

Doctoral Thesis

Experimental Study on Interaction Mechanics between
an Active Lugged Wheel and Sandy Soil

March, 2015

Doctoral Program in Integrated Science and Engineering
Graduate School of Science and Engineering
Ritsumeikan University

YANG YANG

Doctoral Thesis reviewed
by Ritsumeikan University

Experimental Study on Interaction Mechanics between
an Active Lugged Wheel and Sandy Soil

(能動ラグ型車輪と砂質土間の相互作用力学
に関する実験的研究)

March, 2015

2015年3月

Doctoral Program in Integrated Science and Engineering

Graduate School of Science and Engineering

Ritsumeikan University

立命館大学大学院理工学研究科

総合理工学専攻博士課程後期課程

YANG YANG

ヤン ヤン

Supervisor: Professor SHUGEN MA

研究指導教員：馬 書根 教授

Abstract

Experimental Study on Interaction Mechanics between
an Active Lugged Wheel and Sandy Soil

by

Yang YANG

Doctor of Philosophy in Department of Robotics

Ritsumeikan University, Biwako-Kusatsu Campus

Professor Shugen MA, Chair

In planetary explorations and geological investigations, wheeled robots have been deployed on the sandy environments that typify terrestrial, lunar, and Martian surfaces. On such soft terrains, wheels easily slip and become trapped, leading to possible mission failure. The mobility of wheeled robots can be improved by attaching protrusions or convex patterns called lugs (i.e., grousers) to the wheel surfaces. However, the individual lugs interact with the soil, generating unwanted fluctuations of the vertical force and drawbar pull of the lightweight vehicles. Such oscillations compromise the stability of the robot.

To alleviate this problem, we have developed a novel wheeled mechanism called Active Lugged Wheel (ALW), which integrates a set of actively actuated lugs into a traditional wheel. As the wheel rolls over soft terrain, the inclination angle and protruded length of the lugs can be actively controlled by changing the position of the lug shaft. Such versatile motion modes stabilize the vertical forces and drawbar pull and may potentially increase the soil reaction force. However, to achieve these goals, we must first fully characterize the ALW-soil interaction.

The ALW-soil interaction is influenced by the various design and motion parameters of the wheel and lugs. To date, no accurate models exist for understanding such complex interactions. To highlight how tuning the lug trajectory improves the performance of the ALW mechanism, we first investigate the lug-soil interaction characteristics of a single lug

without the wheel. In this experiment, the soil reaction forces were independent of traveling speeds below 10 mm/s. As the lug horizontally moves through the soil, it generates both transient and steady-state lug-soil interaction forces. In the transient stage, the soil reaction force is mainly altered by ground swell caused by the lug excavation. In both transient and steady states, the soil reaction force is a quadratic function of lug sinkage length.

Next, the drawbar pull and vertical force of the ALW mechanism with a single lug is measured during the complete ALW-soil interaction process. Similar to the single-lug experiments, the ALW-soil interaction measurements reveal a quadratic relationship between the maximum soil reaction force and lug sinkage length.

Both experiments confirm that the ALW-soil interaction forces significantly depend on lug inclination angle and sinkage length. Moreover, by virtue of its rim, the lugged wheel improves the drawbar pull and vertical force relative to a single lug. Moreover, the active lug can be inserted into the soil earlier and withdrawn later than the conventional fixed lug. The extended time in the soil increases the soil reaction forces over a wider range. From experience, we identified six lug trajectories by which the ALW mechanism can dampen the fluctuations of the drawbar pull arising from a fixed lugged wheel.

The experimental results and analyses verify the performance of the developed ALW mechanism. In particular, tuning the lug trajectory improves the soil reaction forces. Therefore, the ALW mechanism is a suitable locomotive module for deployment in high-risk tasks on sandy terrains.

Contents

Contents	1
List of Figures	4
List of Tables	8
Acknowledgements	9
1 Research Background	1
1.1 Locomotion Mechanism on Sandy Terrains	2
1.1.1 Wheeled Vehicles	2
1.1.2 Others	4
1.2 Effects of the Lug	6
1.2.1 Fixed Lugs	8
1.2.2 Movable Lugs	11
1.2.3 Lug-soil Interactions	12
1.2.4 Lugged Wheel-soil Interactions	13
1.3 Terramechanics	14
1.3.1 Methods	14
1.3.2 Experimental Testbeds	15
1.3.3 Terramechanics-based Mobility Control	17
1.4 Motivation and Outline of this Thesis	18
2 Principle and Prototype of the Active Lugged Wheel	21
2.1 Concept of the Active Lugged Wheel	22
2.2 Kinematics of the ALW Mechanism	23

2.2.1	Inclination Angle and Sinkage Length	23
2.2.2	Inverse Kinematic Model	26
2.2.3	Workspace Analysis	26
2.3	Locomotion on Soft Terrains	27
2.3.1	Versatile Locomotion Modes	27
2.3.2	Lug-soil Interaction Process in Active Lugged Wheeled Mode	29
2.4	ALW-soil Interaction Force	30
2.4.1	Wheel-soil Interaction Force	30
2.4.2	Lug-soil Interaction Force	32
2.4.3	ALW-soil Interaction Force	33
2.5	Prototype Design of the ALW Mechanism	33
2.5.1	Mechanism Design of the ALW Module	33
2.5.2	Controller Design of the ALW Module	37
2.6	ALW-based Mobile Robot	38
2.6.1	Concept	38
2.6.2	Control Problem Statement	40
2.7	Summary	42
3	Lug-soil Interaction Characteristics	43
3.1	Motion Parameters and Lug Forces	44
3.2	Experimental Setup	46
3.2.1	Experimental Overview and Conditions	46
3.2.2	Lug-soil Interaction Testbed and Soil Conditions	47
3.2.3	Experimental Procedure	49
3.2.4	Data Processing	50
3.3	Experimental Results	51
3.4	Discussions	55
3.4.1	Effect of Horizontal Displacement	55
3.4.2	Effect of Lug Sinkage Length	59
3.4.3	Effect of Lug Inclination Angle	63
3.5	Summary	66
4	ALW-soil Interaction Characteristics	67
4.1	ALW-soil Interaction Process	68

4.2	Experimental Setup	72
4.2.1	Experimental Overview and Conditions	72
4.2.2	ALW-soil Interaction Testbed	73
4.2.3	Experimental Procedure	73
4.2.4	Data Processing	76
4.3	Experimental Results	76
4.3.1	Sinkage Length Dependency	80
4.3.2	Inclination Angle Dependency	80
4.4	Discussion	81
4.4.1	Effect of Lug Sinkage Length	81
4.4.2	Effect of Lug Inclination Angle	84
4.5	Summary	84
5	Performance Improvement by the ALW Mechanism	87
5.1	Experimental Overview	88
5.1.1	Wheel Configurations	88
5.1.2	Motion Sequence of the Fixed Lugged Wheel	89
5.1.3	Fluctuation Reduction in Drawbar Pull	91
5.2	Experimental Results and Discussion	94
5.2.1	Confirmation of Wheel-lug Interference	94
5.2.2	Soil Reaction Forces of Two Lugged Wheels	97
5.2.3	Effectiveness of the Fluctuation Reduction Method	99
5.3	Summary	104
6	Conclusion and Future Work	105
6.1	Conclusion	105
6.2	Future Work	107
	Bibliography	108
	Published Papers During Doctoral Course	115

List of Figures

1.1	Examples of mobile robots: (a) <i>Sojourner</i> rover, (b) <i>Rocky 7</i> rover, (c) <i>Opportunity</i> rover, (d) <i>Curiosity</i> rover, (e) <i>Nomad</i> , deployed in the Atacama Desert, (f) <i>Scarab</i> lunar rover, (g) <i>Tri-Star IV</i> lunar rover.	3
1.2	Examples of tracking robots: (a) <i>Light Crawler</i> , (b) <i>RHex</i> , (c) <i>WhegsTM IV</i> , (d) <i>Lemur IIb</i> in sandy environments.	5
1.3	Examples of hybrid locomotion mechanisms deployed in sandy environments: (a) <i>Track Walker</i> , (b) <i>ATHLETE</i> , (c) <i>LEON</i> , (d) <i>crank-wheel</i>	7
1.4	Examples of lugged wheels: (a) <i>Lunakhod I</i> rover, (b) <i>Apollo</i> rover, (c) <i>Sojourner</i> rover, (d) <i>Spirit</i> rover, (e) <i>Curiosity</i> rover, (f) <i>Micro 5</i> rover.	9
1.5	Experimental study for investigating the effects of (a) lug height on driving wheel, (b) lug inclination angle on driving wheel, (c) lug number on wheeled robot (d) lug number on tracked robot.	10
1.6	(a) Movable lug cage wheel, (b) lug motion pattern of movable lug cage wheel (λ is the lug angle; α and θ denote the lug inclination and rotation angles, respectively), (c) compound walking wheel.	11
1.7	Single-wheel testbeds developed by (a) MIT, (b) Tohoku University, (c) HIT, (d) JAXA, (e) DLR, (f) CMU.	16
1.8	Physics-based approach [1].	17
2.1	Schematic of the ALW: (a) mechanism, (b) kinematic diagram of ALW with eight active lugs.	22
2.2	Wheel coordinate system.	23
2.3	Relationship between the protruded length l_{pi} and sinkage length l_{si} when the lug has sunk into the soil (a) partly and (b) completely.	25
2.4	The ALW mechanism operates in three modes on soft terrains: (a) smooth wheeled mode, (b) fixed lugged wheeled mode, (c) active lugged wheeled mode (the working lug is highlighted in red).	28
2.5	Stress model of (a) the wheel rim, (b) the lug, (c) the ALW module on soft terrain.	31

2.6	The ALW prototype: (a) front view, (b) rear view, (c) section view.	34
2.7	Transmission system of (a) wheel rim, (b) carrier, (c) sun gear.	35
2.8	Planetary gear mechanism.	36
2.9	Lugs and lug shaft: (a) one set, (b) eight-lug configuration.	37
2.10	Wheel-like shell: (a) 3D view, (b) section view.	38
2.11	The schematic blocks of the proposed dsPIC-based motion controller.	39
2.12	Prototype of four-ALW-robot.	40
2.13	(a) Kinematic model and (b) dynamic model of the four-wheel-robot.	41
3.1	Motion parameters and force model for a single lug with translational motion.	44
3.2	Experimental procedure of (a) bulldozing experiment I, (b) bulldozing experiment II.	47
3.3	(a) Lug-soil interaction testbed and (b) data acquisition system.	48
3.4	Removal of noise from measured forces: (a) original signal measured in one experiment trail, (b) filtered signal, and (c) filtered signals from ten experiment trail and their mean value.	50
3.5	(a) Horizontal forces and (b) vertical forces in bulldozing experiments I at inclination angle $\alpha = 90^\circ$ and sinkage length $l_s = 30$ mm for selected horizontal speeds.	51
3.6	Horizontal forces (left panels) and vertical forces (right panels) in bulldozing experiment I ($v = 10$ mm/s) at inclination angles α of (a) 90° , (b) 105° , (c) 120° , and (d) 135°	52
3.7	Horizontal forces (left panels) and vertical forces (right panels) in bulldozing experiment I ($v = 10$ mm/s) at sinkage lengths l_s of (a) 10 mm, (b) 20 mm, (c) 30 mm, and (d) 40 mm.	53
3.8	Comparison of horizontal forces (left panels) and vertical forces (right panels) measured before and after soil removal in bulldozing experiment II ($l_s = 30$ mm, $v = 10$ mm/s) at inclination angles α of (a) 90° and (b) 120°	54
3.9	The phenomenon of ground swell in bulldozing experiment I ($\alpha = 90^\circ$, $l_s = 30$ mm, $v = 10$ mm/s).	55
3.10	(a) λ_p in (3.4) and (b) λ_v in (3.5) from bulldozing experiment II at $\alpha = 90^\circ$, $l_s = 30$ mm, $v = 10$ mm/s, and at $\alpha = 120^\circ$, $l_s = 30$ mm, $v = 10$ mm/s.	56
3.11	Comparison of experimental results and fitted results of horizontal forces (left panels) and vertical forces (right panels) in bulldozing experiment I ($v = 10$ mm/s) at inclination angles α of (a) 90° , (b) 105° , (c) 120° , and (d) 135°	58
3.12	F_{p0} in (3.8) (left panels) and F_{v0} in (3.10) (right panels) for bulldozing experiment I at inclination angles α of (a) 90° , (b) 105° , (c) 120° , and (d) 135°	60

3.13	A_p in (3.9) (left panels) and A_v in (3.11) (right panels) for bulldozing experiment I at inclination angles α of (a) 90° , (b) 105° , (c) 120° , and (d) 135°	61
3.14	F_{p0} in (3.12) (left panels) and F_{v0} in (3.13) (right panels) for bulldozing experiment I at sinkage lengths l_s of (a) 10 mm, (b) 20 mm, (c) 30 mm, and (d) 40 mm.	62
3.15	Soil failure in bulldozing experiment at α of (a) 90° and (b) 120°	64
3.16	Ratio of horizontal force to vertical force at selected inclination angles α and sinkage lengths l_s of (a) 10 mm, (b) 20 mm, (c) 30 mm, (d) 40 mm.	65
4.1	Lug trajectory within a complete lug-soil interaction process as the wheel rotates from 0° to 180°	68
4.2	Locomotion of the ALW at initial rotational angle $\theta_1 = 20^\circ$, inclination angle $\alpha = 60^\circ$ (in phase II), sinkage length $l_s = 18$ mm (in phase II) and wheel sinkage $h = 5$ mm. (a) Joint angles calculated from (2.8), (b) lug inclination angle, (c) lug sinkage length, (d) velocity of the lug tip.	69
4.3	Illustration of a single increment of lug displacement.	70
4.4	Actual lug trajectory of the ALW at (a) $\theta_1 = 20^\circ$, $\alpha = 50^\circ$, $l_s = 18$ mm, (b) $\theta_1 = 20^\circ$, $\alpha = 60^\circ$, $l_s = 18$ mm, (c) $\theta_1 = 20^\circ$, $\alpha = 60^\circ$, $l_s = 22$ mm.	74
4.5	(a) ALW-soil interaction testbed, (b) data acquisition system.	75
4.6	Removal of noise from measured forces: (a) original signal measured during one experimental trial, (b) filtered signal, and (c) filtered signals from ten experimental trials and their mean (red dashed line).	77
4.7	Drawbar pulls (left panels) and vertical forces (right panels) at selected sinkage lengths l_s and inclination angles α of (a) 50° , (b) 60° , and (c) 70°	78
4.8	Drawbar pulls (left panels) and vertical forces (right panels) at selected inclination angles α and sinkage lengths l_s of (a) 10 mm, (b) 14 mm, (c) 18 mm, and (d) 22 mm.	79
4.9	ALW-soil interaction process: (a)→(b)→(c).	80
4.10	Drawbar pulls fitted by (4.6) (left panels) and vertical forces fitted by (4.7) (right panels). The inclination angles α are (a) 50° , (b) 60° , and (c) 70°	83
4.11	Ratio of drawbar pull to vertical force at selected inclination angles α and sinkage lengths l_s of (a) 10 mm, (b) 14 mm, (c) 18 mm, and (d) 22 mm.	85
5.1	Experimental wheel types: (a) Smooth Wheel (SW), (b) Cage Lugged Wheel (CLW), (c) Active Lugged Wheel (ALW).	88
5.2	Motion behavior of the prototype to simulate a wheel with a fixed lug of 13 mm height.	89
5.3	Locomotion of a wheel fitted with a fixed lug of 13 mm height at wheel sinkage $h = 5$ mm. (a) Joint angles calculated from (2.8), (b) lug inclination angle, (c) lug sinkage length.	90

5.4	Lug trajectory within a complete lug-soil interaction process as the wheel rotates from 0° to 180° for reducing the fluctuation of drawbar pull.	92
5.5	Locomotion of the ALW at initial rotational angle $\theta_1 = 20^\circ$, inclination angle $\alpha = 60^\circ$ (in phase II), $\theta_a = 40^\circ$, $l_{sa} = 18$ mm, $\theta_b = 55^\circ$, $l_{sb} = 2$ mm, $\theta_c = 75^\circ$, $l_{sc} = 12$ mm, and wheel sinkage $h = 5$ mm. (a) Joint angles calculated from (2.8), (b) lug inclination angle, (c) lug sinkage length.	93
5.6	Actual lug trajectory of the ALW at trajectory “Inc60-II”.	94
5.7	Comparison of drawbar pulls (left panels) and vertical forces (right panels) generated by the Smooth Wheel (SW), the Lugged Cage Wheel (LCW), the ALW, and the sum of SW and LCW (SW + LCW), at initial rotational angles θ_1 , inclination angles α and sinkage lengths l_s of (a) $\theta_1 = 20^\circ$, $\alpha = 50^\circ$, $l_s = 14$ mm, (b) $\theta_1 = 20^\circ$, $\alpha = 60^\circ$, $l_s = 18$ mm, (c) $\theta_1 = 30^\circ$, $\alpha = 70^\circ$, $l_s = 18$ mm.	95
5.8	The phenomenon of ground swell photographed as the wheel rolls from (a) \rightarrow (b) \rightarrow (c).	96
5.9	Comparison of drawbar pulls (left panels) and vertical forces (right panels) generated by a fixed lugged wheel (lug height = 13 mm) and by the ALW mechanism at selected sinkage lengths l_s and inclination angles α of (a) 50° , (b) 60° , and (c) 70°	98
5.10	Drawbar pulls (left panels) and vertical forces (right panels) for different trajectories. (a) “Inc50-I” and “Inc50-II”, (b) “Inc60-I” and “Inc60-II”, (c) “Inc70-I” and “Inc70-II”.	100
5.11	Definition of parameters for evaluating fluctuations of wheel-soil interaction force.	101
5.12	$\Delta\theta$ calculated from (5.1) for (a) drawbar pulls and (b) vertical forces of the ALW adopting six trajectories (blue bars) and fixed lugged wheel (red bar).	102

List of Tables

2.1	Specifications of the ALW module whose kinematical diagram is shown in Fig. 2.1 (b).	36
3.1	Values used for motion parameters in the experiments.	46
3.2	Soil parameters.	49
3.3	Values for parameters in (3.6) and (3.7) determined from bulldozing experiment I.	57
3.4	Values for coefficients in (3.8) and (3.9) determined from bulldozing experiment I.	63
3.5	Values for coefficients in (3.10) and (3.11) determined from bulldozing experiment I.	63
3.6	Values for coefficients in (3.12) determined from bulldozing experiment I.	64
3.7	Values for coefficients in (3.13) determined from bulldozing experiment I.	64
4.1	Values of lug motion parameters (in phase II) adopted in the experiments.	72
4.2	Experimental peak values of drawbar pull F_p and vertical force F_v at different inclination angles α and sinkage lengths l_s .	81
4.3	Coefficients of (4.6) determined by fitting to experimental data.	82
4.4	Coefficients of (4.7) determined by fitting to experimental data.	82
5.1	Values of lug motion parameters (in phase II) adopted in the Cage Lugged Wheel (CLW) experiments.	89
5.2	Values of motion parameters adopted in the experiments.	92
5.3	Evaluation of fluctuations in wheel-soil interaction forces.	103

Acknowledgements

First of all, I would express my gratitude to my supervisor, Prof. Shugen Ma, of the Department of Robotics at Ritsumeikan University, for his patient guidance, enthusiastic encouragement, and useful critiques on this research work. Especially, he helped me to overcome many bad habits. Although I will complete the doctoral course soon, a heart with deep thanksgiving will exist in my life forever.

I would like to thank Prof. Sadao Kawamura not only for his valuable suggestions on my research activities, but also for his instruction in field construction, where the performance of the developed robot can be tested in real environments.

I would also like to thank Prof. Satoshi Ueno, for his support in my job hunting activity. In addition, it is my pleasure to thank Prof. Hirokazu Maeda, Prof. Makoto Nokata, and Prof. Ryuta Ozawa for their valuable suggestions and comments on my research in seminars.

I am grateful to all my colleagues in Ma laboratory, to Dr. Yi Sun, Mr. Chuanguo Li, Mr. Dingxin Ge, Mrs. Yongchen Tang, Mr. Chao Ren, Ms. Norzalilah Binti Mohamad Nor, Mr. Wenbin Tan, Mr. Yang Tian, Mr. Fabian Reyes who gave me great help and many useful comments for my research, to Mr. Atsushi Kakogawa, Mr. Takahiro Matsuno who helped me greatly in the lab, to Mr. Ryohei Yamamoto, Mr. Longhe Zheng, Mr. Siyu Huang for their assistance and supporting on mechanism design, prototype fabrication and experiments, and especially, to two OB students, Dr. Qiquan Quan and Dr. Xiaodong Wu for their advice during my research life. Studying with them together in Ritsumeikan University leads me a colorful and fruitful campus life.

It is my pleasure to thank Dr. Liang Ding, Dr. Zhongkui Wang, and Dr. Ming Hu for their kind help in my research activities and daily life.

The workshop of Ritsumeikan University, who contributed the prototype fabrication, is also gratefully acknowledged.

Special thanks are also extended to Prof. Shigeo Hirose, Visiting Professor at Ritsumeikan University and CTO of HiBot Corp., for his constructive advice in mechanical

design. In addition, he provided me an opportunity of internship at HiBot Corp. where we appreciated joy in robot development.

My study was supported by “strategic research foundation grant-aided project for private universities (2013 - 2017)” from Ministry of Education, Culture, Sports, Science and Technology, Japan. The foundation is gratefully acknowledged.

Finally, I would like to thank my beloved family and friends for their encouragement and understanding during my study.

Curriculum Vitæ

Yang YANG

Education

1993-1999	Elementary School of Chunhai (Dalian, Liaoning, China) Elementary School Student
1999-2002	Dalian No.16 Middle School (Dalian, Liaoning, China) Secondary School Student
2002-2005	Dalian No.1 High School (Dalian, Liaoning, China) Upper Secondary School Student
2005-2009	Hefei University of Technology (Hefei, Anhui, China) Bachelor Degree of Mechanical Design Manufacturing and Automation
2009-2011	Harbin Institute of Technology (Harbin, Heilongjiang, China) Master Degree of Mechatronics Engineering
2011-2015	Ritsumeikan University, BKC (Kusatsu, Shiga, Japan) Doctoral Candidate, Robotics

Personal

Born	March 18, 1986, Liaoning, China.
Research Interests	Terramechanics, Mobile Robot, Biomimetic Systems, Motion Control.

Chapter 1

Research Background

Sandy terrains are widely distributed across terrestrial, lunar and Martian surfaces. Such surfaces covered with fine-grained loose soil regolith are difficult to traverse, and their access presents an ongoing challenge for mobile robots.

Many robots have been developed for planetary explorations and geological investigations in sandy environments that are hazardous to humans (e.g. active volcanoes) or that are difficult for humans to access (e.g. Martian surfaces). On such difficult terrains with poor trafficability, robots easily slip and become trapped, leading to possible mission failure. An example is NASA's Mars exploration rover *Opportunity* which became trapped in a region named Purgatory Dune in April 2005. Scientists spent approximately five weeks trying to release it [2]. After six years of unprecedented exploration of the Red Planet, *Opportunity*'s sister rover *Spirit* became immobilized in January 2010. *Spirit* was designated a stationary science platform after several months of unsuccessful efforts to set it free from a sand trap [3].

To improve the mobility of robots on soft terrains, researchers and engineers have invested much effort into developing new forms of locomotion devices and understanding the mechanics of device-soil interactions.

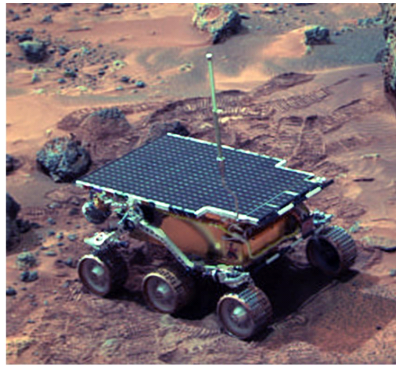
1.1 Locomotion Mechanism on Sandy Terrains

New locomotion mechanisms for undertaking complex scientific exploration tasks on sandy terrains have been extensively investigated. Examples of loose terrain trekkers include wheeled vehicles, track-based crawlers, and robots based on hybrid mechanisms.

1.1.1 Wheeled Vehicles

Among the above-mentioned locomotive devices, the wheeled robot is favored in practice for its simplicity, reliability, and efficiency.

Among the wheeled robots proposed for accessing sandy terrains in the past few decades, the most dramatic are those developed for planetary exploration by the NASA Jet Propulsion Laboratory [4]. The *Sojourner* rover was the first autonomous Mars exploration vehicle (Fig. 1.1 (a)), followed by *Rocky 7* [5] (Fig. 1.1 (b)). The twin rovers *Spirit* and *Opportunity* (Fig. 1.1 (c)) have been deployed for more than ten years and have completed many scientific exploration tasks. For example, *Opportunity* has accomplished the mission's primary scientific goal: to search for and characterize a wide range of rocks and soils that hint at past water activity on Mars. In addition, *Opportunity* has completed astronomical observations and acquired atmospheric data [6]. The newest Mars rover *Curiosity* (Fig. 1.1 (d)) landed on Aeolis Palus in Gale Crater on August 6, 2012 [7]. This rover was deployed to investigate the Martian climate and geology, to assess whether the selected field site inside Gale Crater has ever offered environmental conditions favorable for microbial life (and to investigate the role of water in this conditioning), and to evaluate whether Mars could be rendered inhabitable for future human exploration [8]. On June 24, 2014, after one Martian year (687 earth days) of searching, *Curiosity* reported that Mars once had environmental conditions favorable for microbial life [9]. These successful applications have spurred great interest in wheeled mobile robots for planetary exploration missions. The mobile robot *Nomad*, developed by Carnegie Mellon University for extended terrestrial and planetary exploration (Fig. 1.1 (e)), traversed 223.5 kilometers of the rugged Atacama



(a)



(b)



(c)



(d)



(e)



(f)



(g)

Figure 1.1. Examples of mobile robots: (a) *Sojourner* rover, (b) *Rocky 7* rover, (c) *Opportunity* rover, (d) *Curiosity* rover, (e) *Nomad*, deployed in the Atacama Desert, (f) *Scarab* lunar rover, (g) *Tri-Star IV* lunar rover.

Desert in Northern Chile in 1997. This mission was autonomously controlled by operators thousands of kilometers away [10] [11].

NASA’s rovers are outfitted with suspension systems, allowing the wheels to ride over obstacles. Other groups have developed novel mechanisms that improve the environmental adaptability of wheeled robots. An example is *Scarab*, a prototype rover designed for surveying resources in the polar craters of the moon (Fig. 1.1 (f)). *Scarab*’s chassis can adjust the wheelbase and height, thereby stabilizing the drill in contact with the ground. *Scarab* also adjusts its posture when ascending and descending steep slopes [12]. The Japanese government has developed a policy for future space development, inspiring Aoki et al.’s transformable three-wheeled lunar rover named *Tri-Star IV* [13]. This rover comprises three spring wheels and two rotating arms (Fig. 1.1 (g)). It can expand from a storage posture, extricate itself from traps, and adapt to slopes or rough terrains using its arms.

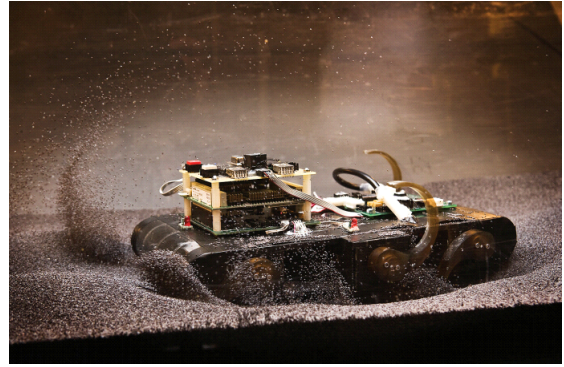
1.1.2 Others

Tracked robots are advantaged by higher stability and terrain adaptability than wheeled robots. These rovers can climb over obstacles that are unachievable by same-sized wheeled robots and are generally less prone to slipping on soft terrains than wheeled robots. The lunar vehicle *Light Crawler* is outfitted with four mesh-crawlers [14] (Fig. 1.2 (a)). The crawler links reduce the contact pressure and improve the robot’s mobility, particularly its climbing ability on pure sand slopes.

Although legged robots are less efficient and slower than wheeled robots, they can flexibly traverse rocky terrains. Inspired by animal walking, Buehler et al. developed *RHex* (Fig. 1.2 (b)), which achieves extreme mobility by a single actuator for each leg. In particular, *RHex* maintains high speed over sandy terrains [15] [16]. The biologically-inspired platform *WhegsTM IV* (Fig. 1.2 (c)) was developed for operations in a surf-zone environment [17] [18]. *Lemur IIb* (Fig. 1.2 (d)) is a four-limbed robotic system used for investigating climbing system designs, including mechanical systems (novel end-effectors, kinematics, joint design), sensing (force, attitude, vision), low-level control (force-control



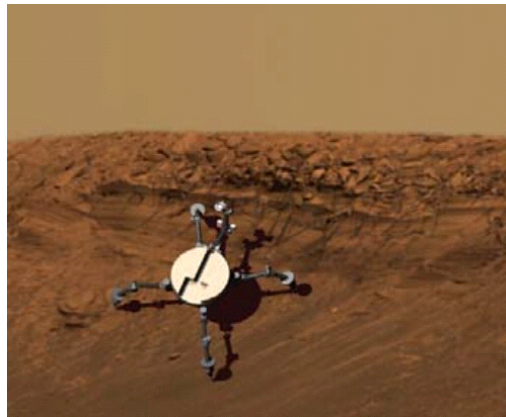
(a)



(b)



(c)



(d)

Figure 1.2. Examples of tracking robots: (a) *Light Crawler*, (b) *RHex*, (c) *WhegsTM IV*, (d) *Lemur IIb* in sandy environments.

for tactile sensing and stability management), and planning (joint trajectories for stability) [19]. In general, legged robots are unsuitable for exploration because they consume much energy.

The aforementioned discussion implies that robots based on single locomotive mechanisms are difficult to adapt to complex soft environments. Thus, researchers and engineers have proposed hybrid locomotive mechanisms for improved terrain adaptability and mobility. Nagatani et al. developed a leg-track hybrid locomotion mechanism *Track Walker* that traverses loose-soil slopes (Fig. 1.3 (a)). *Track Walker* comprises three track modules and six actuators: three motors for standard tracked locomotion, two for subtrack motions that change the mounting angles, and one for simple legged motion [20]. *ATHLETE* is a large mobile six-legged lunar vehicle developed for lunar exploration by the Jet Propulsion Laboratory (Fig. 1.3 (b)). *ATHLETE*'s wheels are generally used for rolling but can be employed as feet when walking is required [21]. Rohmer et al. proposed a novel transforming hybrid walking/roving mechanism called Lunar Exploration Omnidirectional Netbot (*LEON*) (Fig. 1.3 (c)). This hexapod can fold two of its limbs and transform them into wheels, thereby transforming from a six-legged robot into a large wheeled robot [22]. Nakano et al. developed a novel mobile base named *crank-wheel* (Fig. 1.3 (d)), comprising wheels and a connecting coupler link called a crank leg. In sand dune field experiments, the crank legs always extricated the wheels from the sand, preventing sinking. Forward walking motion is generated by the paddle actions of the grouzers attached at the bottom of the crank-legs [23].

1.2 Effects of the Lug

The mobility of terrestrial robots can be simply and effectively improved by adding protrusions or convex patterns called lugs (i.e., grouzers) to the wheels/tracks. These protrusions reduce slippage of the robot. Lugs can be classified as fixed or movable; the latter can be adjusted in real time. The performance of lugged devices has been evaluated in



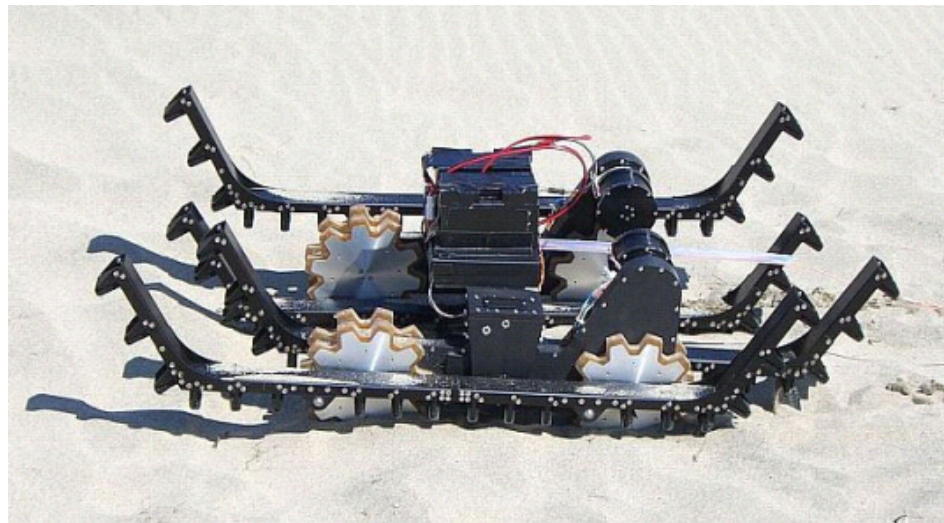
(a)



(b)



(c)



(d)

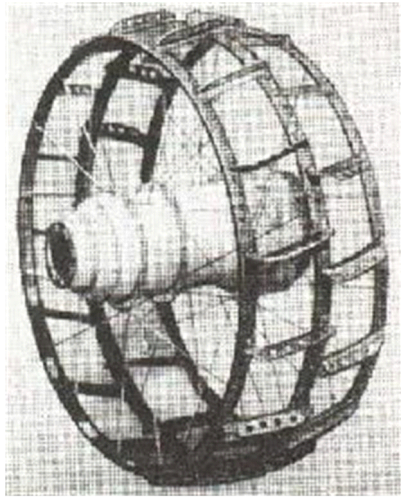
Figure 1.3. Examples of hybrid locomotion mechanisms deployed in sandy environments: (a) *Track Walker*, (b) *ATHLETE*, (c) *LEON*, (d) *crank-wheel*.

numerous experimental studies and theoretical analyses, and fundamental guidelines for determining the height, number, and other lug parameters have been established.

1.2.1 Fixed Lugs

Lugs are routinely fixed to the wheel/track surfaces of mobile robots to enhance their capability on loose sandy terrain. The wheels of the *Lunakhod I* vehicle (Fig. 1.4 (a)) comprise three rims; each connected to the hub by sixteen spokes. They are formed into a wire mesh with sixteen 20-mm-high lugs to improve traction [24]. The wheels of the *Apollo* rover are covered with zinc-plated piano wire woven into an elastic mesh (Fig. 1.4 (b)). Titanium lugs (of height 10 mm) are arranged in a chevron pattern around the circumference of the tire, providing a traction aid and a coverage of approximately 50% [25]. The 13 cm-diameter wheels of *Sojourner* (Fig. 1.4 (c)) are made of aluminum and outfitted with stainless steel treads and cleats that provide traction [26]. Each wheel of *Spirit* is embellished with cleats and is independently actuated (Fig. 1.4 (d)), enabling the rover to climb loose soil-like materials and traverse rocks whose heights approximate the wheel diameter [27]. The six wheels of *Curiosity* (Fig. 1.4 (e)) have chevron-shaped grousers with a 15° spacing. The grousers radially protrude 7.5 mm from the 0.75-mm-thick wheel skin [28]. In *Micro 5* (Fig. 1.4 (f)), turning is facilitated by special tires with spiral fins [29].

These successful applications confirm that lugs significantly influence the traveling performance of lightweight vehicles. Hence, many experimental investigations have been performed to further evaluate the effects of lugs. Liu et al. conducted experiments on a single-wheel testbed, and recommended certain lug parameters such as spacing angle, height, and thickness [30]. Ding et al. reported the effects of lug height and inclination angle (Fig. 1.5 (a), (b)) on the performance of driving wheels [31]. They found that, while increasing the lug height increases the drawbar pull amplitude of the wheel, it also magnifies unwanted fluctuations. These fluctuations can be reduced by increasing the lug inclination angle, similar to the engagement of helical gears, but may generate lateral force, thereby introduc-



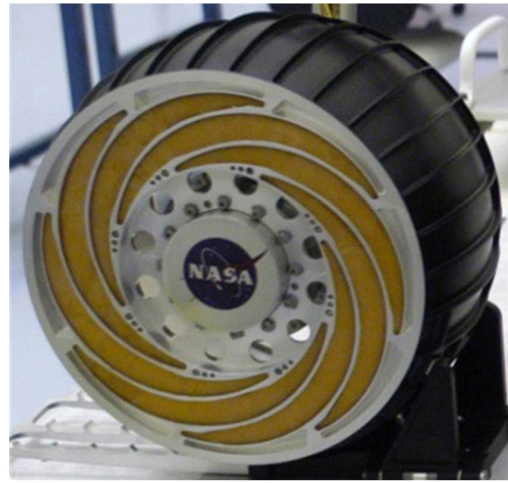
(a)



(b)



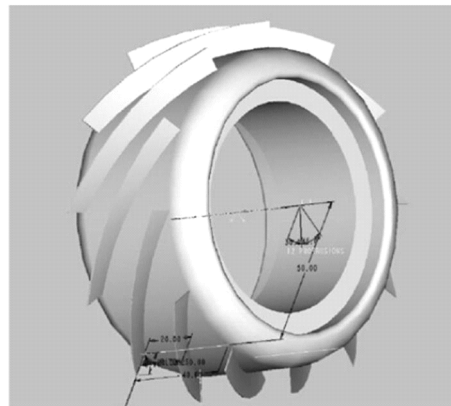
(c)



(d)



(e)



(f)

Figure 1.4. Examples of lugged wheels: (a) *Lunakhod I* rover, (b) *Apollo* rover, (c) *Sojourner* rover, (d) *Spirit* rover, (e) *Curiosity* rover, (f) *Micro 5* rover.

ing mechanical performance differences between the forward and backward motions of the wheel. South et al. experimentally confirmed the effects of lug interval ((Fig. 1.5 (c)) on the linear speed of the vehicle [32], and on the slip ratio [33]. They concluded that increasing the number of lugs improves the traveling performance up to some limit. In addition to wheeled robots, they also investigated the effects of lugs on the traveling performance of tracked rovers [33] [34], as shown in Fig. 1.5 (d). Moreover, Ding et al. reported the effect of lug height and lug number on wheel steering performance [35]. The studies with regard to fixed lugs mainly focused on the effects of lug shape on the traveling performance of the robots.

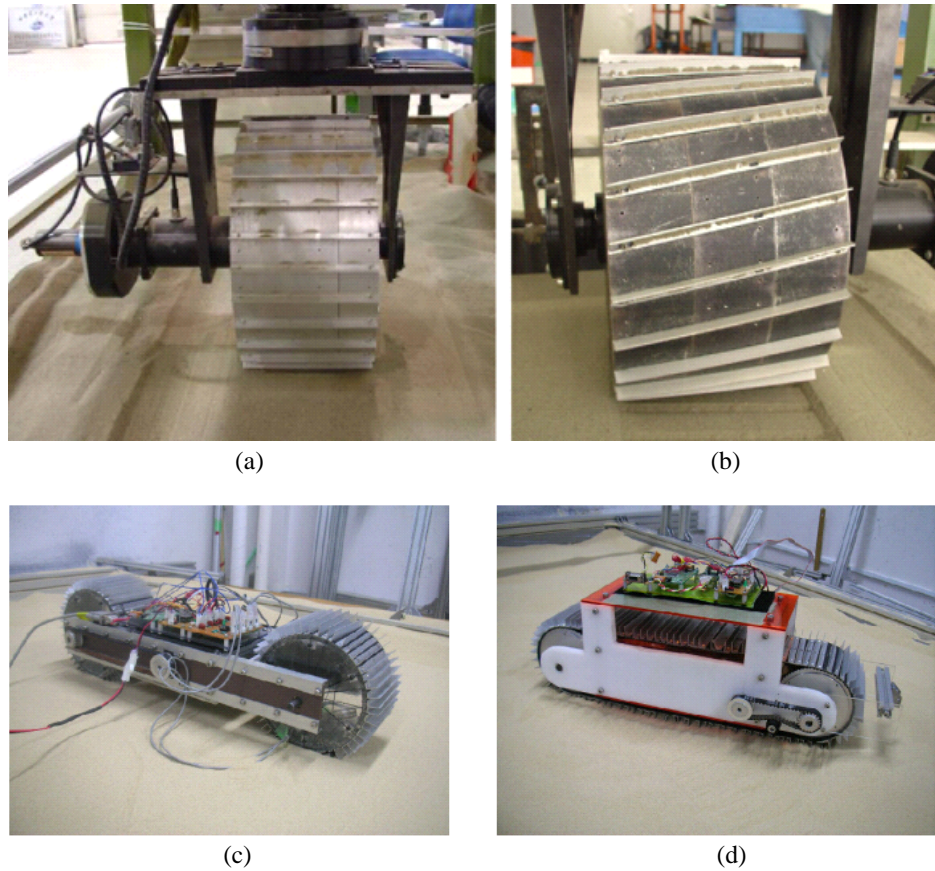


Figure 1.5. Experimental study for investigating the effects of (a) lug height on driving wheel, (b) lug inclination angle on driving wheel, (c) lug number on wheeled robot (d) lug number on tracked robot.

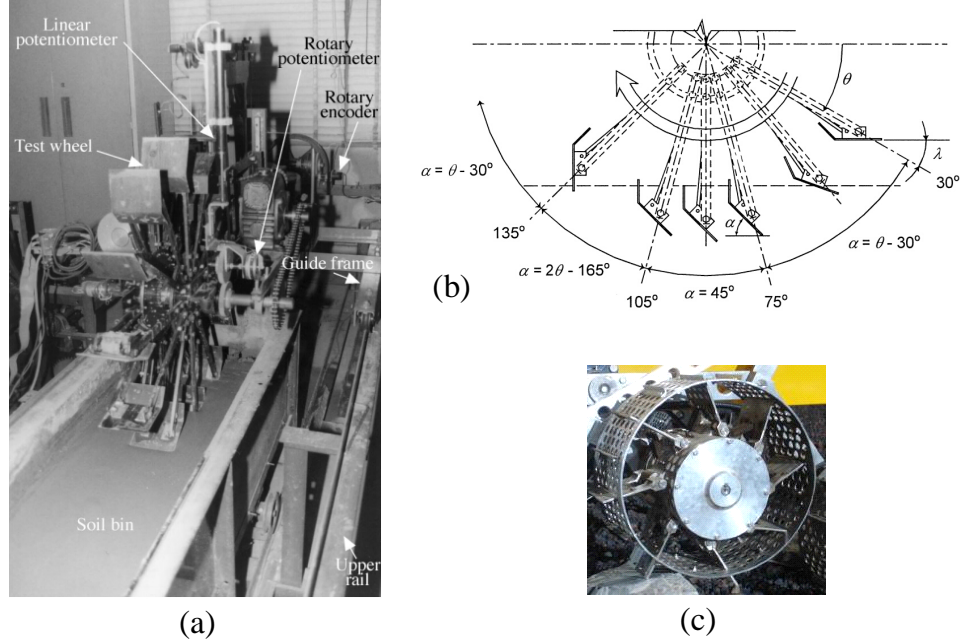


Figure 1.6. (a) Movable lug cage wheel, (b) lug motion pattern of movable lug cage wheel (λ is the lug angle; α and θ denote the lug inclination and rotation angles, respectively), (c) compound walking wheel.

1.2.2 Movable Lugs

Unlike the shapes of lugs, which are generally determined during the design stage, lug trajectories change as a robot performs its tasks. Therefore, to overcome the limitations of conventional wheels studded with fixed lugs, researchers have developed mechanisms with movable lug mechanisms that adjust the lug trajectories. Chen et al. proposed movable lugs for the driving wheels of boat tractors [36]. This design maximizes the pull and lift forces by setting the lug plates at an appropriate angle (Fig. 1.6 (a), (b)). In comparison experiments, a single movable lug generated greater maximum resultant force than a fixed lug [37] [38]. Moreover, the peak pull force depended on the inclination angle of the flat movable lug, being slightly larger at 45° than at 30° and 60° , whereas the peak lift force is reduced at larger lug inclination angles. Both the pull and lift forces were reported to increase with increasing wheel sinkage. By measuring the lug forces acting on multi-movable lugs, this group confirmed that the movable action of the lug plate generated superior pull and lift forces to those acting on the fixed lug wheel [39]. Fig. 1.6 (c) shows the compound walking

wheel developed by the Intelligent Vehicle Group of Jilin University, China. The retractile laminas on this wheel can be extended and withdrawn [40]. Adopting a terramechanics model, Chen et al. concluded that this walking wheel can improve the mobility of a rover on loose lunar terrain. Because the inclination angle or sinkage length of the lug is tunable, these new wheel designs enhance the traveling performance of the device. However, the lug trajectories achieved by these wheels are limited by the few degrees of freedom of the mechanisms.

1.2.3 Lug-soil Interactions

In evaluating the performance of locomotion modules equipped with lugs, an important prediction is the lug-soil interaction.

The passive pressure theory is a simple, practical method [41] that has been used successfully to predict lug forces in wet soil. Gee-Clough et al. divided the action of lug plate into vertical and horizontal; and then calculated the reaction forces owing to vertical failure and horizontal failure by Bekker's plate-sinkage theory and passive pressure theory, respectively [42]. Considering the soil trench made by the preceding lug, the passive pressure theory was modified by Hermawan et al. The modified model gives a good representation of the reaction forces acting on the multi-movable lug cage wheel [43]. However, the main demerit of passive pressure theory lies in the assumption that the free soil surface must be horizontal, which makes it difficult to deal with situations in which the ground swells continuously.

To predict the cutting resistance of the cutting tools, many models have been proposed in three-dimensional conditions [44] [45] [46] [47]. However, the lug-soil interaction period from its initial contact with the soil to its departure from the soil is far shorter than that of cutting tools, so the force characteristics of the lug within the transient state are of important for the lug-soil interaction prediction.

In addition, based on investigations of soil failure patterns, Harrison et al. modeled lug-soil interaction forces at the start of lug movement by considering three motion parameters:

inclination angle, sinkage length, and moving direction angle of the lug [48] [49]. Finite Element Method (or FEM) has also been used for lug-soil system problems [50] [51].

Based on our experimental observation, we found that some factors having strong effects on lug forces have been ignored in previous studies. For example, some studies have only modeled the normal and tangential forces acting on the front surface of the lug, and ignored the effects of the lug-tip surface that significantly contribute to the lug forces observed in our investigation [52]. Overall, no theory pertaining to lug-soil interaction mechanics is well supported due to the complex soil deformation.

1.2.4 Lugged Wheel-soil Interactions

Bekker [53] and Wong [54] proposed models for predicting wheel-soil interactions. However, the hypothesis of these terramechanics models are frequently inconsistent with existing conditions [55]. Their experimental results (normal stress distributions are directly measured using a pressure sensor array, which is attached to the wheels of a rover) show that the distribution range of normal stress for small wheeled rovers obtained using the proposed method is considerably smaller than that obtained by using conventional method.

In addition to these terramechanics models, researchers have estimated the effect of lugs by discrete element methods (DEM) [56] [57]. Its drawback is the need for powerful computers.

Moreover, because these models assumed smooth-wheeled mechanisms, they cannot inherently capture the fluctuations caused by lugs. With the development of planetary exploration technology, many terramechanics models have been proposed for estimating the effects of lugs on robots traversing sandy terrains. A dynamic terramechanic model of rigid wheels with grousers has been described and validated [58]. This model captures and predicts the dynamic oscillations observed in experimental data obtained from a single-wheel testbed for sinkage, drawbar pull, and normal load. Favaedi et al. modeled the interaction forces between the soil and a flexible wheel equipped with lugs [59]. Based on Terzaghi's solution of the soil bearing capacity, they [60] modeled the effect of grousers

on the traction of Mars exploration rover wheels. Iizuka et al. proposed an equation for calculating the drawbar pull produced by grousers [61].

As the lugged wheel rolls forward on the terrain, forces are exerted on the wheel rim and the lugs. The sum of these forces is the wheel-soil interaction force. Such forces are difficult to model, because the wheel rim and lugs push soil between each other. However, by ignoring the wheel-lug interference effects, previous models lose prediction accuracy. To date, no well-supported theory has been developed for characterizing soil failure generated by wheels equipped with grousers.

1.3 Terramechanics

The word *terramechanics*, a compound of the words *terrain* and *mechanics*, first appeared in Prof. Bekker's book [62]. Terramechanics describes the interaction mechanics between the traveling mechanisms and the soil and between the operating machines and the soil [63]. In this thesis, *terramechanics* means the wheel-soil and/or lug-soil interaction mechanics by which we evaluate the performance of our developed device.

1.3.1 Methods

From terramechanics, which has gradually developed throughout the past several decades, many fundamental principles have emerged for research and development of locomotive vehicles, which can be grouped into five methodologies [63].

- i. Empirical method. A typical empirical method is the cone index (CI) method (or WES method) developed by the U.S. Army Corps of Engineers during the Second World War [64]. Although this method is simple and practical, its application is limited to experimental and similar vehicles.
- ii. Semiempirical method [53]. These methods analyze the experimental results and derive approximation formulas for calculating wheel-soil interactions. Semiempirical

formulas quantify the device-soil interaction mechanics, so are commonly adopted in terramechanics study.

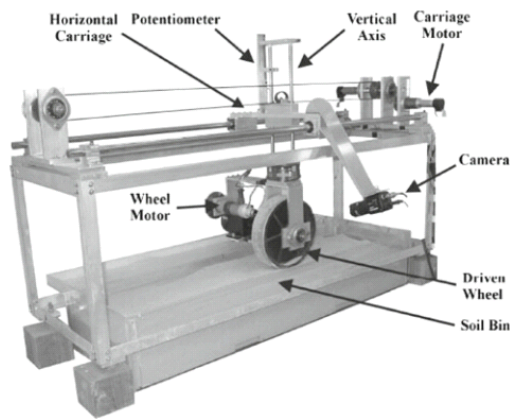
- iii. Model experiments and dimensional analysis method [65]. Like empirical methods, these methods are of limited applicability.
- iv. Theoretical method [66]. These methods attempt to understand soil-device interactions using soil mechanics, elasto-plasticity, constitutive relationships, and other relevant theories. Soil failure under a device is analyzed by Rankine theory, Prandtl theory, and Terzaghi theory.
- v. Numerical simulation method [67]. With the development of computer technology, device-soil interaction mechanics are increasingly simulated by numerical methods. Numerical analysis methods include the finite element method (FEM), DEM, and boundary element method.

Among these research methods, semiempirical and theoretical approaches are most commonly adopted. Since the complicated soil deformations are difficult to accommodate in a theoretical model of lug/wheel-soil interaction forces, we focus on semiempirical analysis in this thesis.

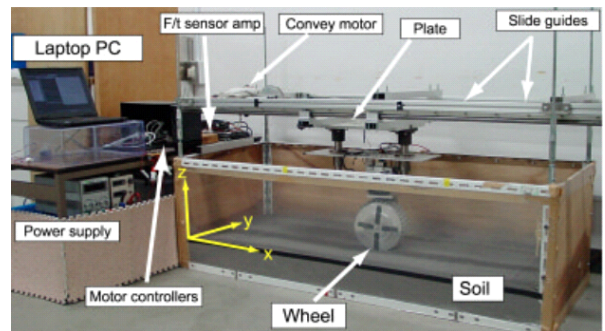
1.3.2 Experimental Testbeds

In the semiempirical method, experimental data are necessary for investigating the device-soil interaction characteristics and improving the newly proposed semiempirical formulas. To this end, researchers and institutions have developed a variety of experimental testbeds with high-performance sensors.

Dubowsky and Iagnemma from the Field and Space Robotics Laboratory (FSRL) of the Massachusetts Institute of Technology (MIT) developed the first single-wheel testbed with a length of 1.06 m, a width of 0.37 m, and a height of 0.44 m (Fig. 1.7 (a)). This testbed measures the forces and moments acting on the wheel, the driving torque, and the



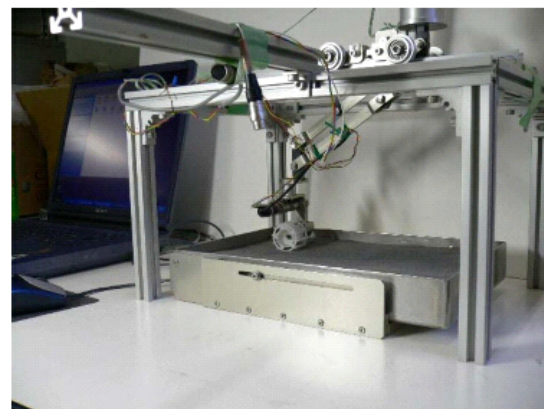
(a)



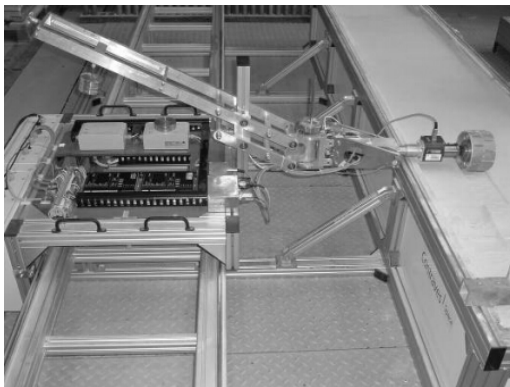
(b)



(c)



(d)



(e)



(f)

Figure 1.7. Single-wheel testbeds developed by (a) MIT, (b) Tohoku University, (c) HIT, (d) JAXA, (e) DLR, (f) CMU.

angular speed of the motor. It also coordinates the angular speed of the wheel and the traveling speed of the carriage to obtain the desired slip ratio [68]. The testbed developed by Tohoku University [69] is similarly configured (Fig. 1.7 (b)). The Harbin Institute of Technology (HIT) developed a single-wheel testbed (Fig. 1.7 (c)) of length 1.70 m, width 0.85 m, and height 0.90 m. This testbed contains a driving motor, a carriage motor, and a steering motor. The motion state and wheel-soil interaction forces are measured by related sensors, including a linear potentiometer displacement sensor, a six-axis F/T sensor, a torque sensor, current sensors, and optical encoders [70]. Researchers from Japan Aerospace Exploration Agency (JAXA) have developed a testbed for evaluating the slope climbing capability of the wheel (Fig. 1.7 (d)). The testbed comprises a stator, a guide rail, a load balance, a balance box, and a parallel link that connects the load balance and the wheel. The load balance moves across the guide rail [71]. Panels (e) and (f) of Fig. 1.7 show the specialized single-wheel testbeds developed by the German Aerospace Center (DLR) and the Carnegie Mellon University (CMU), respectively [72] [73].

1.3.3 Terramechanics-based Mobility Control

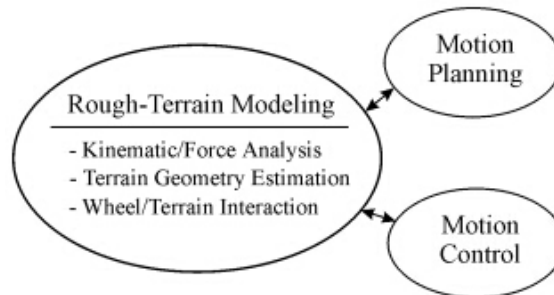


Figure 1.8. Physics-based approach [1].

Future exploration missions will require mobile robots to perform difficult tasks on challengeable terrains, with limited human supervision. However, most motion control algorithms do not consider the physical characteristics of the robot and its environment, which restricts their effectiveness on soft terrains. Facing this problem, Iagnemma pointed that advanced control methods must be developed that consider the physical characteristics

of the robot and its environment, and thus fully utilize the robot’s physical capabilities [1], as shown in Fig. 1.8. Thereafter, researchers have focused on terramechanics-based control that considers the wheel/lug-soil interaction mechanics.

Iagnemma proposed a rough terrain-control methodology for wheeled robotic vehicles [74]. This algorithm exploits the actuator redundancy of multi-wheeled mobile robot systems to improve ground traction and reduce power consumption. To limit the wheel slip and improve the climbing capabilities, they proposed a quasi-static model of a six-wheeled robot and a method that selects the optimal torques subject to the system constraints (the maximal and minimal torques and positive normal forces) [75]. Yoshida et al. investigated the kinetic behavior of a planetary rover traversing rough natural terrain, considering the wheel-soil traction mechanics and articulated body dynamics. They also developed an effective control law that reduces wheel slippage and improves traversability [76]. Ishigami et al. [77] proposed two control approaches for exploration rovers traversing sandy-sloped terrains; model-based feed-forward control and sensor-based feedback control. They experimentally identified the advantages and disadvantages of both approaches and discussed the possibility of merging them into an improved control system. Many alternative methods are being proposed, and terramechanics-based mobility control is becoming a new research hotspot.

1.4 Motivation and Outline of this Thesis

While rolling on sandy terrains, the conventional fixed lugged wheel inevitably generates unwanted oscillations in the tracking force, vertical force and wheel sinkage of lightweight vehicles, as the individual lugs interact with the soil. The oscillations will compromise the stability of the robot.

This motivated us to build a new form of wheel to overcome the limitations of the conventional wheeled robot by actively actuating its lug trajectory. To clearly understand the effects of lug motion on lug-soil interaction forces, experimental study and analysis

are performed in this thesis. The findings would be useful for estimating the traveling performance of locomotive mechanism equipped with lugs, modeling interaction mechanics between lugged wheels and soil, etc. The developed wheel can be used as the locomotive module of mobile robot for undertaking high-risk scientific exploration tasks in sandy environments.

Chapter 2 introduces the principle, kinematic model, lug-soil interaction process, force analysis and prototype of the Active Lugged Wheel (ALW) mechanism. In addition, based on the kinematic and dynamic models of four-wheel-robot, we discuss the possibility of ALW-based robot for achieving better traveling performance than conventional wheeled robot.

Chapter 3 presents an experimental study to confirm the effects of lug motion on lug-soil interaction forces. Horizontal force and vertical force acting on a single lug are measured as functions of inclination angle, sinkage length, horizontal displacement, and traveling speed. The experimental results are mathematically fitted by using least square method to facilitate quantitative analyses on effects of changes in these motion parameters. Moreover, we experimentally confirm how the soil deformation contributes to the lug-soil interaction forces.

Chapter 4 measures drawbar pull and vertical force on ALW prototype equipped with a single lug undergoing a complete interaction process to investigate the effect of the lug inclination angle and lug sinkage length. While the ratio of drawbar pull to vertical force is calculated to discuss the effects of the lug inclination angle, the maximum values are mathematically fitted by using least square method to quantitatively analyze the effect of the lug sinkage length.

Chapter 5 highlights the advantages of the ALW mechanism. By comparing the drawbar pull and vertical force generated by a smooth wheel, a lugged cage wheel, and the ALW, the interference between the wheel rim and lug, and the effects on force improvement of lugged wheels are discussed. In addition, six trajectories are further given, by which the developed mechanism can reduce the fluctuations of drawbar pull by tuning the sinkage length of the

active lug. The validity is experimentally verified by comparing its generated drawbar pull and vertical force with that generated by a fixed lugged wheel.

Chapter 6 concludes this thesis and discusses the possible works in the future.

Chapter 2

Principle and Prototype of the Active Lugged Wheel

Wheeled robot have been developed to access sandy environments in planetary explorations and geological investigations for its simplicity, reliability and efficiency. However, they easily slip and become trapped on such soft terrains, which may result in mission failure. Significant efforts have been made to improve the traveling performance of wheeled robots, and thereby undertake complex scientific exploration tasks on challenging terrains.

Attaching lugs can significantly enlarge the drawbar pull of the wheeled robot to reduce the slippage. However, lugged wheels inevitably generate unwanted oscillations in the sinkage, drawbar pull, and driving torque of lightweight vehicles as the individual lugs interact with the soil, which compromise the stability of the robot. It has been verified that the traveling performance of the wheeled robot can be improved by tuning the lug trajectory, which inspired us to propose a novel wheeled mechanism that overcomes the limitation of conventional wheeled robots by actively actuating the lugs.

This chapter first conceptualizes the Active Lugged Wheel (ALW), then introduces the kinematic model, the lug-soil interaction process, force analysis on soft terrains, and a mechanism prototype. Based on the kinematic and dynamic models of a four-wheeled robot,

we finally discuss whether the ALW-based robot can achieve better traveling performance than the conventional wheeled robot.

2.1 Concept of the Active Lugged Wheel

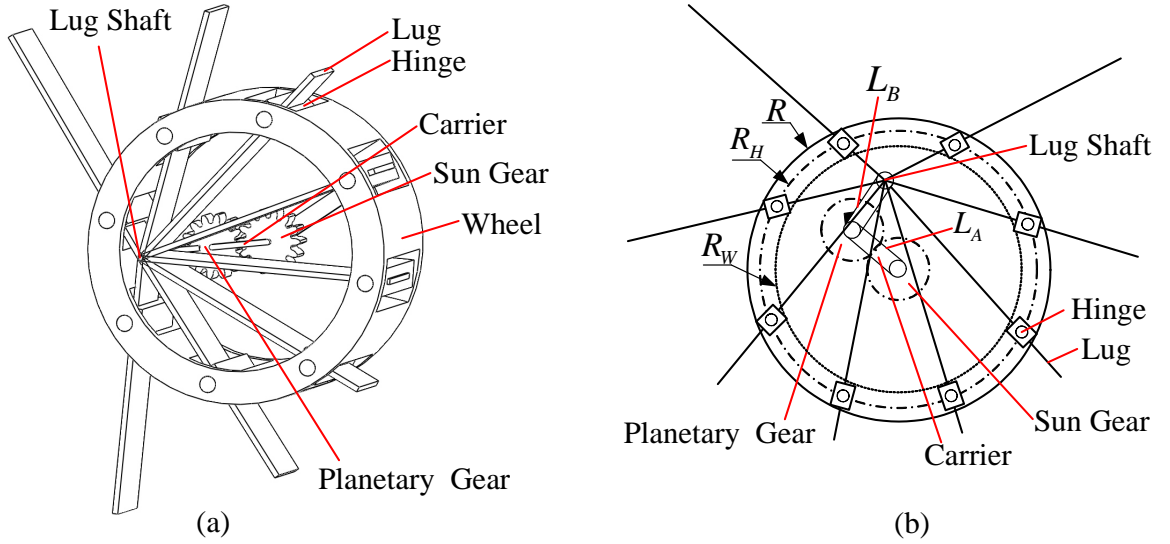


Figure 2.1. Schematic of the ALW: (a) mechanism, (b) kinematic diagram of ALW with eight active lugs.

The ALW concept, first proposed in [78], extends the amphibious ePaddle mechanism to operation on soft terrains [79]. The ALW module comprises a wheeled shell and a set of lugs, and has three degrees of freedom (Fig. 2.1 (a)). The main components are described below.

- i. A rotational joint driven by a motor for rotating the wheel shell. The hinges can passively rotate around the shaft affixed to the wheel rim, allowing retraction or protrusion of the lug through the hinge.
- ii. A planetary gear mechanism with a sun gear and a carrier actuated by two motors. This mechanism moves the lug shaft that is fixed on a disk integrated with the planetary gear. The center distance L_A between the two gears equals the center distance

L_B between the planetary gear and the lug shaft; thus, the lug shaft can arrive at any position within a circle of radius $R_W = L_A + L_B$ as shown in Fig. 2.1 (b).

The wheel, carrier, and sun gear are separately driven by three DC brushed motors, each with its own transmission system. As the wheel rolls forward, the position of the lug shaft changes, and the lugs are actively protruded or retracted through the hinges.

2.2 Kinematics of the ALW Mechanism

In this section, we focus on kinematically modeling the relationship between lug inclination angle, lug sinkage length and three joint angles of the ALW mechanism.

2.2.1 Inclination Angle and Sinkage Length

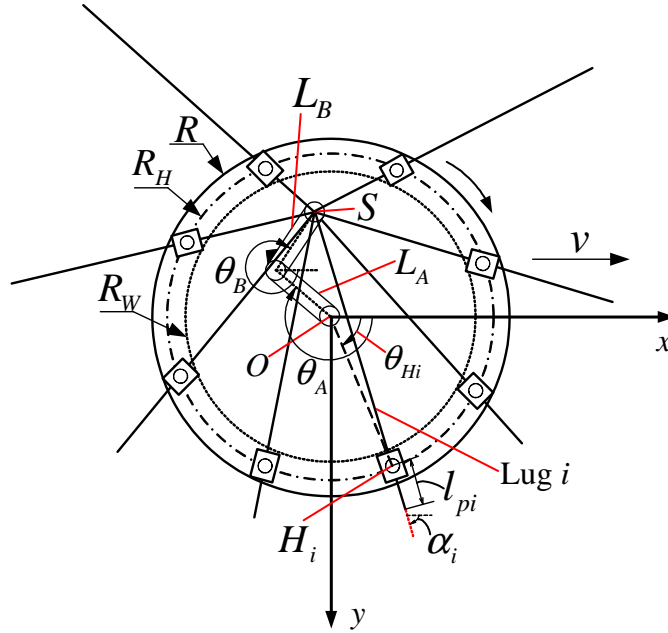


Figure 2.2. Wheel coordinate system.

The wheel coordinate system in the sagittal plane of the wheel is illustrated in Fig. 2.2. The origin is fixed at the wheel center, and the horizontal and vertical directions are denoted

by x and y , respectively. The coordinate frame is rotationally stationary with respect to the driving motion of the wheel.

The motion of the ALW mechanism can be denoted by the motion of three components, the wheel, the lugs, and the hinges. They all can be treated as rigid bodies. For the ALW mechanism with n lugs and n hinges (where an ALW mechanism with 8 lugs are demonstrated), the following basic points are used to denote its motion: center of the wheel O , center of the lug shaft S , center of the i -th hinge H_i .

The protruded length l_{pi} and inclination angle α_i of the i -th lug ($i=1,2,\dots,8$) are derived from three joint angles, θ , θ_A and θ_B . Note that, hereinafter, we use angular position of the 1-th hinge θ_{H1} as the angular position θ of the wheel rim (i.e. $\theta = \theta_{H1}$). The angular positions of the other hinges for the ALW mechanism with 8 lugs can be subsequently calculated as follows:

$$\theta_{Hi} = \theta_{H1} - (i - 1) \times 45^\circ = \theta - (i - 1) \times 45^\circ \quad (2.1)$$

In the first step, the positions of the lug shaft S and the i -th hinge H_i are given by

$$\mathbf{S} = \begin{bmatrix} x_s \\ y_s \end{bmatrix} = \begin{bmatrix} L_A \cos \theta_A + L_B \cos \theta_B \\ L_A \sin \theta_A + L_B \sin \theta_B \end{bmatrix} \quad (2.2)$$

$$\mathbf{H}_i = [x_{Hi}, y_{Hi}]^T = [R_H \cos \theta_{Hi}, R_H \sin \theta_{Hi}]^T \quad (2.3)$$

Next, we obtain the protruded length l_{pi} in (2.4) and inclination angle α_i in (2.5) of the i -th lug. The protruded length is the length from the hinge to the lug tip, and the inclination angle is the angle between the lug and the horizontal direction, as shown in Fig. 2.2.

$$l_{pi} = L - \sqrt{(x_{Hi} - x_S)^2 + (y_{Hi} - y_S)^2} \quad (2.4)$$

$$\alpha_i = \text{atan2}(y_{Hi} - y_S, x_{Hi} - x_S) \quad (2.5)$$

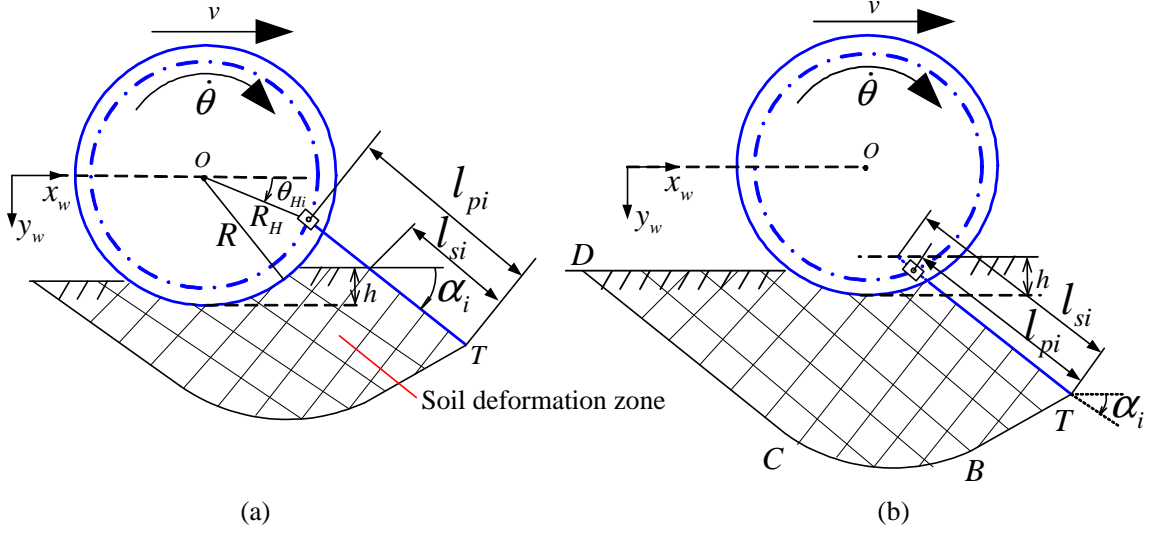


Figure 2.3. Relationship between the protruded length l_{pi} and sinkage length l_{si} when the lug has sunk into the soil (a) partly and (b) completely.

As shown in Fig. 2.3 (only the i -th lug is denoted for clarity), when the ALW is rolling on the soft terrain with constant wheel sinkage h , we describe the lug trajectory in terms of an sinkage length l_{si} rather than l_{pi} for simplicity. The lug sinkage length determines the contact area between the lug and the soil. Before the lug completely sinks into the soil, its rear part is above the soil surface (Fig. 2.3 (a)), and thus, the sinkage length l_{si} is smaller than the protruded length l_{pi} . According to terramechanics, cohesion and friction forces along the slip line (connecting points TBCD in Fig. 2.3 (b)) induce the soil-lug reaction force, which continues from the lug tip to the soil surface. The start point is determined by the depth plunged by the lug tip, so l_{si} exceeds l_{pi} when the lug has completely sunk into the soil. In both conditions, the sinkage length l_{si} is determined from the y-coordinate of the i -th lug tip, representing the depth sunk by the i -th lug, as

$$l_{si} = \frac{y_{Ti} - (R - h)}{\sin \alpha_i} = l_{pi} - \frac{R - h - R_H \sin \theta_{Hi}}{\sin \alpha_i} \quad (2.6)$$

Because each wheel module has three degrees of freedom, it can control the sinkage length and inclination angle of one lug only at a certain angular position of the wheel. The motions of the remaining lugs are determined accordingly.

2.2.2 Inverse Kinematic Model

Given the desired inclination angle and sinkage length of the i -th lug at angle θ_{Hi} of the wheel rotation, an inverse kinematic model is used to calculate the desired joint parameters θ_A and θ_B . First, the corresponding position of the lug shaft is calculated by (2.7).

$$\mathbf{S} = \begin{bmatrix} x_S \\ y_S \end{bmatrix} = \begin{bmatrix} R_H \cos \theta_{Hi} - (L - l_{si} - \frac{R - h - R_H \sin \theta_{Hi}}{\sin \alpha_i}) \cos \alpha_i \\ R_H \sin \theta_{Hi} - (L - l_{si} - \frac{R - h - R_H \sin \theta_{Hi}}{\sin \alpha_i}) \sin \alpha_i \end{bmatrix} \quad (2.7)$$

Combining this with (2.2), two solutions can be obtained for the joint angles in (2.8).

$$\begin{cases} \theta_A = \text{atan2}(y_S, x_S) \pm \text{acos} \frac{x_S^2 + y_S^2 + L_A^2 - L_B^2}{2L_A \sqrt{x_S^2 + y_S^2}} \\ \theta_B = 2\theta_A - \text{atan2}(y_S - L_A \sin \theta_A, x_S - L_A \cos \theta_A) \end{cases} \quad (2.8)$$

2.2.3 Workspace Analysis

It should be noted that no solutions exist if S is out of the annulus with an inner radius of $L_A - L_B$ and an outer radius of $L_A + L_B$. Therefore, θ_A and θ_B exist if the coordinates of S satisfy the following.

$$L_A - L_B \leq \sqrt{x_S^2 + y_S^2} \leq L_A + L_B \quad (2.9)$$

where x_S and y_S are the functions of l_{si} and α_i as specified by (2.7).

In addition, like a two-link serial manipulator, the center and the boundary of the workspace are the singularities in which the joint parameters no longer completely define the position of the lug shaft. The angular speed of the joint angle will sharply change when the lug shaft moves close to these singularities.

2.3 Locomotion on Soft Terrains

2.3.1 Versatile Locomotion Modes

By integrating the wheel and lug motions, our proposed ALW mechanism controls the lug trajectory, and thus improves the traveling performance of the wheel. Depending on the environmental conditions, the ALW selects one of the three motion modes by repositioning its lug shaft. Because of its versatile motion, the ALW-based robot is an ideal mobile platform for undertaking high-risk scientific exploration tasks in sandy environments. The three motion modes are briefly described below and illustrated in Fig. 2.4.

Smooth wheeled mode (Fig. 2.4 (a)): a smooth wheel-like motion is achieved by maintaining good contact between the ground and the outer surface of the shell and adopting a rolling motion. The lug shaft is placed at the upmost position to prevent the lugs from punching the ground. This mode is suitable for rolling on compacted terrain on which the robot might be effectively propelled by friction between the wheel surface and ground. In this case, the lugs should be completely retracted into the wheel; otherwise, the robot body will be periodically affected by lug-ground interactions on the rigid surface.

Fixed lugged wheeled mode (Fig. 2.4 (b)): to achieve a fixed lugged wheel-like motion, the lug shaft is coincided with the wheel center, and both motors of the planetary gear mechanism are locked. This mode requires no additional lug trajectory control strategy and is controllable by many existing approaches. However, as mentioned earlier, this type of wheel inevitably generates unwanted oscillations in the sinkage, force, and torque of lightweight vehicles as the individual lugs interact with the soil, which compromise the stability of the robot.

Active lugged wheeled mode (Fig. 2.4 (c)): while the smooth and fixed lugged wheel modes are conventional modes, this is a unique locomotion mode in which the lugs are actively protruded outward from the wheel and inserted into the soil. This mechanism gains drawbar pull and vertical force. The performance improvement of a device operated in this mode constitutes the main topic of this thesis.

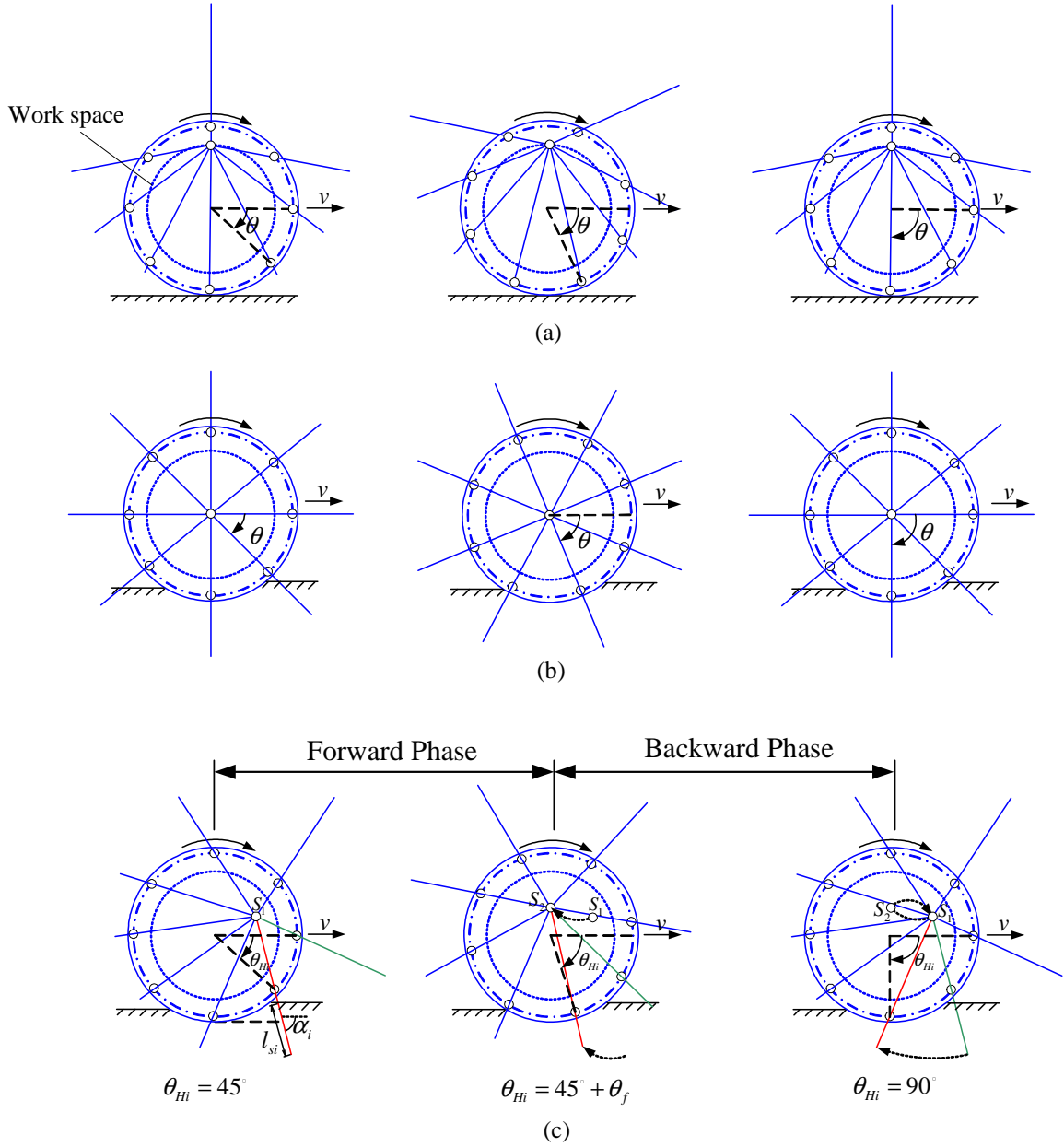


Figure 2.4. The ALW mechanism operates in three modes on soft terrains: (a) smooth wheeled mode, (b) fixed lugged wheeled mode, (c) active lugged wheeled mode (the working lug is highlighted in red).

2.3.2 Lug-soil Interaction Process in Active Lugged Wheeled Mode

By the above analysis, we can tune the lug trajectory as the ALW moves in active lugged wheeled mode. As mentioned in Sec. 2.2, we can tune the lug trajectory as the ALW moves in active lugged wheeled mode. The sinkage length and inclination angle of an individual lug can be controlled only at a specific angular position of the wheel. In this thesis, the controlled lug is called the working lug. During the wheel rotation, each of the eight lugs sequentially becomes the working lug.

An example of the lug-soil interaction process is shown in Fig. 2.4 (c). As the wheel rotates through one turn, each of the eight lugs sequentially becomes the working lug and the lug shaft reciprocates between S_1 and S_2 . In the eight-lug configuration, one reciprocation is completed every 45° ($45^\circ = 360^\circ / 8$). In this example, the i -th lug becomes the working lug when

$$45^\circ \times i \leq \theta < 45^\circ \times (i + 1) \quad (2.10)$$

From (2.1), we have

$$45^\circ \leq \theta_{Hi} < 90^\circ \quad (2.11)$$

Each reciprocation is subdivided into two phases, **forward phase** and **backward phase**, which operate within the angular ranges θ_f and θ_b , respectively ($\theta_f + \theta_b = 45^\circ$).

As θ_{Hi} proceeds from 45° to $(45^\circ + \theta_f)$, the working lug (the i -th lug, highlighted in red in Fig. 2.4 (c)) is controlled at the desired inclination angle and sinkage length. At the switch point where $\theta_{Hi} = 45^\circ + \theta_f$, the lug shaft arrives at point S_2 .

As θ_{Hi} proceeds from $(45^\circ + \theta_f)$ to 90° , the lug shaft returns to its initial point S_1 and the succeeding lug (highlighted in green in Fig. 2.4 (c)) becomes the working lug.

If the relationship between the lug trajectory and force is known, we can calculate the sinkage length and inclination angle of the working lug at each sampling point of the angular

wheel position from the given required drawbar pull. The positions of the lug shaft are then obtained from the kinematic model described in Sec. 2.2. At any particular angle θ , the position of the lug shaft can be adjusted to achieve the desired inclination angle and sinkage length of the working lug.

2.4 ALW-soil Interaction Force

Smooth-wheeled vehicles easily slip and lose traction on soft terrains, whereas legged robots tend to sink because the foot lacks sufficient support area. Unlike these terrestrial mobile robots, the ALW mechanism achieves sufficient supporting force to overcome sinkage of the wheel rim. The drawbar pull and vertical force are further enhanced by the insertion of the lugs into the soil. Essentially, the motion state of the mobile robot depends on the interaction forces between the locomotive module and soil. This section analyzes the forces exerted on the ALW module by the soil.

2.4.1 Wheel-soil Interaction Force

As the wheel rolls over soft terrain, its sinkage introduces a normal stress σ under the wheel, and its shearing motion relative to the ground generates a shear stress τ . The force model describing the smooth wheel on loose soil is schematized in Fig. 2.5 (a). The drawbar pull F_p^W acts in the longitudinal direction and is calculated by integrating the normal stress σ and shear stress τ from the entry angle θ_r to the exit angle θ_e .

$$F_p^W = RB_W \int_{\theta_r}^{\theta_e} \{\tau(\theta) \sin \theta - \sigma(\theta) \cos \theta\} d\theta \quad (2.12)$$

where R and B_W are the wheel radius and width, respectively.

The vertical force F_v^W is calculated as follows.

$$F_v^W = RB_W \int_{\theta_r}^{\theta_e} \{\tau(\theta) \cos \theta + \sigma(\theta) \sin \theta\} d\theta \quad (2.13)$$

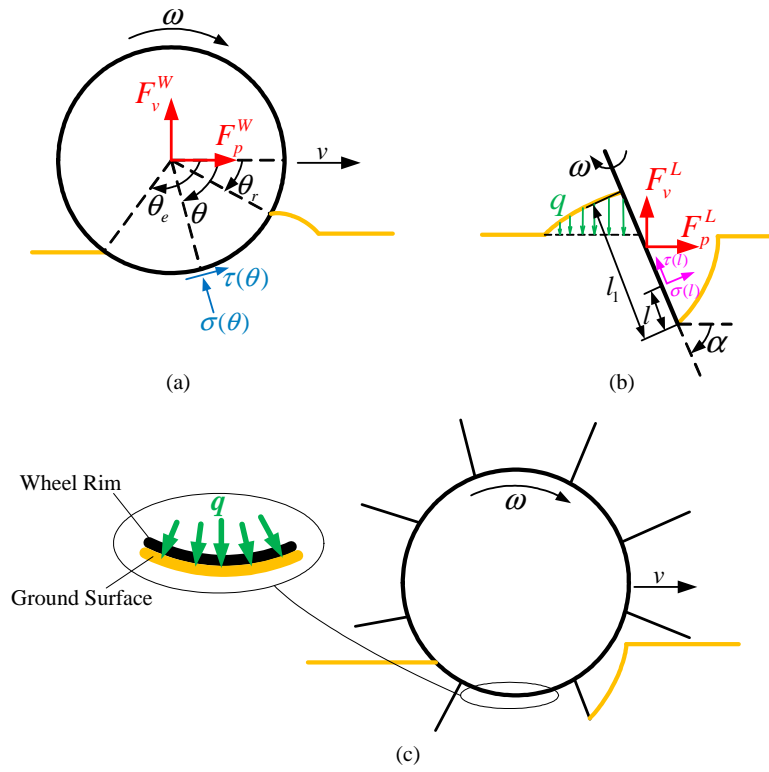


Figure 2.5. Stress model of (a) the wheel rim, (b) the lug, (c) the ALW module on soft terrain.

The normal and shear stresses are calculated from Bekker's formula [53] and the Janosi-Hanamoto equation [80], respectively. The validity of these expressions has been experimentally verified in many reports.

2.4.2 Lug-soil Interaction Force

As the lug is inclined into the soil, the pushing movement and relative shearing generate a normal reaction stress σ and a shearing stress τ , respectively. The horizontal force F_p^L and vertical force F_v^L are calculated by integrating the stresses σ and τ over the contacting area of the lug.

$$F_p^L = B_L \int_0^{l_1} \{\sigma(l) \sin \alpha - \tau(l) \cos \alpha\} dl \quad (2.14)$$

$$F_v^L = B_L \int_0^{l_1} \{\sigma(l) \cos \alpha + \tau(l) \sin \alpha\} dl \quad (2.15)$$

where B_L and α denote the lug width and inclination angle, respectively.

As the lug begins digging into the soil, the lug-soil interface and the interior soil structure are deformed to varying extents. Such deformation fills some of the voids in the random sand structure with moving sand grains, increasing the local soil density around the lug-soil interaction area. As the soil is further compressed, the portion in front of the lug slowly swells from the ground and its weight applies an additional pressure q to the terrain surface (Fig. 2.5 (b)). Both the altered soil density and the pressure q affect the lug-soil interaction force. The lug forces in such a complicated soil failure pattern are difficult to model, and their interaction mechanics have yet to be described by a robust theory. Facing this challenge, experiments were conducted to investigate the effects of lug motion on lug forces. The detailed results will be presented in Chapter 3.

2.4.3 ALW-soil Interaction Force

The ALW-soil interaction force is the sum of the forces acting on the wheel rim and the lugs. The ALW-soil interaction force is difficult to predict because the motion behaviors of the wheel rim and lugs significantly interfere. As shown in Fig. 2.5 (c), the wheel imposes an additional stress q on the soil free surface that further enhances the lug-soil interaction forces than a single lug. In contrast, the normal and shear stresses acting on the wheel rim depend on the motion of the lug that digs and changes the soil structure beneath the wheel. The ALW-soil interactions are experimentally investigated and characterized in Chapter 4.

2.5 Prototype Design of the ALW Mechanism

2.5.1 Mechanism Design of the ALW Module

The fabricated ALW prototype equipped with a set of eight lugs is shown in Fig. 2.6 (a), (b). To enhance their durability, the mechanism components were constructed from aluminum (AL5052, AL2017) or stainless steel (SUS303, SUS304). The ball bearings were double shield types to prevent contamination of the bearing raceways. The wool felt sheet was installed in two adjacent components, allowing relative movement between the components for dust sealing.

The main components of the ALW module is shown in Fig. 2.6 (c), and the specifications are listed in Table 2.1.

Transmission system

As shown in Fig. 2.7, the wheel rim, carrier, and sun gear are separately driven by three DC brushed motors (Maxon RE25, integrated with a GP gearbox (72:1)) via gears. The angular positions of the three joints are collected by three absolute encoders (RE22, RLS; Slovenia). The wheel rim is rotated by the first motor through a pair of flat gears. The position of the lug shaft is determined by the angular position of the carrier and sun gear of planetary gear mechanism which is plotted in Fig. 2.8.

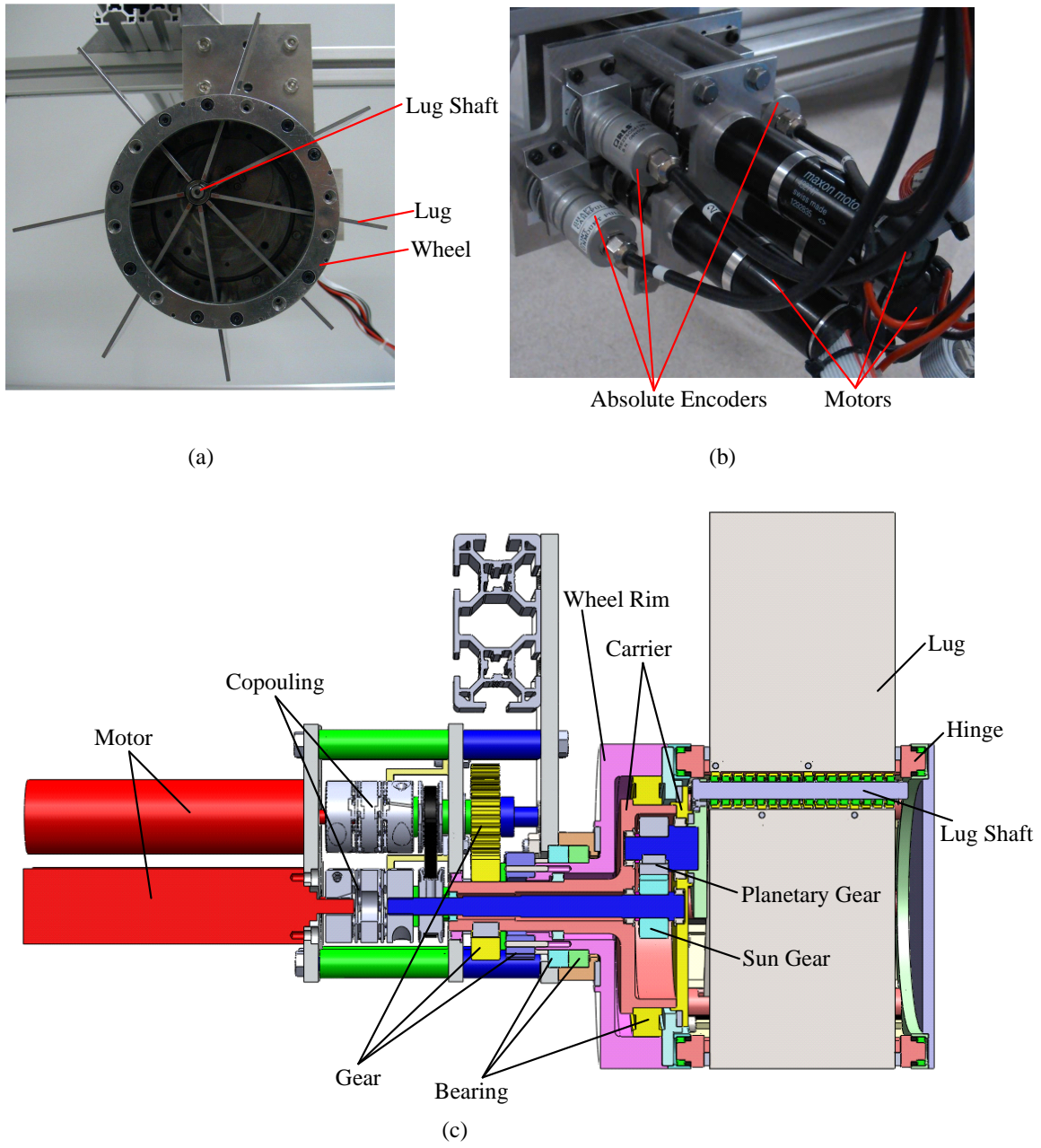


Figure 2.6. The ALW prototype: (a) front view, (b) rear view, (c) section view.

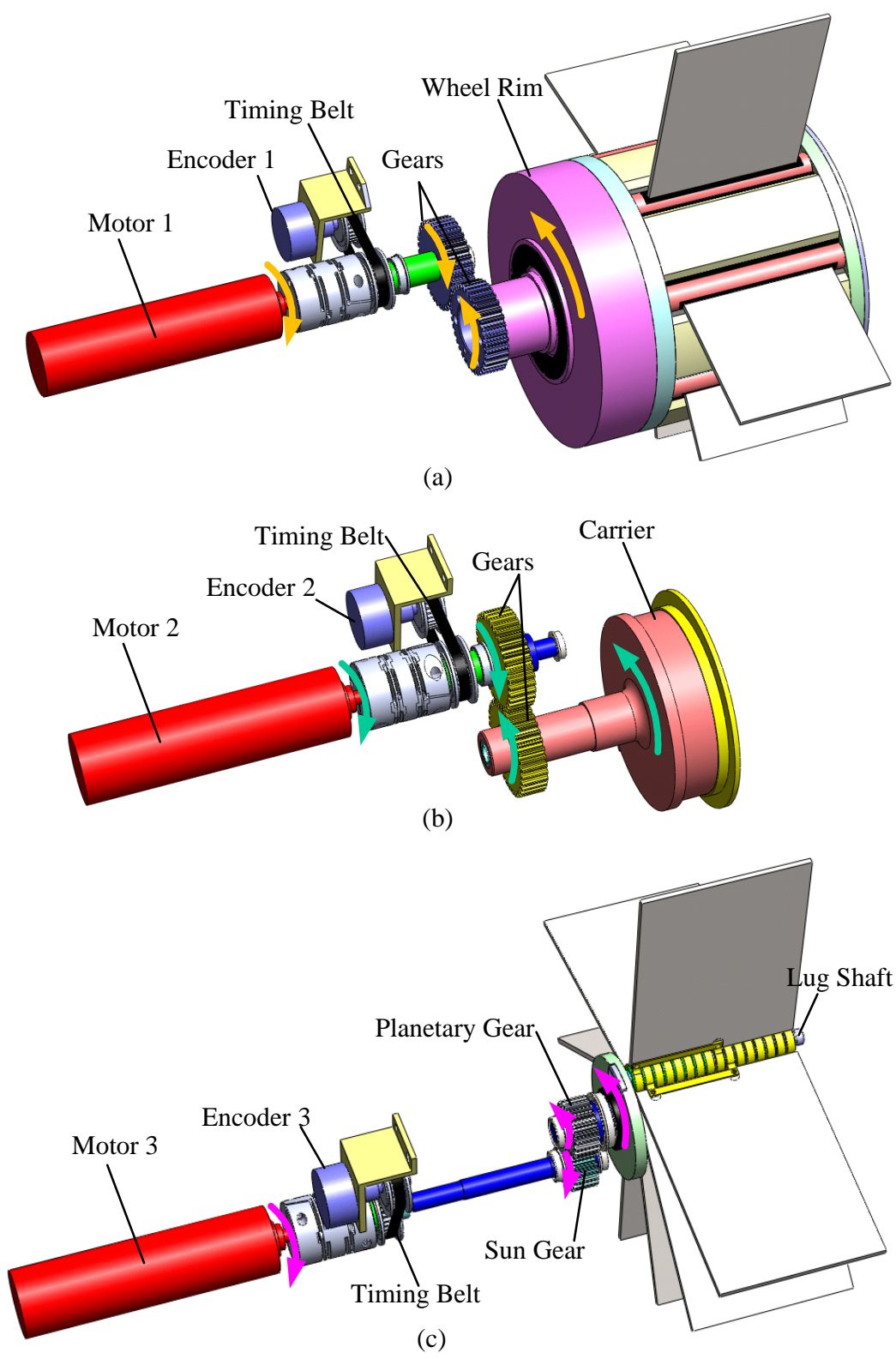


Figure 2.7. Transmission system of (a) wheel rim, (b) carrier, (c) sun gear.

Table 2.1. Specifications of the ALW module whose kinematical diagram is shown in Fig. 2.1 (b).

Parameters	Unit	Value
Lug length L	[mm]	89.5
Lug width B	[mm]	63
Lug thickness	[mm]	2
Shell radius R	[mm]	56
Shell width	[mm]	113
Lug hinges layout circle radius R_H	[mm]	50
Center distance L_A	[mm]	20
Lug shaft layout circle radius L_B	[mm]	20
Workspace radius R_W	[mm]	40
Mass of the ALW module	[kg]	3.2

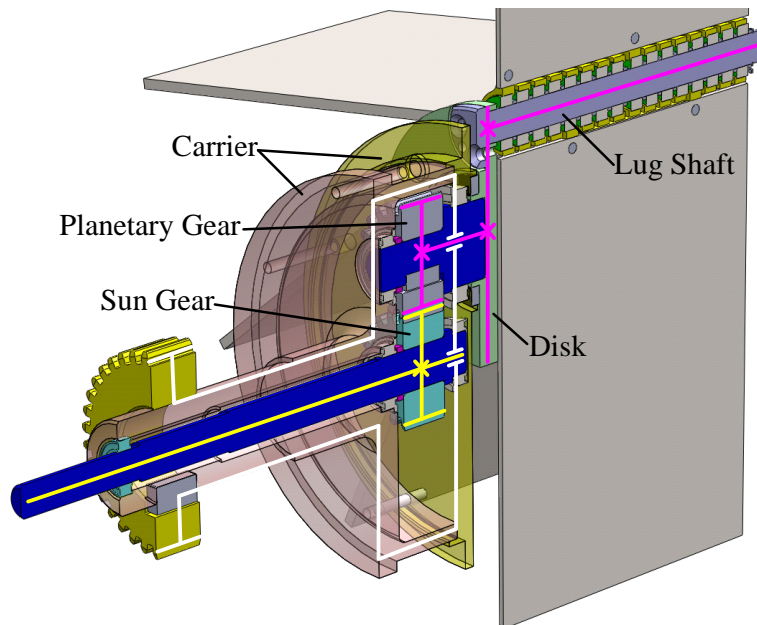


Figure 2.8. Planetary gear mechanism.

Lugs and Lug Shaft

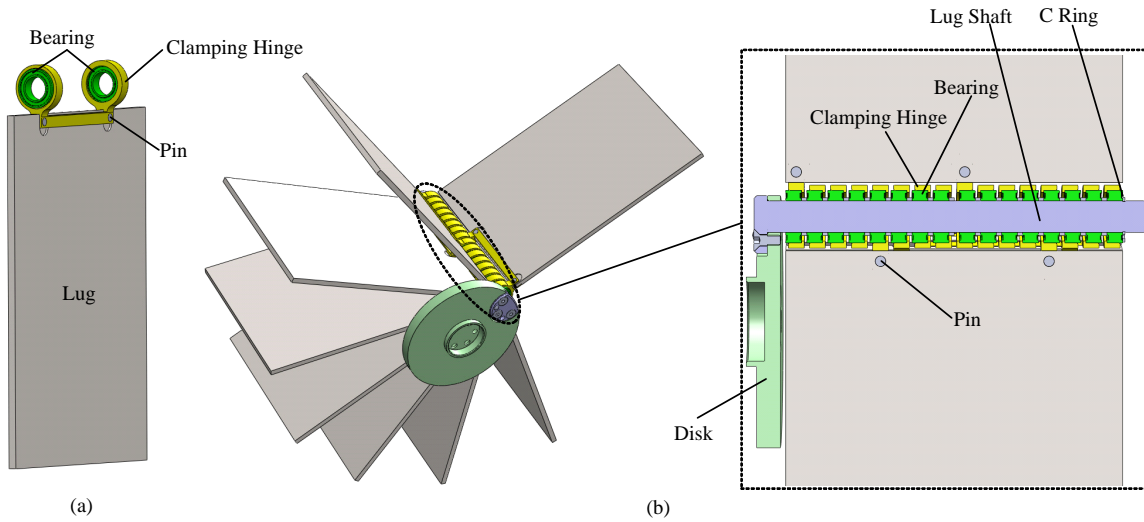


Figure 2.9. Lugs and lug shaft: (a) one set, (b) eight-lug configuration.

The stainless steel lug shaft is fixed to the disk integrated with the planetary gear by pins and bolts. As shown in Fig. 2.9, the lugs are made from rectangular rigid aluminum plates, and each lug is hung on the lug shaft by a clamping hinge. Ball bearings are assembled in the clamping hinge, ensuring smooth passive rotation of the lug around the lug shaft.

Wheel-like Shell

Fig. 2.10 shows the wheel-like shell constructed from two annulus frames, eight shell pieces, and eight hinges. The shells are fixed between the frames by stainless steel pins and bolts to form the wheel surface. The hinges, which freely rotate around their central axis, are supported between the frames by the bearings. The lug slides through a hole inserted in the hinge. For dust-proofing, the clearances between the lug and the hinge and between the hinge and the shell are filled with woolen felt sheets. The outer surface of the wheel is polished for intended future adhesion of rubber tire.

2.5.2 Controller Design of the ALW Module

Schematic blocks of developed controller is shown in Fig. 2.11. The motors driving the ALW joint angles are controlled by a dsPIC33FJ128MC804-based controller (Microchip;

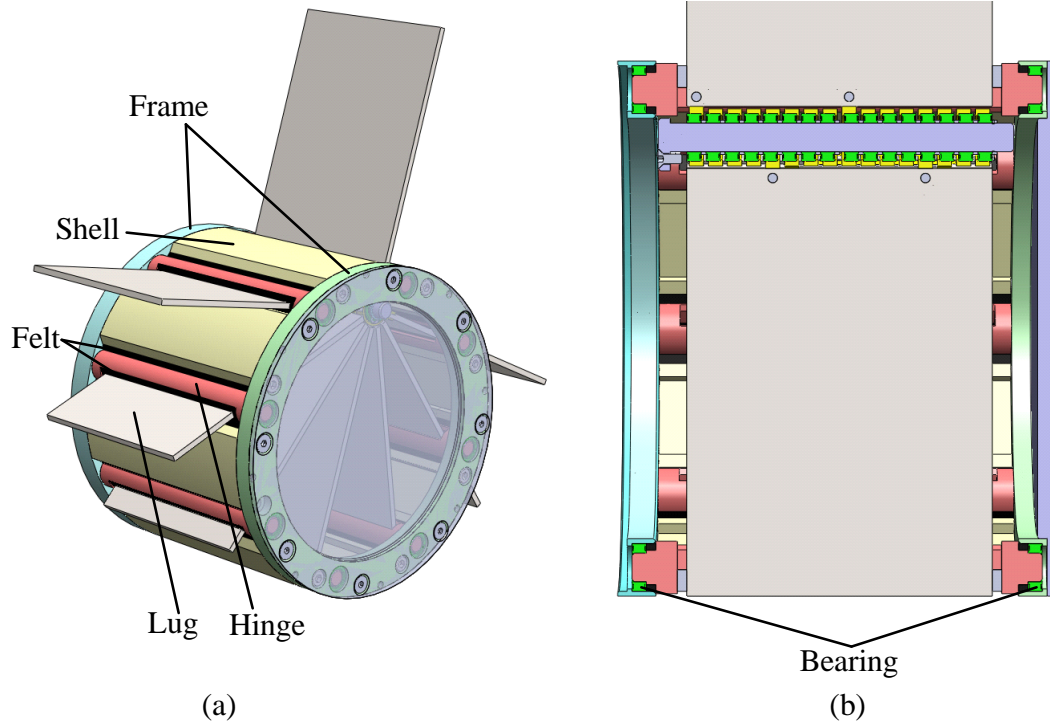


Figure 2.10. Wheel-like shell: (a) 3D view, (b) section view.

USA), and each of them is individually driven by a LMD18200 based motor driver (National Semiconductor; USA). The controller adopts a real-time proportional-integral-derivative-based (PID-based) algorithm with position regulation for controlling the servo motors. In all experiments, the desired trajectories of three joints are downloaded into the controller in advance. Fed by signals from the absolute encoders, PWM signals are generated by position servo algorithm in the controller and amplified by the motor drivers to control the motors.

2.6 ALW-based Mobile Robot

2.6.1 Concept

A four-ALW-robot is under fabrication. The prototype is installed with 12 DC brushed motors. As shown in Fig. 2.12, four modules are rigidly connected by three aluminum frames before obtaining the optimal length, width, and height of the robot body. The front-rear wheel and left-right wheel separations are 400 mm and 630 mm, respectively.

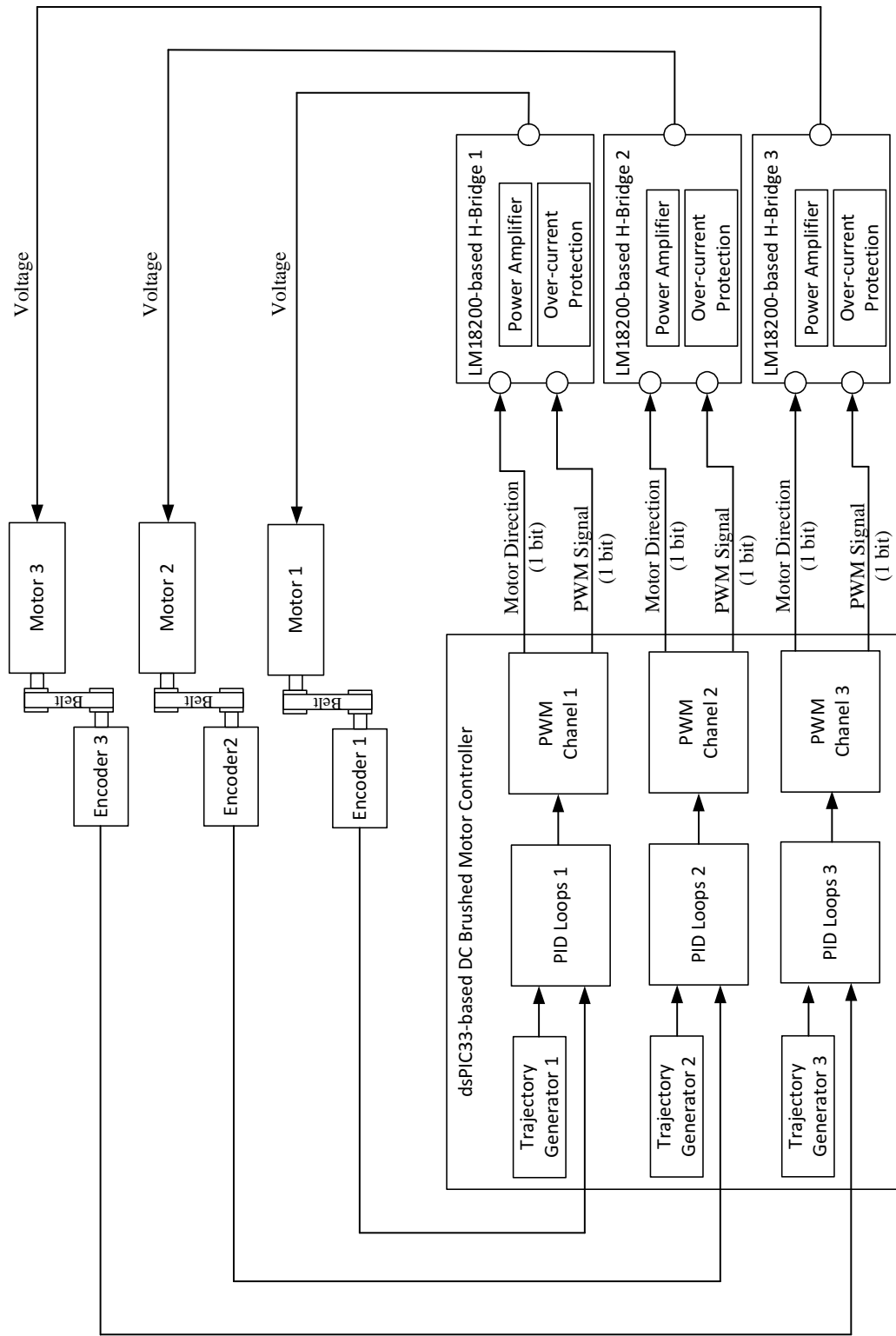


Figure 2.11. The schematic blocks of the proposed dsPIC-based motion controller.

The ALW-based robot will not be detailed in this thesis. This section briefly states the problems and challenges of a mobile robot traversing sandy terrains in the form of a simple example. The requirements of the locomotive module and possible solution by the ALW mechanism are discussed.

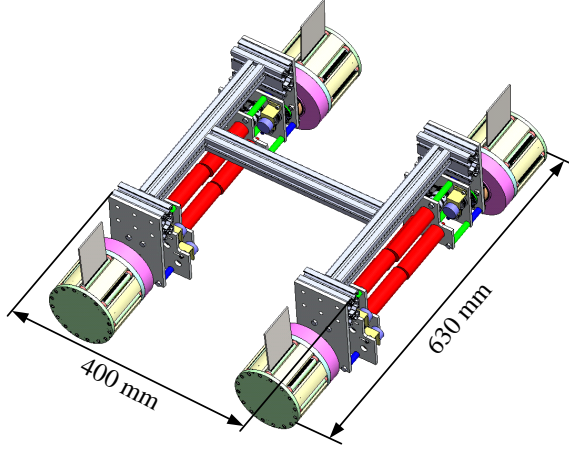


Figure 2.12. Prototype of four-ALW-robot.

2.6.2 Control Problem Statement

The example assumes a skid-steered vehicle in which only the motion and forces in the $x_w - y_w$ plane of the vehicle are important. In the kinematic and dynamics models, we make four further assumptions.

- i. The distance between the wheels is strictly fixed.
- ii. The rolling axle of each wheel is parallel to the terrain surface.
- iii. The vehicle contains no flexible parts.
- iv. The soft terrain is even, i.e., the pitch angle of the vehicle remains at 0.

The subscript i in Fig. 2.13 identifies the wheel ($i = 1$ or 2). The velocity of the centroid of the vehicle is denoted as (v_{x0}, v_{y0}) , and v_{xi}, v_{yi} are the velocity components of wheel i . l_f and l_r represent the longitudinal distances from the centroid of the vehicle to the front

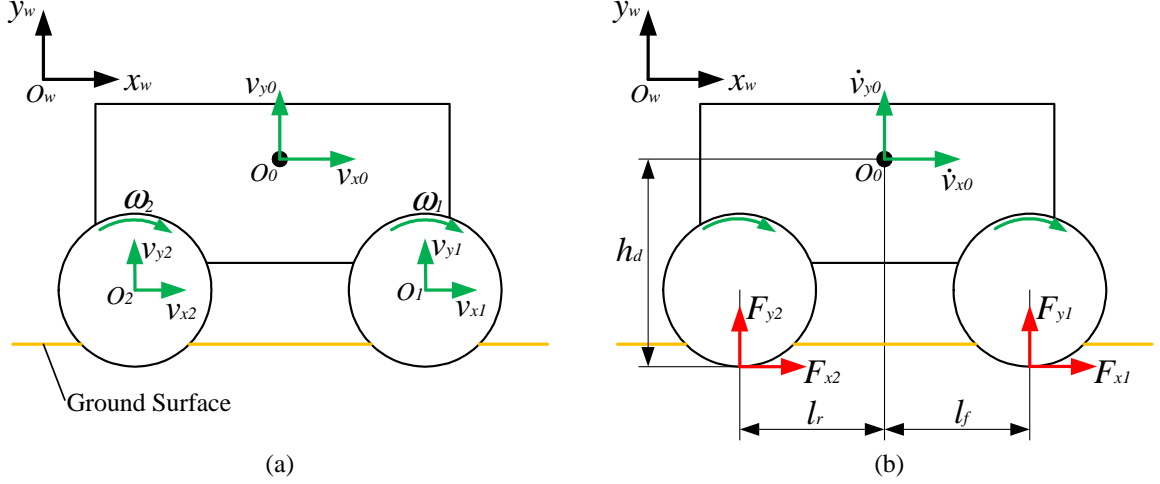


Figure 2.13. (a) Kinematic model and (b) dynamic model of the four-wheel-robot.

and rear wheels, respectively (in this case, $l_f = l_r$). h_d is the vehicle height. The constraint conditions of the kinematic model are as follows.

$$\begin{cases} v_{x1} = v_{x2} = v_{x0} \\ v_{y1} = v_{y2} = v_{y0} = 0 \end{cases} \quad (2.16)$$

The dynamic motion equations of the vehicle are as follows.

$$\begin{cases} M \cdot \dot{v}_{x0} = F_{x1} + F_{x2} \\ M \cdot \dot{v}_{y0} = F_{y1} + F_{y2} - G \\ J \cdot \dot{\theta}_0 = 0 = F_{x1} \cdot h_d + F_{x2} \cdot h_d + F_{y1} \cdot l_f - F_{y2} \cdot l_r \end{cases} \quad (2.17)$$

where M and J represent the mass and inertia of the vehicle, respectively, and G denotes gravity. F_{xi} and F_{yi} in Fig. 2.13 (b) are the soil reaction forces acting at the i -th wheel.

The vehicle control for tracking desired trajectory consists of two parts:

- i. The first part calculates the wheel speed and contact force that reduces the trajectory tracking error. Given the desired parameters (v_{x0} , v_{y0} , \dot{v}_{x0} , \dot{v}_{y0}) of the vehicle body, the required velocity components v_{xi} , v_{yi} and forces F_{xi} , F_{yi} of the i -th wheel are

obtained from the vehicle control approach. This problem has been addressed in many publications.

- ii. The second part drives the single-wheel module to achieve the required $(v_{xi}, v_{yi}, F_{xi}, F_{yi})$. The longitudinal velocity v_i depends on the drawbar pull F_x and angular speed of the wheel rim. Note that, to simultaneously achieve the desired forces and angular speed, each wheel requires at least three degrees of freedom. Such flexibility is precluded in conventional wheeled robots. In Chapter 5, we will demonstrate that the ALW module achieves the desired rotational speed by rotating its wheel rim and tunes the soil reaction forces by controlling its lug trajectory.

2.7 Summary

This chapter introduced a novel wheel type called Active Lugged Wheel (ALW). Corresponding with the environments, the ALW can not only achieve two configurations as conventional wheels, smooth wheel and fixed lugged wheel, but also can actively actuate its lug trajectory to enhance the traveling performance further. Our system is suitable as a basic module in a mobile robot deployed in high-risk missions on soft terrains, such as planetary exploration and disaster rescue.

To fully conceptualize the ALW mechanism, we introduced the kinematic model and discussed the lug-soil interaction process and analysis of the ALW-soil interaction forces. We then designed and fabricated a prototype mechanism, including a transmission system, lug and lug shaft, and a wheel-like shell.

Finally, we stated by example the control problem and challenge of deploying a wheeled mobile robot in soft environments. To reduce the tracking error, each module of the robot must maintain the required rotational speed and forces. Conventional wheeled modules possess insufficient degrees of freedom to meet both requirements. In contrast, the ALW with greater maneuverability can potentially overcome these problems.

Chapter 3

Lug-soil Interaction Characteristics

Lugs are routinely attached to the surface of wheels of mobile robots to enhance their ability to traverse loose sandy terrains. Much previous work has focused on trying to understand how lug shape, such as height, width, etc. affects locomotion performance of the robots. However, unlike the shapes, which are generally determined during the design stage, lug trajectories change as robot performs its tasks. When trying to study the ALW-soil interaction mechanics at various lug trajectories, we did not find any acceptable model that can reliably predict lug forces from the lug motion state. This motivated us to conduct an experimental study to investigate the influence of various motion parameters on lug forces.

In this chapter, we measure horizontal and vertical forces acting on a single lug but without the wheel as functions of inclination angle, sinkage length, horizontal displacement, and traveling speed. The experimental results are mathematically fitted by using least square method to facilitate quantitative analyses on effects of changes in these motion parameters. In addition, an additional experiment is designed to help us to identify how the soil deformation affects the characteristics of lug-soil interaction forces. The conclusions from this chapter would be useful for analyzing the ALW-soil interaction characteristics that will be measured in Chapter 4.

3.1 Motion Parameters and Lug Forces

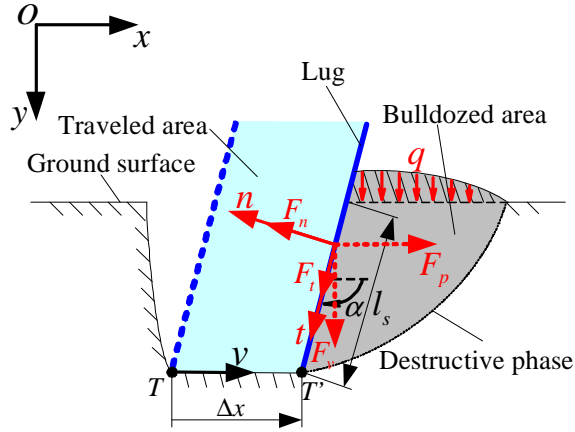


Figure 3.1. Motion parameters and force model for a single lug with translational motion.

As a rigid flat lug horizontally translates in a world coordinate system defined as shown in Fig. 3.1, its horizontal traveling direction is denoted by x . The influences of the following four motion parameters are measured as the lug's tip moves from T to T' .

- i. Translational speed v is the horizontal speed of the lug without rotational motion.
- ii. Horizontal displacement of the lug can be represented by the horizontal displacement Δx of the lug tip.
- iii. Sinkage length l_s determines the contact area between the lug and soil below the ground surface.
- iv. Inclination angle α is defined as the angle between the lug and horizontal direction that denotes the ratio of projected areas of the lug on the horizontal plane to the vertical plane.

Normal and tangential directions of the lug are denoted by n and t , respectively, in a local coordinate system fixed at the lug (Fig. 3.1). The magnitudes of incremental displacements Δt along (tangential to) and Δn perpendicular to (normal to) the lug can be calculated from Δx .

$$\Delta t = \Delta x \cos \alpha \quad (3.1)$$

$$\Delta n = -\Delta x \sin \alpha \quad (3.2)$$

A negative value of Δn means that the lug will push the soil, while the sign of Δt denotes the lug's direction of movement relative to the soil. Deformations of soil due to pushing movements in the normal direction and due to relative movements along the tangential direction of the lug generate reaction forces F_n and F_t , respectively. Thus, the horizontal force F_p and vertical force F_v can be obtained in (3.3).

$$\begin{bmatrix} F_p \\ F_v \end{bmatrix} = \begin{bmatrix} \cos \alpha & -\sin \alpha \\ \sin \alpha & \cos \alpha \end{bmatrix} \begin{bmatrix} F_t \\ F_n \end{bmatrix} \quad (3.3)$$

As the lug starts to dig into the soil, varying degrees of deformation occur along the lug-soil interface and within the soil structure. Under such deformations, some of the voids in the random sand structure are filled by moving sand grains, and thereby increasing the local soil density around the lug-soil interaction area. As the soil is further compressed, a portion in front of the lug slowly swells from the ground and the weight of the swelled soil applies an additional pressure q to the terrain surface (Fig. 3.1). Both the change in soil density and the pressure q affect the lug-soil interaction force. Therefore, it is difficult to model lug forces based on such a complicated soil failure pattern. Facing this challenge, experiments were conducted to measure the soil reaction forces acting on the lug generated by adopting various combinations of the motion parameters. Based on experimental results, this chapter provides a quantitative analysis of relationships between lug motion and forces.

3.2 Experimental Setup

3.2.1 Experimental Overview and Conditions

Unless otherwise mentioned, the following tests were done with a stainless steel lug having a length of 110 mm, width of 30 mm, and thickness of 1 mm. All combinations of motion parameters adopted in the experiments are tabulated in Table 3.1. Overall, they can be classified into two groups according to experimental purpose.

- i. Bulldozing experiment I (Fig. 3.2 (a)): the lug horizontally passes through the soil over a distance of 250 mm with constant inclination angle, sinkage length and traveling speed. The experimental results from adopting various inclination angles, sinkage lengths, and traveling speeds, can be used to investigate effects of the motion parameters on lug-soil interaction forces.
- ii. Bulldozing experiment II (Fig. 3.2 (b)): an additional process of removing swelled soil is involved. Once the lug has bulldozed the soil through the soil 250 mm with constant sinkage length (Fig. 3.2 (b)-(i)(ii)), the swelled soil is manually removed (Fig. 3.2 (b)-(iii)), the convey unit of the testbed is restarted under the same conditions (Fig. 3.2 (b)-(iv)(v)), and the lug travels a further 250 mm through the soil. The results from bulldozing experiment II can be used to determine how the soil deformation affects the lug-soil interaction forces.

Table 3.1. Values used for motion parameters in the experiments.

	Inclination angle α [$^{\circ}$]	Sinkage length l_s [mm]	Speed v [mm/s]
Bulldozing experiment I	90	30	2.5, 5, 7.5, 10
		10, 20, 40	10
	105, 120, 135	10, 20, 30, 40	10
Bulldozing experiment II	90, 120	30	10

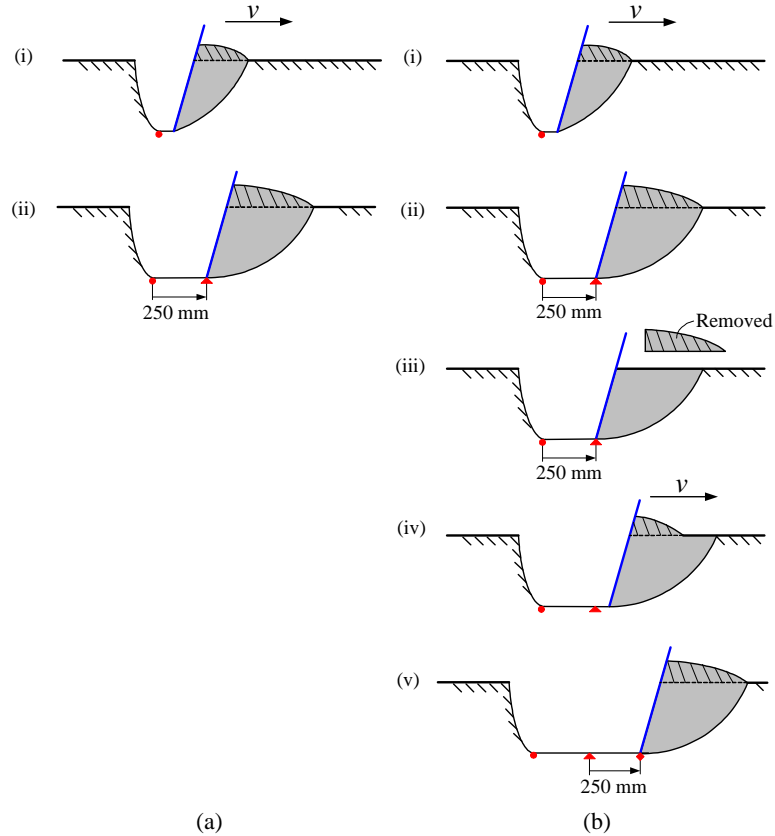
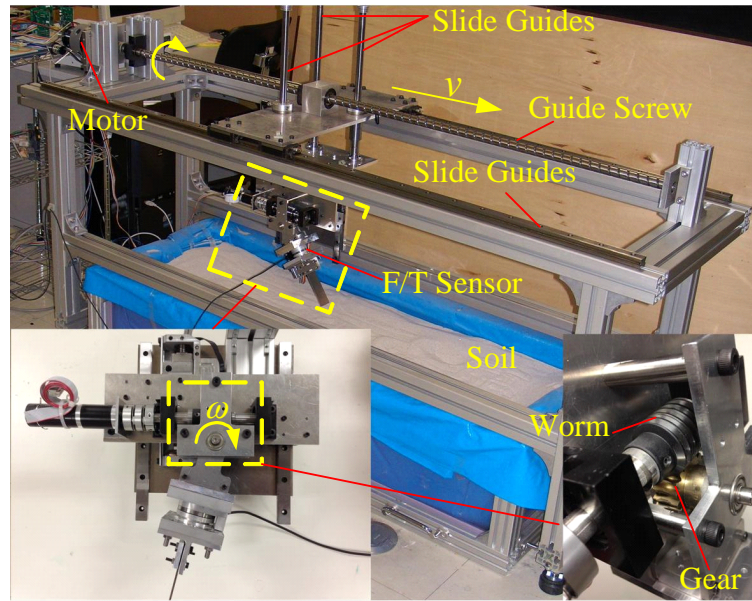


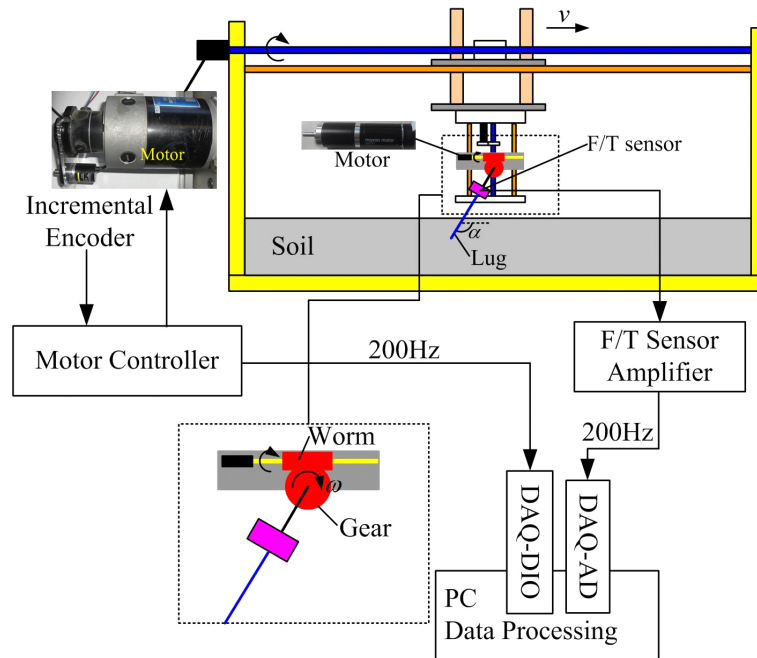
Figure 3.2. Experimental procedure of (a) bulldozing experiment I, (b) bulldozing experiment II.

3.2.2 Lug-soil Interaction Testbed and Soil Conditions

A testbed with length 1700 mm, width 500 mm, and height 800 mm was constructed for the measurements (Fig. 3.3). It contains a horizontal driving unit and a rotating unit. The lug can be manually set at a desired inclination angle in advance, and the angle can be fixed during the experiments due to the self-lock function of a worm gear mechanism. The horizontal driving unit were actuated along two slide guides at the desired speed by using a DC brushed servo motor via a screw. The angular position of the motor was collected by an incremental encoder. The data were sampled through a digital input/output board (NI-6001, National Instrument; USA) on a PC running a Windows XP operating system. In the vertical direction, the lug can be set to the desired sinkage length and then fixed by linear bushings affixed with clamp levers. A six-axis force/torque sensor (Mini 8/40, BL Autotec; Japan) connected the lug to the testbed and was used to measure the forces



(a)



(b)

Figure 3.3. (a) Lug-soil interaction testbed and (b) data acquisition system.

acting on the lug. The force signals were sampled by an A/D board (AD 12-16 (PCI), Contec; Japan). The sampling rate for data acquisition was 200 Hz. The relationship of lug motion and lug forces can be obtained by combining the data from the encoder and the force/torque sensor. It should be noticed that the signals from the force/torque sensor were the normal force and tangential force acting on the lug. The horizontal force and vertical force reported in this chapter were derived by (3.3) from the measured force signals.

Soft dry sand filled the sandbox of the testbed. It had been purified, sieved, ventilated, and dried. The physical and mechanical properties of the soil, measured by shearing experiments, and parameter identifications are listed in Table 3.2.

Table 3.2. Soil parameters.

Parameters	Value
Cohesion stress c (Pa)	400
Soil friction angle ϕ ($^\circ$)	38.1
Soil specific weight γ (kg/m^3)	1480
Adhesion stress c_a (Pa)	66
Lug-soil friction angle δ ($^\circ$)	10.4

3.2.3 Experimental Procedure

The experimental procedure was as follows.

- i. Determine the motion parameters (α, l_s, v) from Table 3.1.
- ii. Make the soil uniform and smooth to ensure reproducibility of the experiments.
- iii. Calibrate the force/torque sensor.
- iv. Put the lug at its initial state.
- v. Start the motors and run the data acquisition program.
- vi. Stop the motors and record the experimental data.
- vii. Repeat the above steps to finish all experiments.

3.2.4 Data Processing

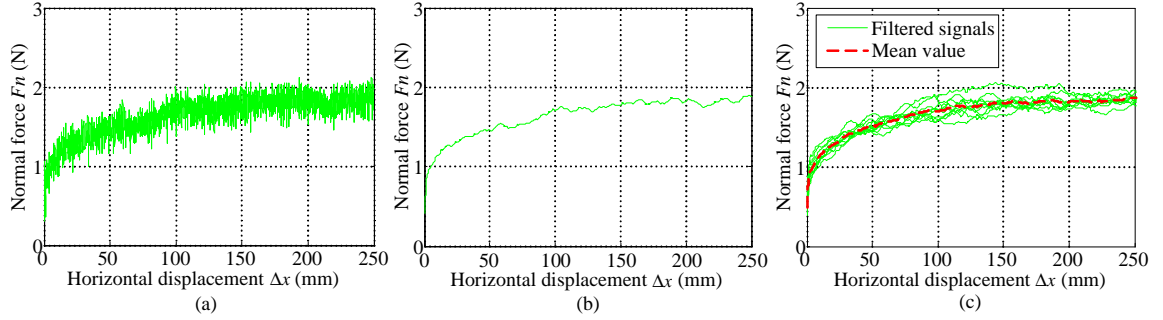


Figure 3.4. Removal of noise from measured forces: (a) original signal measured in one experiment trail, (b) filtered signal, and (c) filtered signals from ten experiment trail and their mean value.

Vibrations in the testbed were manifested as high-frequency noise in the data. The dominant natural frequency of the testbed, which was evaluated from impact tests on the structure, was 16 Hz. Noise at this frequency and high-frequency white noise appeared in the interaction force measurements of all experiments. The noise was removed from the desired force signals by the discrete wavelet transform (DWT) method because the wavelet transform can reflect both whole and local properties of signals owing to its multi-resolution characterization. The force signal was extracted from the original noisy signal using the Daubechies-5 (db5) wavelet at level 5; noise with frequencies exceeding 4.2 Hz was removed from sensor signals corresponding to the sampling rate (200 Hz) in the test system. An example ($\alpha = 90^\circ$, $l_s = 20$ mm and $v = 10$ mm/s) was taken to show the processing procedure from raw data to final result. The force signal selected from the force sensor is shown in Fig. 3.4 (a). After the discrete wavelet transform was applied, the high-frequency noise was removed from the raw data, and the filtered data were relatively smooth (Fig. 3.4 (b)). To ensure repeatability of the experiments, each experiment was repeated ten times and results are presented as their mean value. Based on comparisons between the filtered data and their mean value (Fig. 3.4 (c)), we confirmed that the experiments have acceptable repeatability.

3.3 Experimental Results

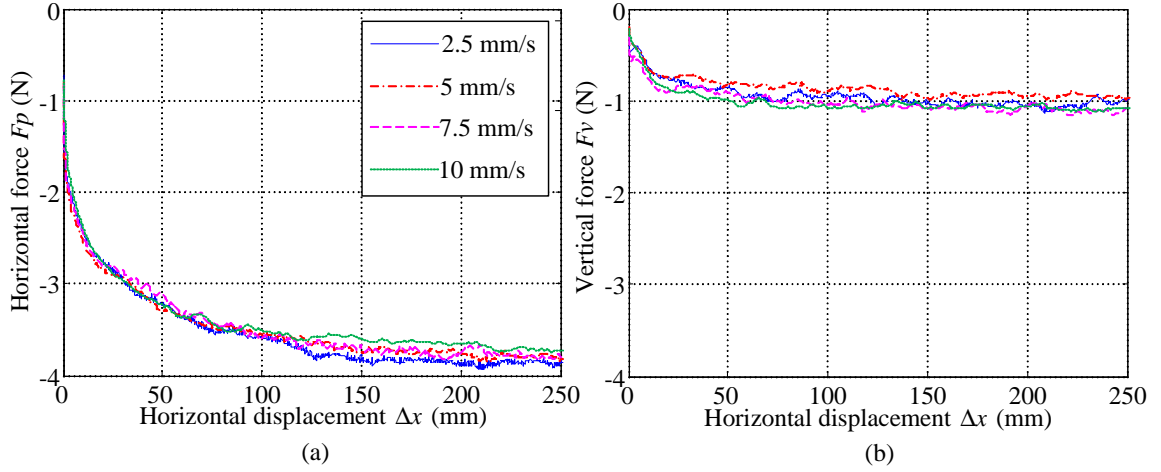


Figure 3.5. (a) Horizontal forces and (b) vertical forces in bulldozing experiments I at inclination angle $\alpha = 90^\circ$ and sinkage length $l_s = 30$ mm for selected horizontal speeds.

The experimental results from bulldozing experiment I are shown in Fig. 3.5, Fig. 3.6, and Fig. 3.7. The results of pre- and post-soil-removal operations in bulldozing experiment II are compared in Fig. 3.8. In these experiments, the sign of forces obeys definition of the coordinate system in Fig. 3.1: while negative horizontal force represents a resistance against lug motion, negative vertical force directs back to ground. The experimental results are summarized as follows.

- i. Speed dependency: the lug with 30 mm sinkage length and 90° inclination angle was horizontally driven to pass over a distance of 250 mm at speeds of 2.5 mm/s, 5 mm/s, 7.5 mm/s, and 10 mm/s, respectively. The relationships between measured forces and horizontal displacements are shown in Fig. 3.5. It can be seen that the values of both horizontal force and vertical force are independent of the bulldozing speed. Therefore, the effect of translational speed can be ignored within the quasi-static regime, and thus speed was set to be 10 mm/s in all following experiments..
- ii. Horizontal displacement dependency: the results from bulldozing experiments I are plotted in Fig. 3.6. The trend in both horizontal force and vertical force can be divided into a transient and a steady state. At $\alpha = 90^\circ$ (Fig. 3.6 (a)) and 105° (Fig.

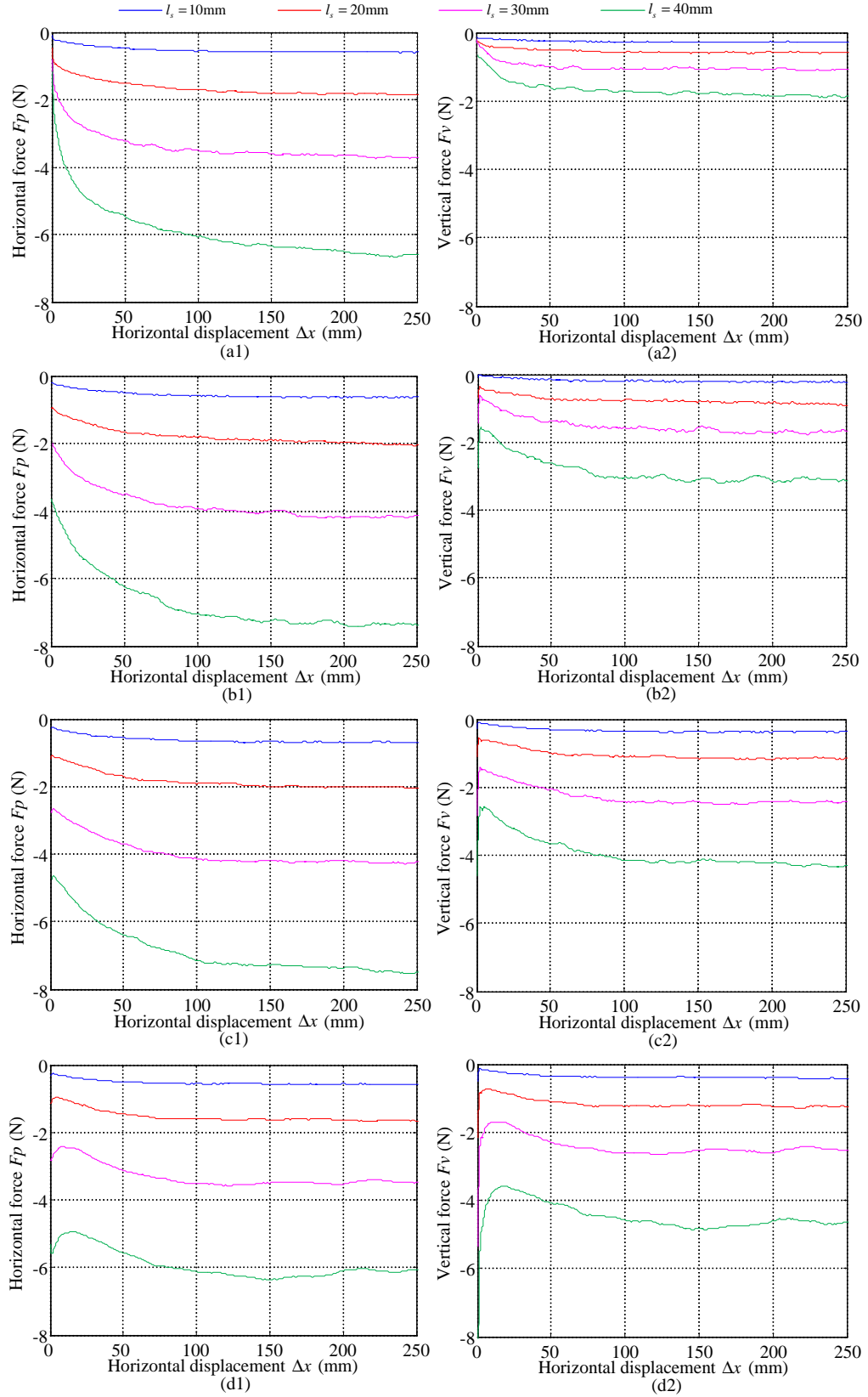


Figure 3.6. Horizontal forces (left panels) and vertical forces (right panels) in bulldozing experiment I ($v = 10$ mm/s) at inclination angles α of (a) 90° , (b) 105° , (c) 120° , and (d) 135° .

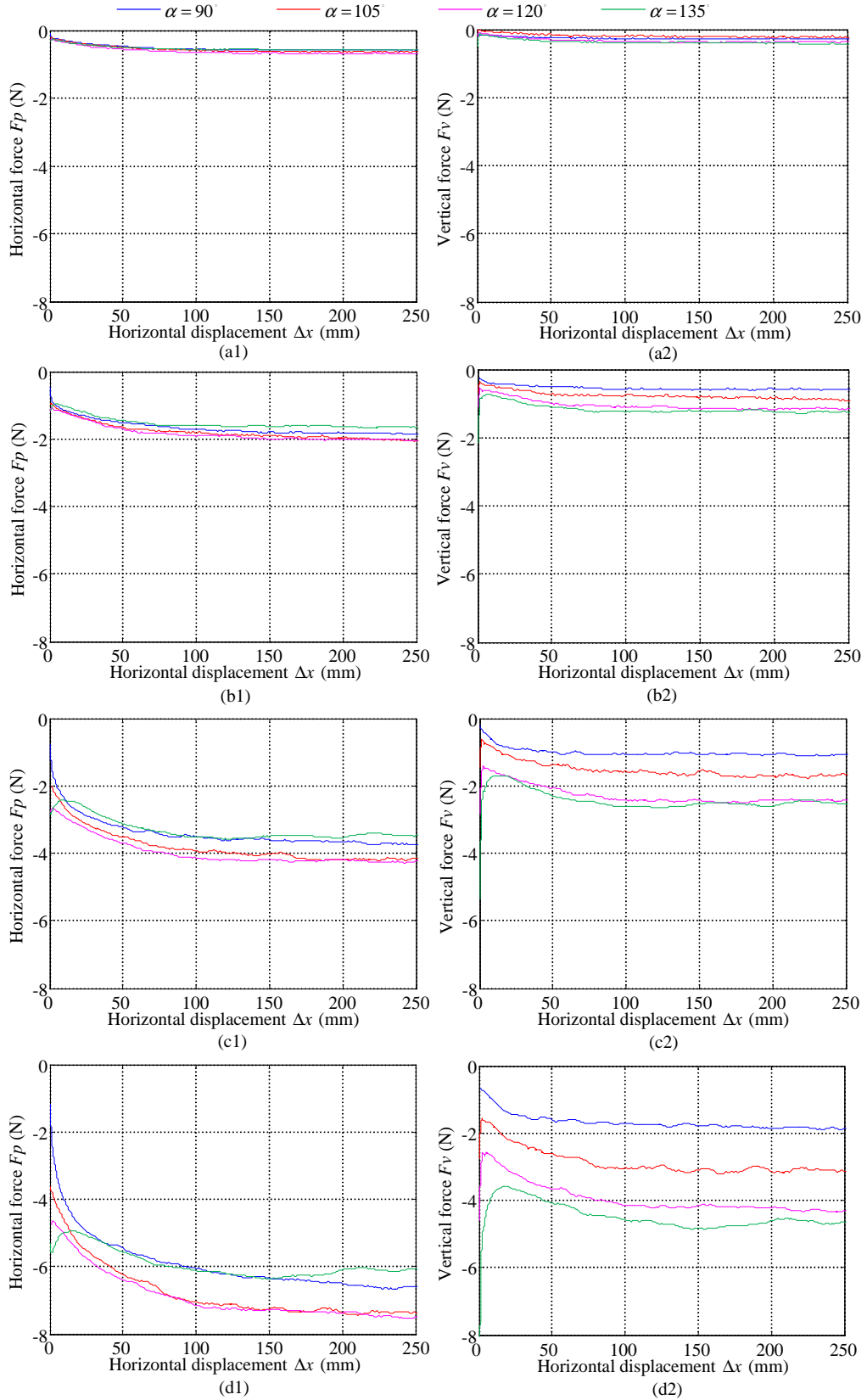


Figure 3.7. Horizontal forces (left panels) and vertical forces (right panels) in bulldozing experiment I ($v = 10$ mm/s) at sinkage lengths l_s of (a) 10 mm, (b) 20 mm, (c) 30 mm, and (d) 40 mm.

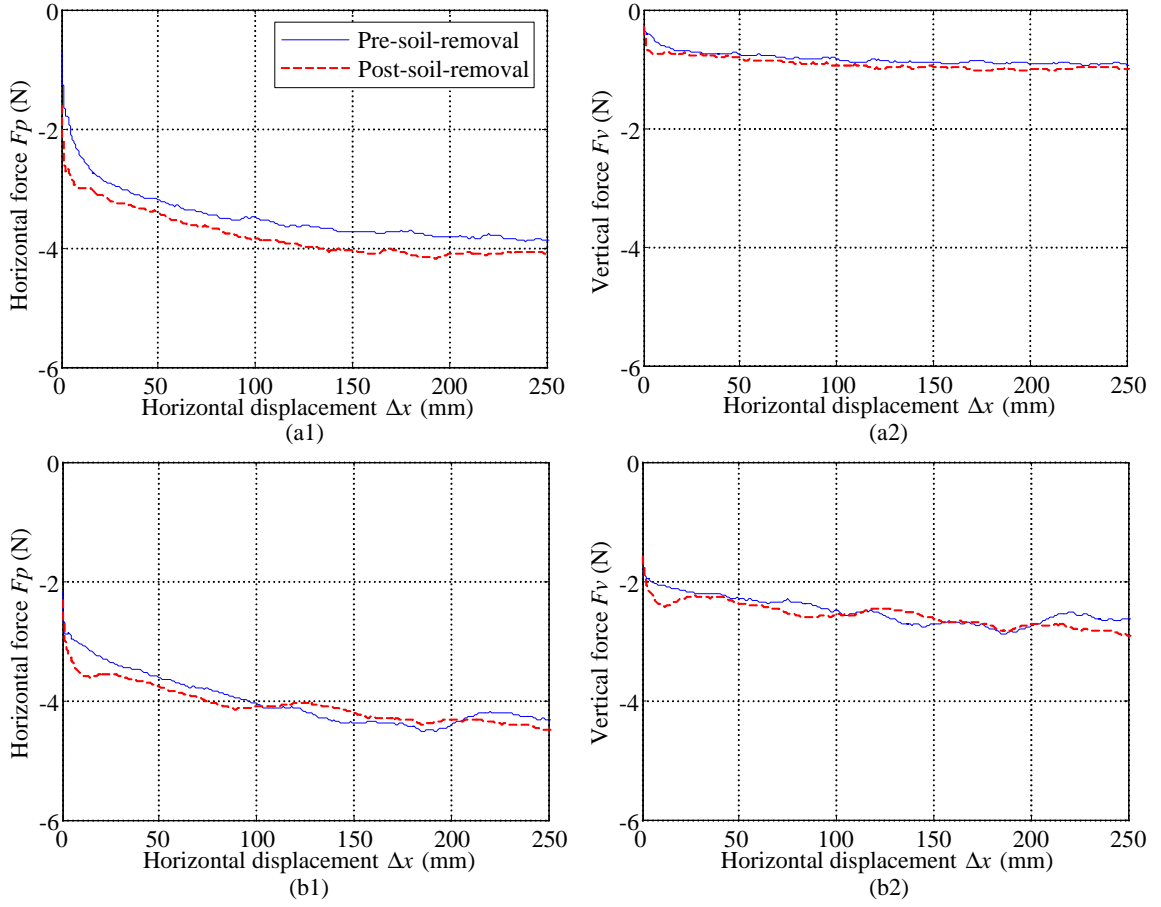


Figure 3.8. Comparison of horizontal forces (left panels) and vertical forces (right panels) measured before and after soil removal in bulldozing experiment II ($l_s = 30$ mm, $v = 10$ mm/s) at inclination angles α of (a) 90° and (b) 120° .

3.6 (b)), the soil reaction forces continuously increased through the transient state. However, at $\alpha = 120^\circ$ (Fig. 3.6 (c)) and 135° (Fig. 3.6 (d)), slight decreases in the forces occurred when the motion first started.

- iii. Sinkage length dependency: the horizontal forces and vertical forces measured at sinkage lengths of 10 mm, 20 mm, 30 mm, and 40 mm are plotted in Fig. 3.6. It can be seen that the lug with larger sinkage length can generate larger soil reaction forces, and the force in steady state increased faster as adopting larger lug sinkage length.
- iv. Inclination angle dependency: as shown in Fig. 3.7, the effect of lug inclination angle gradually became obvious at larger lug sinkage length. Except the starting movement, the horizontal force can achieve the maximum value at $\alpha = 120^\circ$, while the vertical force increased with the increase of lug inclination angle as $l_s = 20, 30$ and 40 mm.
- v. Effect of soil removal operation: as shown in Fig. 3.8, we confirmed that the lug forces measured in pre- and post-soil-removal are substantially similar.

3.4 Discussions

3.4.1 Effect of Horizontal Displacement

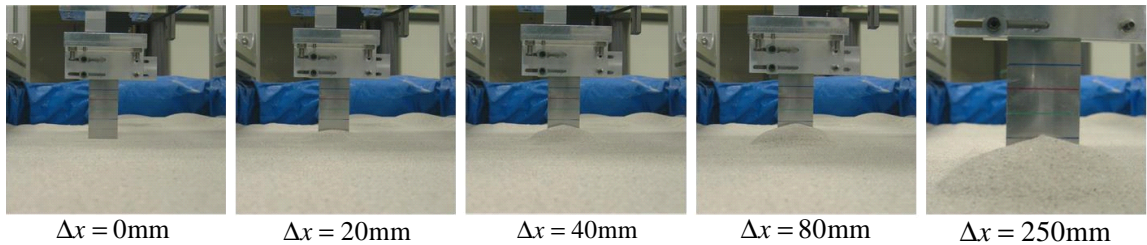


Figure 3.9. The phenomenon of ground swell in bulldozing experiment I ($\alpha = 90^\circ$, $l_s = 30$ mm, $v = 10$ mm/s).

The trend of the forces measured from bulldozing experiment I (Fig. 3.6) corresponded to the volume change of ground swell observed in experiments. As shown in Fig. 3.9, owing to the action of the lug, the ground gradually swelled, and then, the swelled volume achieved

a dynamically balanced condition. The results of bulldozing experiment II can help us to identify how the ground swell contribute to the increasing lug forces in the transient state, in which an additional process of removing swelled soil was involved. As shown in Fig. 3.8, the forces measured in pre- and post-soil removal operations are substantially similar. The difference between these two forces can be estimated by λ_p in (3.4) and λ_v in (3.5), respectively.

$$\lambda_p = \frac{F_p^R - F_p^O}{F_p^O} \quad (3.4)$$

$$\lambda_v = \frac{F_v^R - F_v^O}{F_v^O} \quad (3.5)$$

where F_p and F_v are the horizontal force and vertical force. The superscript O and R represent the force measured before and after soil removal, respectively.

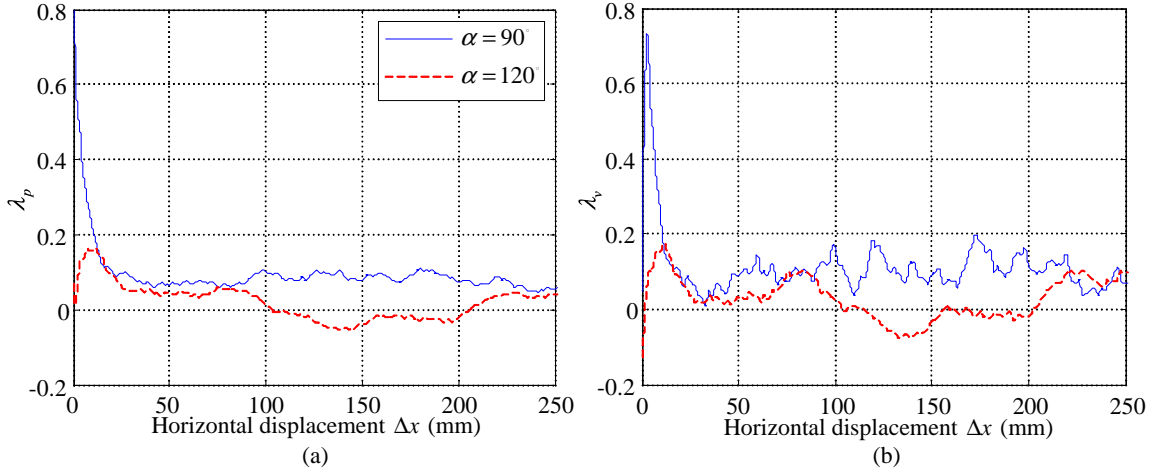


Figure 3.10. (a) λ_p in (3.4) and (b) λ_v in (3.5) from bulldozing experiment II at $\alpha = 90^\circ$, $l_s = 30$ mm, $v = 10$ mm/s, and at $\alpha = 120^\circ$, $l_s = 30$ mm, $v = 10$ mm/s.

As shown in Fig. 3.10, small λ_p and λ_v indicate that ground swell contributes more than other factors (e.g. soil compression, soil plasticity, sand dilatation, etc.) to the increasing lug forces in the transient state.

Based on lug-soil interaction characteristics plotted in Fig. 3.6, an exponential function

was chosen to approximate the relationship between horizontal displacement Δx and forces F_p , F_v by using least square method.

$$F_p = F_{p0} + A_p e^{-B_p \cdot \Delta x} \quad (3.6)$$

$$F_v = F_{v0} + A_v e^{-B_v \cdot \Delta x} \quad (3.7)$$

where F_{p0} and F_{v0} are the value of the normal force and vertical force at steady state, A_p (or A_v) is the difference between the initial ($\Delta x = 0$) and steady values ($\Delta x = \infty$), and $1/B_p$ (or $1/B_v$) is a displacement constant that denotes the traveling distance of the lug until arriving at steady state. We fit our measured data to the form in (3.6) and (3.7). For $\alpha = 120^\circ$ and 135° , the data in descent stage were removed in advance and the remaining data were used in the curve-fitting operation. The fitted curves (dashed lines) are compared with experimental results (solid lines) in Fig. 3.11 and parameters determined for each configuration are summarized in Table 3.3.

Table 3.3. Values for parameters in (3.6) and (3.7) determined from bulldozing experiment I.

α [°]	l_s [mm]	Horizontal force			Vertical force		
		F_{p0} [N]	A_p [N]	B_p [1/mm]	F_{v0} [N]	A_v [N]	B_v [1/mm]
90	10	-0.5834	0.3862	0.0267	-0.2765	0.1294	0.0278
	20	-1.8245	0.9067	0.0220	-0.5793	0.2702	0.0297
	30	-3.6412	1.9523	0.0336	-1.0563	0.7654	0.0640
	40	-6.5229	3.4441	0.0239	-1.7990	1.0984	0.0371
105	10	-0.6338	0.4116	0.0231	-0.2212	0.1983	0.0238
	20	-2.0101	0.9740	0.0178	-0.8577	0.4185	0.0175
	30	-4.1702	1.9628	0.0220	-1.6887	0.9565	0.0232
	40	-7.4041	3.4779	0.0219	-3.1469	1.5826	0.0228
120	10	-0.6883	0.4292	0.0241	-0.3747	0.2794	0.0272
	20	-2.0170	1.0130	0.0226	-1.1441	0.6688	0.0270
	30	-4.2534	1.7676	0.0244	-2.4553	1.1997	0.0257
	40	-7.4930	2.9193	0.0193	-4.2968	1.8965	0.0216
135	10	-0.5763	0.3047	0.0282	-0.4140	0.2032	0.0200
	20	-1.6338	0.9664	0.0346	-1.2366	0.8595	0.0393
	30	-3.5087	1.6722	0.0303	-2.5530	1.4150	0.0341
	40	-6.1905	2.6235	0.0311	-4.7195	2.1244	0.0254

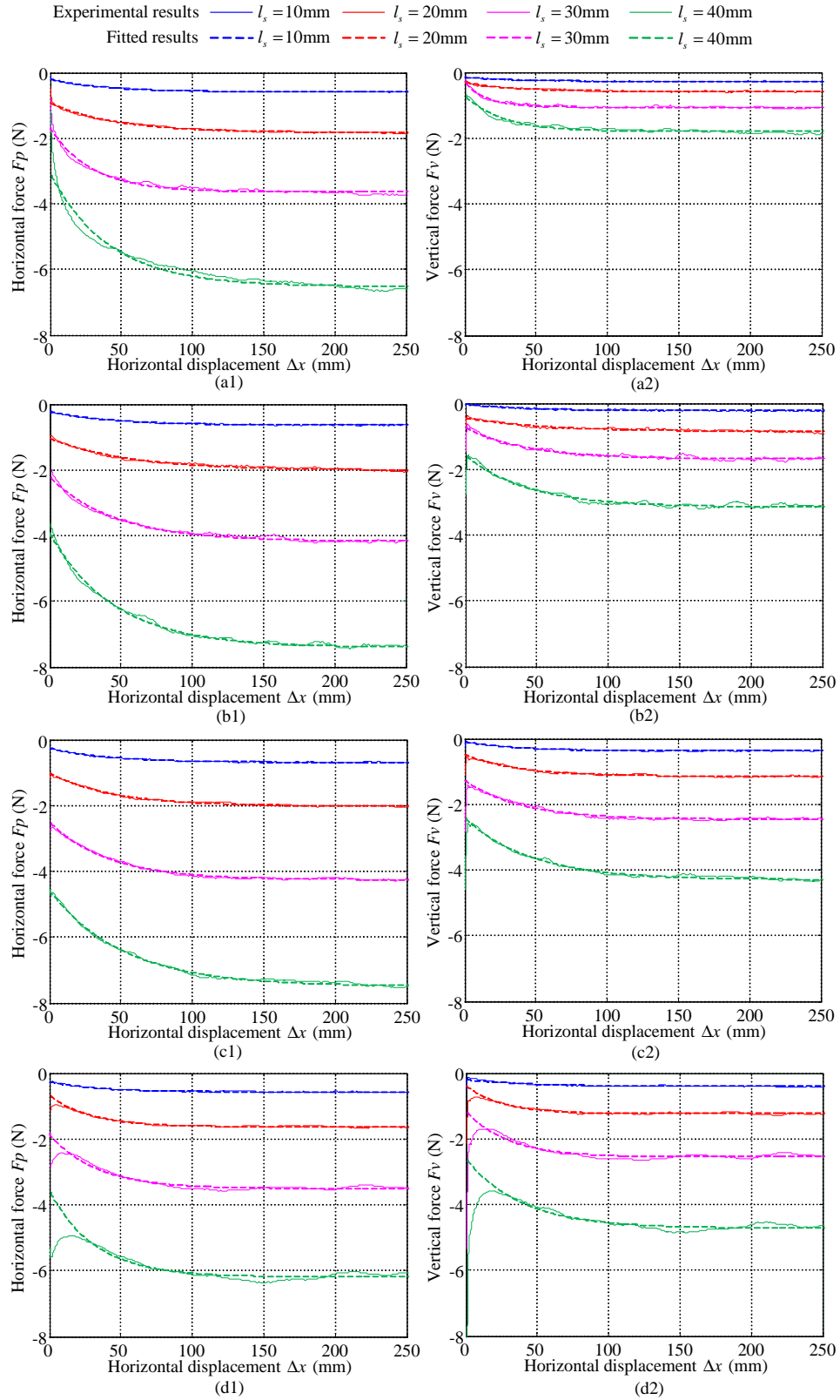


Figure 3.11. Comparison of experimental results and fitted results of horizontal forces (left panels) and vertical forces (right panels) in bulldozing experiment I ($v = 10 \text{ mm/s}$) at inclination angles α of (a) 90° , (b) 105° , (c) 120° , and (d) 135° .

3.4.2 Effect of Lug Sinkage Length

On the basis of the fitted results in Table 3.3, the effects of lug sinkage length were determined by comparing the horizontal (or vertical) force generated at different sinkage lengths. Ishigami et al. have verified that, at steady state, resistance to bulldozing obeys a quadratic function of lug sinkage [81]. In this study, we further consider the effects of lug sinkage on horizontal (or vertical) force within a complete lug-soil interaction process. According to (3.6) (or (3.7)), F_{p0} (or F_{v0}) determines characteristics of steady state, while A_p (or A_v) and B_p (or B_v) affect characteristics of transient state. The following quadratic functions were used to approximate the relationships between l_s and F_{p0} (or F_{v0}) and between l_s and A_p (or A_v) at fixed inclination angle.

$$F_{p0} = K_1^{F_{p0}} l_s^2 + K_2^{F_{p0}} l_s + K_3^{F_{p0}} \quad (3.8)$$

$$A_p = K_1^{A_p} l_s^2 + K_2^{A_p} l_s + K_3^{A_p} \quad (3.9)$$

$$F_{v0} = K_1^{F_{v0}} l_s^2 + K_2^{F_{v0}} l_s + K_3^{F_{v0}} \quad (3.10)$$

$$A_v = K_1^{A_v} l_s^2 + K_2^{A_v} l_s + K_3^{A_v} \quad (3.11)$$

Values for the fitted coefficients in (3.8) and (3.9), (3.10) and (3.11) are summarized in Table 3.4, and Table 3.5, respectively. Predictions for F_{p0} from (3.8) and F_{v0} from (3.10), A_p from (3.9) and A_v from (3.11) are compared with experimental results in Figs. 3.12 and 3.13, respectively. Both F_{p0} (or F_{v0}) and A_p (or A_v) satisfy the quadratic functions of lug sinkage for all inclination angles. In all bulldozing experiments, values of the parameter B_p (or B_v) in (3.6) (or (3.7)) were mainly around 0.02.

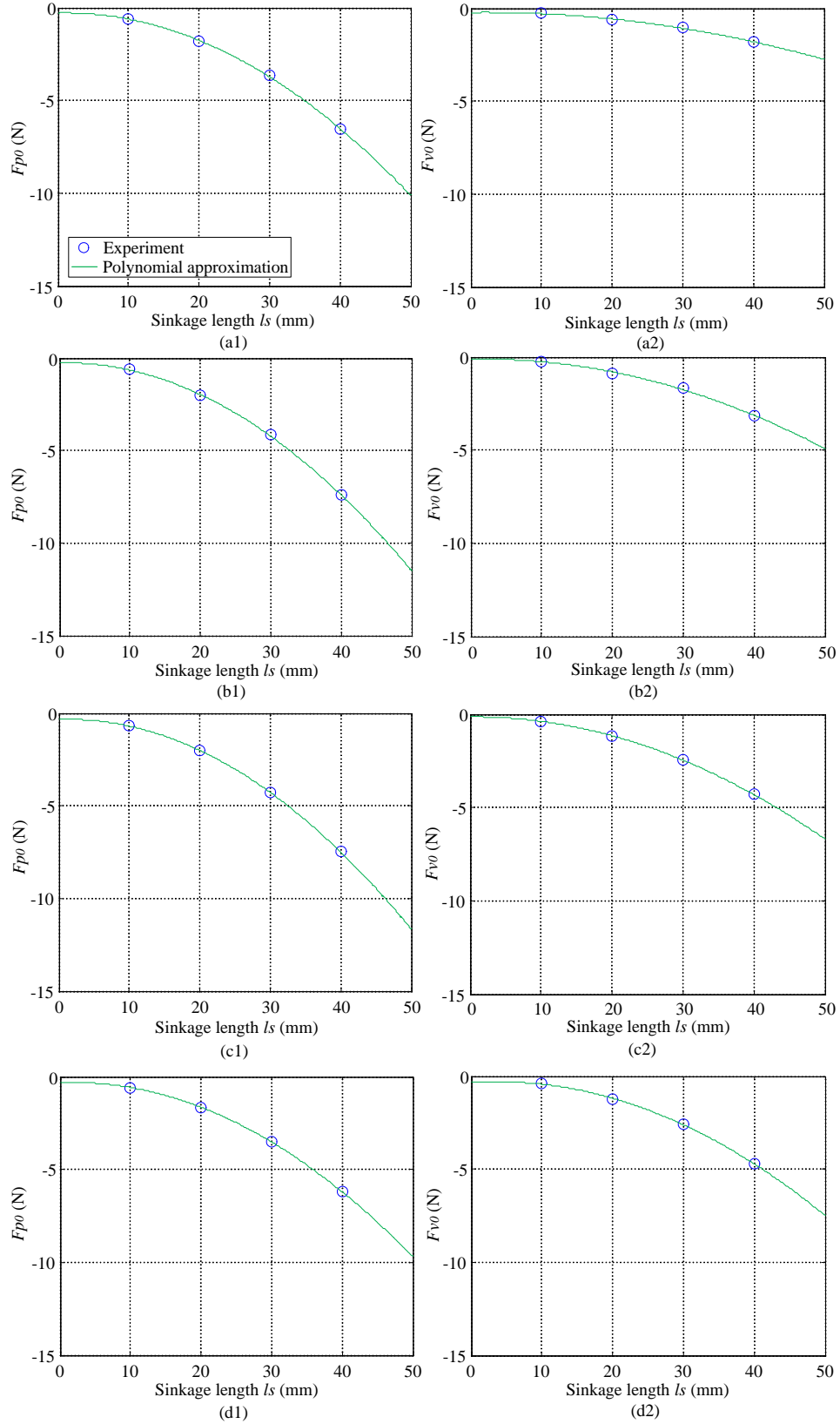


Figure 3.12. F_{p0} in (3.8) (left panels) and F_{v0} in (3.10) (right panels) for bulldozing experiment I at inclination angles α of (a) 90° , (b) 105° , (c) 120° , and (d) 135° .

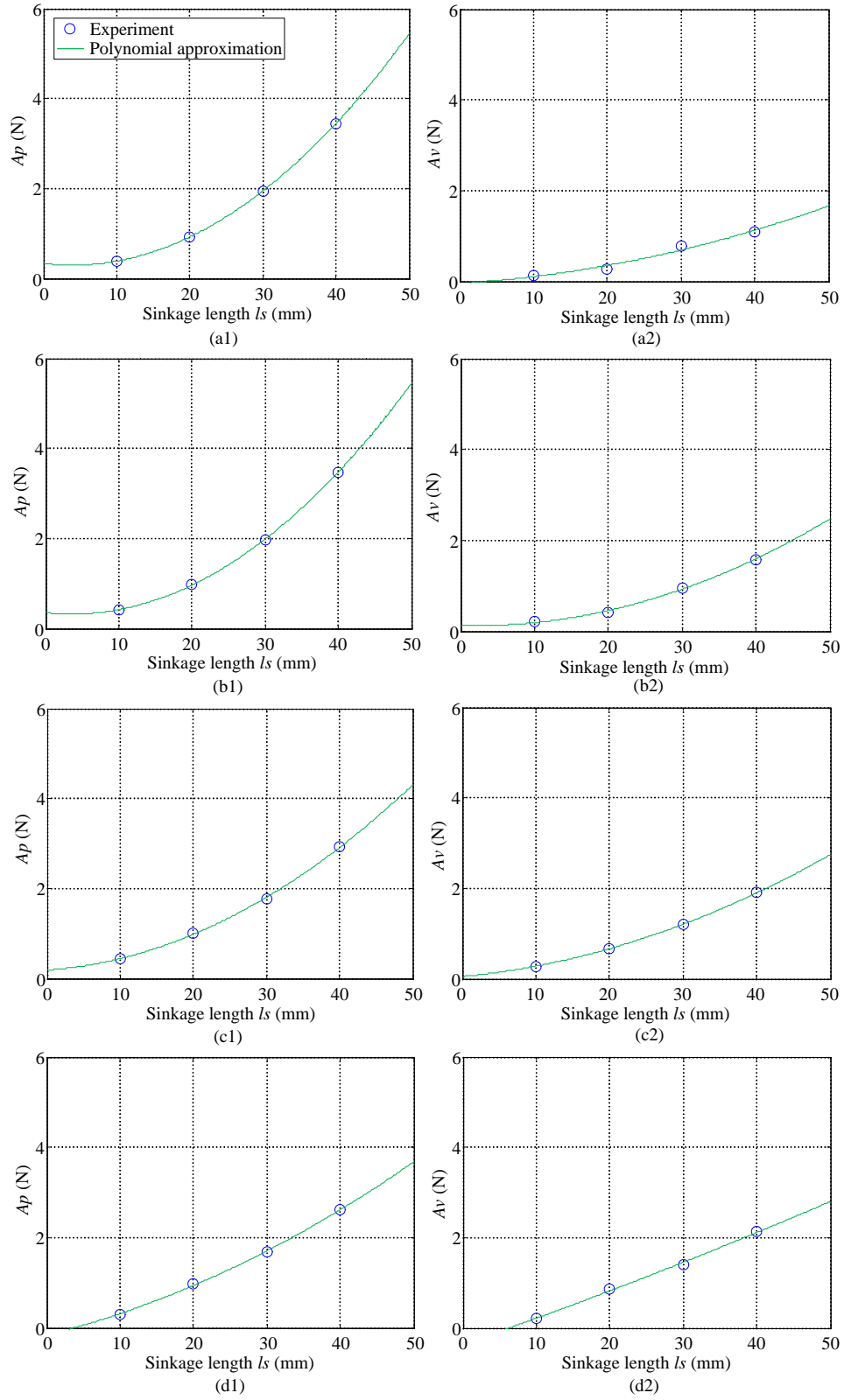


Figure 3.13. A_p in (3.9) (left panels) and A_v in (3.11) (right panels) for bulldozing experiment I at inclination angles α of (a) 90°, (b) 105°, (c) 120°, and (d) 135°.

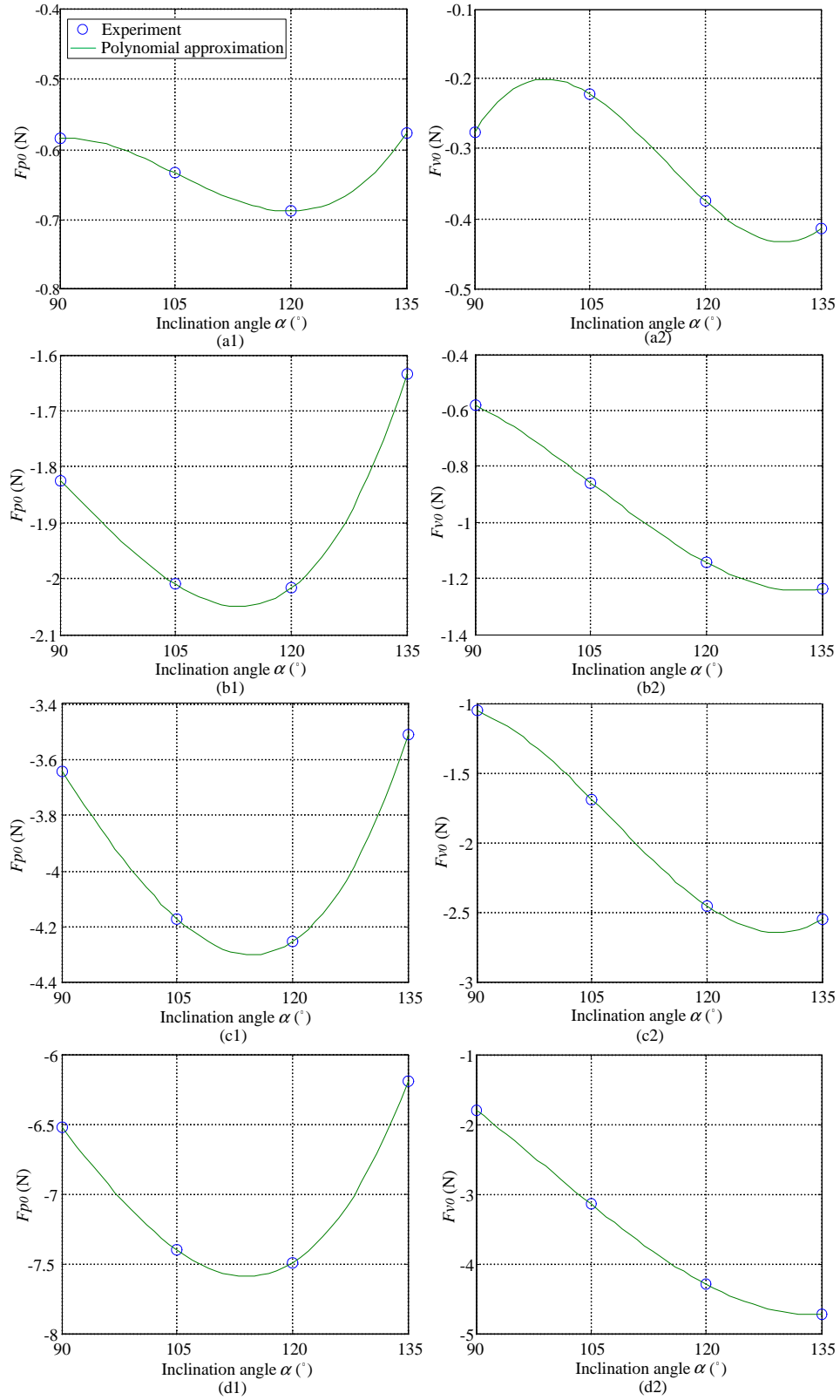


Figure 3.14. F_{p0} in (3.12) (left panels) and F_{v0} in (3.13) (right panels) for bulldozing experiment I at sinkage lengths l_s of (a) 10 mm, (b) 20 mm, (c) 30 mm, and (d) 40 mm.

Table 3.4. Values for coefficients in (3.8) and (3.9) determined from bulldozing experiment I.

α [$^\circ$]	$K_1^{F_{p0}}$	$K_2^{F_{p0}}$	$K_3^{F_{p0}}$	$K_1^{A_p}$	$K_2^{A_p}$	$K_3^{A_p}$
90	-0.0041	0.0087	-0.2850	0.0024	-0.0192	0.3316
105	-0.0046	0.0075	-0.2588	0.0024	-0.0172	0.3505
120	-0.0048	0.0124	-0.3389	0.0014	0.0113	0.1859
135	-0.0041	0.0159	-0.3283	0.0007	0.0404	-0.1618

Table 3.5. Values for coefficients in (3.10) and (3.11) determined from bulldozing experiment I.

α [$^\circ$]	$K_1^{F_{v0}}$	$K_2^{F_{v0}}$	$K_3^{F_{v0}}$	$K_1^{A_v}$	$K_2^{A_v}$	$K_3^{A_v}$
90	-0.0011	0.0045	-0.2165	0.0005	0.0100	-0.0444
105	-0.0021	0.0066	-0.1037	0.0010	-0.0038	0.1236
120	-0.0027	0.0032	-0.1385	0.0008	0.0154	0.0498
135	-0.0034	0.0257	-0.3524	0.0001	0.0566	-0.3629

3.4.3 Effect of Lug Inclination Angle

Similar with the analysis in Sec. 3.4.2, the effects of lug inclination angle were determined by comparing F_{p0} (or F_{v0}) in Table 3.3 generated at different inclination angles. As shown in Fig. 3.14, we found that the lug-soil reaction force achieved its peak value with a specific inclination angle of the lug. Based on this observation, the cubic linear functions in (3.12) and in (3.13) were adopted to find the optimal values of the inclination angle. The fitted results are summarized in Tables 3.6 and 3.7.

$$F_{p0} = D_1^{F_{p0}} \alpha^3 + D_2^{F_{p0}} \alpha^2 + D_3^{F_{p0}} \alpha + D_4^{F_{p0}} \quad (3.12)$$

$$F_{v0} = D_1^{F_{v0}} \alpha^3 + D_2^{F_{v0}} \alpha^2 + D_3^{F_{v0}} \alpha + D_4^{F_{v0}} \quad (3.13)$$

Predictions for F_{p0} and F_{v0} from (3.12) and (3.13) are compared with experimental results in Fig. 3.14. We confirmed that F_{p0} and F_{v0} achieved their maximum values as inclination angle of lug was set at the range of $[110^\circ, 120^\circ]$, and at the range of $[125^\circ, 135^\circ]$, respectively. It means that the lug can be set at an optimal angle to improve the

Table 3.6. Values for coefficients in (3.12) determined from bulldozing experiment I.

l_s [mm]	$D_1^{F_{p0}}$	$D_2^{F_{p0}}$	$D_3^{F_{p0}}$	$D_4^{F_{p0}}$
10	8.4247×10^{-6}	-0.0027	0.2752	-9.9207
20	1.0440×10^{-5}	-0.0029	0.2531	-8.7966
30	1.8869×10^{-5}	-0.0050	0.3914	-12.5030
40	2.9585×10^{-5}	-0.0076	0.5698	-18.1470

Table 3.7. Values for coefficients in (3.13) determined from bulldozing experiment I.

l_s [mm]	$D_1^{F_{v0}}$	$D_2^{F_{v0}}$	$D_3^{F_{v0}}$	$D_4^{F_{v0}}$
10	1.5951×10^{-5}	-0.0055	0.6181	-23.0811
20	9.9704×10^{-6}	-0.0032	0.3124	-10.3833
30	3.9659×10^{-5}	-0.0128	1.3188	-45.0537
40	2.6133×10^{-5}	-0.0078	0.6828	-19.1888

horizontal force or vertical force according to requirement. We deduce that the movement of the lug with a larger projection of the lug on the horizontal plane, which increases with the inclination angle, can cause soil failure over a wider range. This significantly increases the local density of the sand and enlarges lug-soil interaction force (Fig. 3.15). On the other hand, we observed from the experiments that the volume of ground swell decreased with the increase of lug inclination angle, and thus this will reduce lug-soil interaction forces. Therefore, the peak value of lug force can be achieved at a certain inclination angle. However, we have not yet quantitatively measure the volume of ground swell and change of pressure within the soil to verify our deduction, but we intend to revisit this issue in our later work.

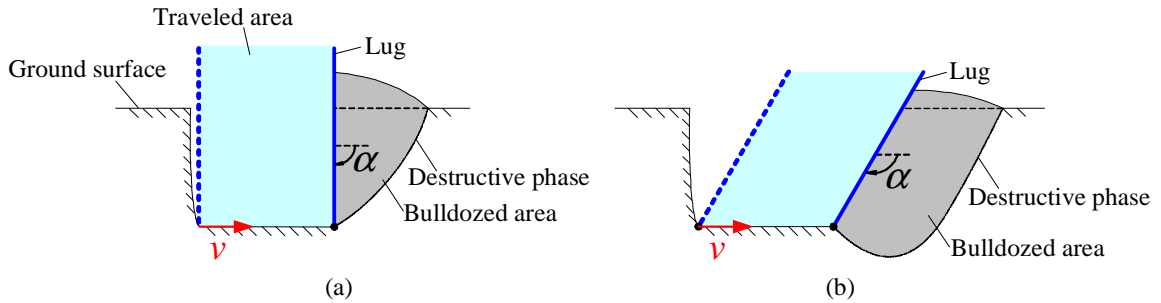


Figure 3.15. Soil failure in bulldozing experiment at α of (a) 90° and (b) 120° .

Moreover, the ratio of horizontal force to vertical force defined in (3.14) was calculated to investigate the effects of lug inclination angle further.

$$\eta = \left| \frac{F_p}{F_v} \right| \quad (3.14)$$

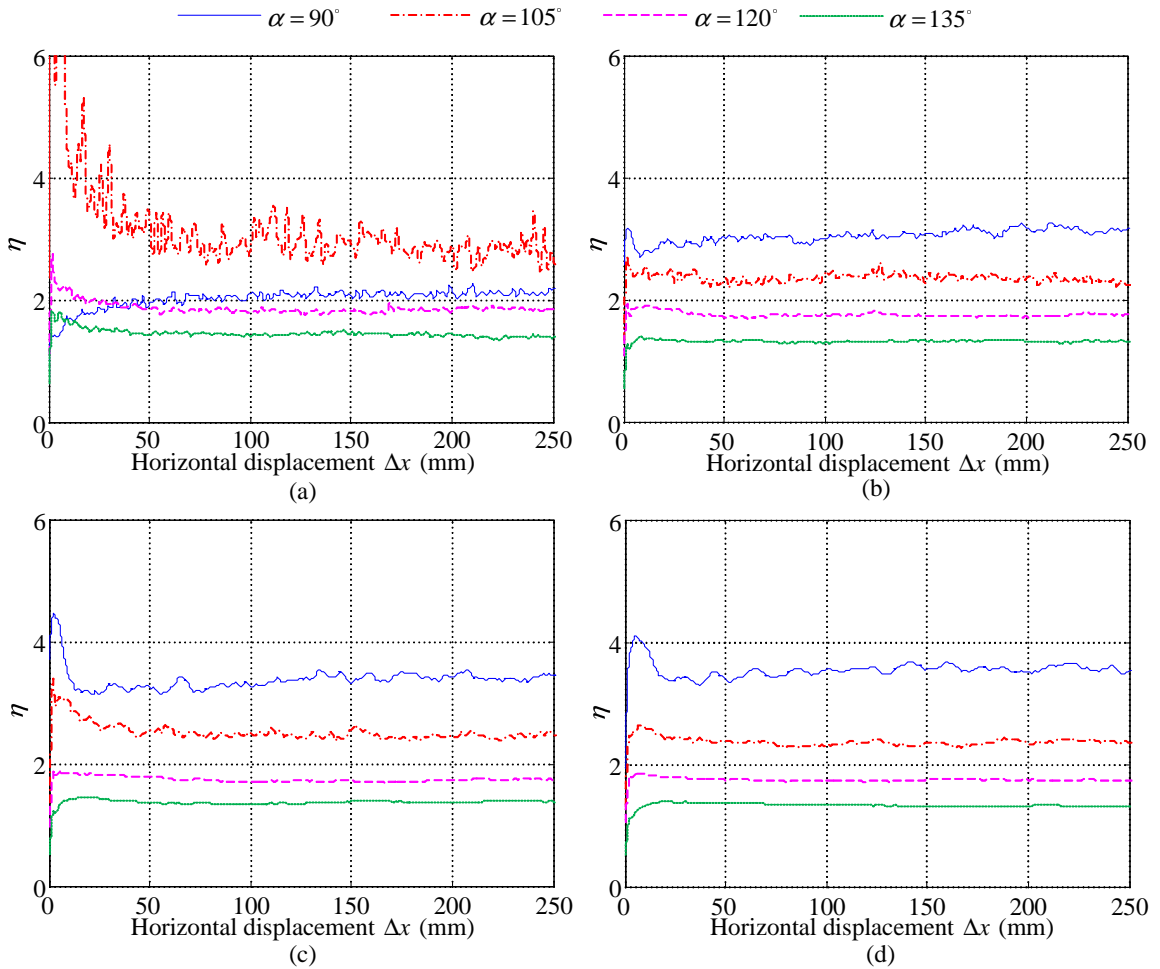


Figure 3.16. Ratio of horizontal force to vertical force at selected inclination angles α and sinkage lengths l_s of (a) 10 mm, (b) 20 mm, (c) 30 mm, (d) 40 mm.

As shown in Fig. 3.16, ratio η decreased with the increase of the lug inclination angle, except the results from adopting lug sinkage length of 10 mm. On the whole, the lug inclination angle can be tuned to adjust the distribution of lug-soil interaction force in horizontal direction and vertical direction.

3.5 Summary

In this chapter, we have performed an experimental study to determine the effects of lug motion on lug forces by using a single lug on sandy terrain. Numerical fits of the measured data were conducted by using least square method to quantitatively analyze the effects. We confirmed that:

- i. Lug-soil interaction forces are independent of traveling speed when the speed is below 10 mm/s.
- ii. The relationship between soil reaction forces and horizontal displacement can be approximated by an exponential function. The change of force in transient state is mainly contributed from ground swell.
- iii. The horizontal force (or vertical force) is a quadratic function of lug sinkage in both transient and steady state.
- iv. At the fixed lug sinkage length, the lug-soil interaction force can achieve the maximum value by setting lug at an optimal inclination angle. Moreover, the lug inclination angle affects the ratio of horizontal force to vertical force.

From the experimental analysis in this chapter, it is obvious that the lug-soil interaction forces depend on the lug trajectory significantly. Therefore, it is possible to improve the ALW-soil interaction force by tuning lug trajectory.

Chapter 4

ALW-soil Interaction

Characteristics

On soft terrains, smooth wheels easily sink or slip, and the normal legs may fail to provide sufficient supporting force. Through integrating motion of the wheel and the lugs, the proposed ALW module can overcome these problems. While the wheel rim provides larger contacting area with the soil to prevent the wheel sinkage, the lugs are actively protruded outward the wheel and inserted into the soil to gain additional drawbar pull and vertical force.

In Chapter 3, it has been found that the lug motion significantly affects the lug-soil interaction forces. Therefore, by tuning the lug trajectory, the ALW can potentially improve the traveling performance. To realize this potential, we must determine the relationship between the lug motion and ALW-soil interaction forces. Although the results from single lug experiments are important for evaluating the traveling performance of ALW mechanism, they cannot be used to predict the lugged wheel-soil interaction forces until the interplay between the lug and wheel has been clearly understood. The wheel exerts an additional surcharge on the ground that enlarges the lug-soil interaction forces. The wheel surface-soil interaction forces are also altered because the lug excavates some of the soil, thereby altering the soil conditions beneath the wheel rim. Such complicated soil deformations are difficult

to accommodate in a theoretical model of lugged wheel-soil interaction forces. Therefore, an experimental study and analysis are conducted in this chapter.

Before investigating the performance of the actual ALW, it is essential to observe and evaluate the ALW-soil interaction characteristics of a wheel with a single active lug, without interference from other lugs. For this purpose, we analyze the effects of lug inclination angle and lug sinkage length by measuring the interaction forces on the single-lugged ALW at various lug trajectories.

4.1 ALW-soil Interaction Process

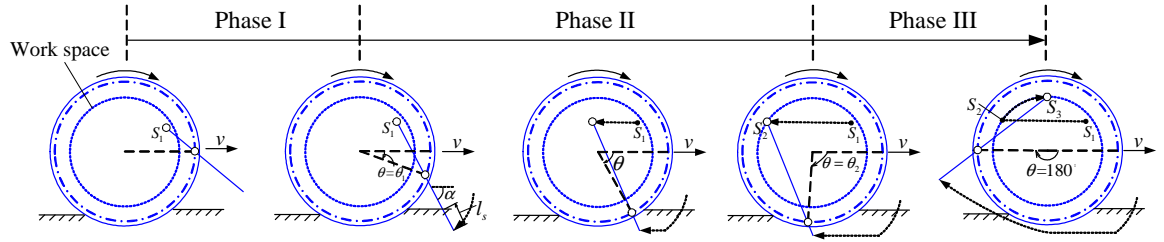


Figure 4.1. Lug trajectory within a complete lug-soil interaction process as the wheel rotates from 0° to 180°.

In this chapter, we measure the characteristics of ALW-soil interaction forces as the wheel rotates from 0° to 180°. As shown in Fig. 4.1, corresponding to rotation of the wheel, the lug-soil interaction process passes through three phases. In phase I, the lug contacts and penetrates the soil. At the switch point where $\theta = \theta_1$, the lug enters the initial state of phase II. As the wheel rotates through θ_1 to θ_2 in phase II, the traveling performance is enhanced by driving the lug shaft along a desired trajectory S_1S_2 . Finally, the lug is retracted from the soil during phase III. Given the required motion parameters, switch point θ_1 , inclination angle α (in phase II), sinkage length l_s (in phase II), the desired joint angles can be calculated by inverse kinematics model presented in Sec. 2.2.2. As an example ($\theta_1 = 20^\circ$, $\alpha = 60^\circ$ (in phase II), $l_s = 18$ mm (in phase II)), Fig. 4.2 shows the joint angles, inclination angle, sinkage length, and velocity of the lug tip within a completed lug-soil interaction process.

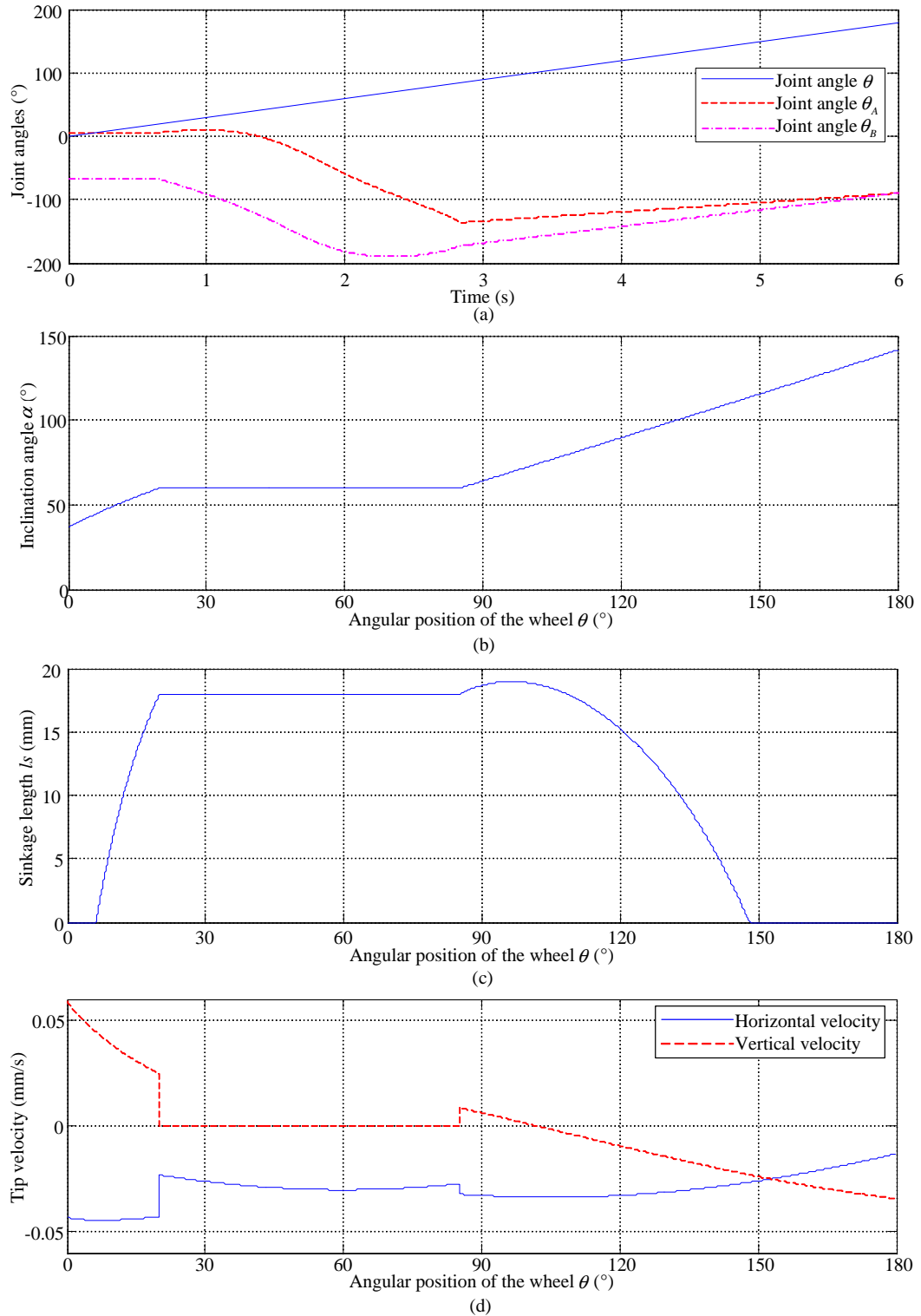


Figure 4.2. Locomotion of the ALW at initial rotational angle $\theta_1 = 20^\circ$, inclination angle $\alpha = 60^\circ$ (in phase II), sinkage length $l_s = 18$ mm (in phase II) and wheel sinkage $h = 5$ mm. (a) Joint angles calculated from (2.8), (b) lug inclination angle, (c) lug sinkage length, (d) velocity of the lug tip.

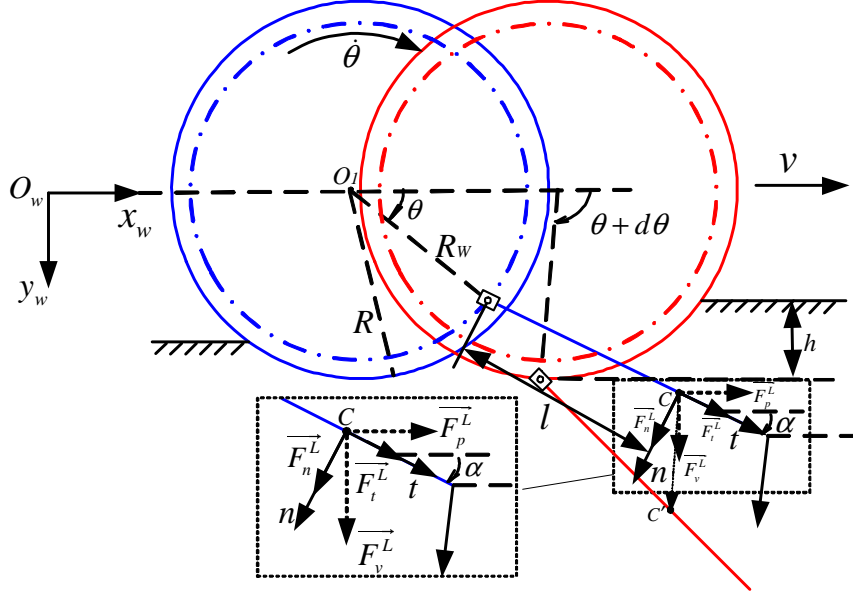


Figure 4.3. Illustration of a single increment of lug displacement.

To analyze the soil-lug forces, the trajectory of points on the lug should be considered. Generally, slips occur when a vehicle travels on loose soil; it is expressed by the slip ratio s , that is defined as a function of the horizontal velocity of the wheel v , wheel radius R , and angular speed of the wheel $\dot{\theta}$ as,

$$s = \frac{R\dot{\theta} - v}{R\dot{\theta}} \quad (4.1)$$

The world coordinate system is shown in Fig. 4.3. It is assumed that the x -coordinate of the wheel center is 0 when $\theta = 0$ and the wheel center moves along the x -axis with constant sinkage h and slip ratio s . Given the angular position of the wheel θ and inclination angle of the lug α , the coordinates of point C on the lug can be calculated as follows.

$$\begin{aligned} x &= R\theta(1 - s) + R_H \cos \theta + l \cos \alpha \\ y &= R_H \sin \theta + l \sin \alpha \end{aligned} \quad (4.2)$$

As the wheel rotates from θ to $\theta + d\theta$ and the distance changes from l to $l + dl$, the point C on the lug will move from C to C' with infinitesimal displacements, dx and dy .

These can be obtained by differentiating equation (4.2). We can obtain the components of infinitesimal displacement perpendicular to (normal to) and along (tangential to) the lug in local coordinate fixed at the point C , as shown in Fig. 4.3.

$$\begin{bmatrix} dt \\ dn \end{bmatrix} = \begin{bmatrix} \cos \alpha & \sin \alpha \\ -\sin \alpha & \cos \alpha \end{bmatrix} \begin{bmatrix} dx \\ dy \end{bmatrix} \quad (4.3)$$

A positive value of dn means that the lug will push the soil backward to gain the normal force F_n^C , and dt means that the lug will generate the tangential force F_t^C . The normal force F_n^L and tangential force F_t^L acting on the whole lug can be calculated by integrating the forces acting on each infinitesimal. The drawbar pull and vertical force acting on the lug can be subsequently derived as follows:

$$\begin{bmatrix} F_p^L \\ F_v^L \end{bmatrix} = \begin{bmatrix} \cos \alpha & -\sin \alpha \\ \sin \alpha & \cos \alpha \end{bmatrix} \begin{bmatrix} F_t^L \\ F_n^L \end{bmatrix} \quad (4.4)$$

The drawbar pull F_p and vertical force F_v acting on the ALW module are the sum of F_p^L , F_v^L acting on the lug, and F_p^W , F_v^W acting on the wheel rim.

$$\begin{cases} F_p = F_p^L + F_p^W \\ F_v = F_v^L + F_v^W \end{cases} \quad (4.5)$$

Because of the complex soil deformation, the experimental study is adopted rather than theoretical modeling to discuss the following two topics in this chapter.

- i. Effect of lug sinkage length l_s on ALW-soil interaction forces F_p and F_v .
- ii. Effect of lug inclination angle α on ALW-soil interaction forces F_p and F_v .

4.2 Experimental Setup

4.2.1 Experimental Overview and Conditions

To investigate the ALW-soil interaction characteristics, the drawbar pull and vertical force of the wheel outfitted with an active lug were measured with various lug inclination angles and lug sinkage lengths. In all experiments, the wheel rim sinkage was fixed at 5 mm. The wheel rim was rotated from 0° to 180° at a constant angular velocity of $30^\circ/\text{s}$. The traveling velocity was 20 mm/s, yielding a slip ratio (calculated from (4.1)) of 0.3. All combinations of lug motion parameters (in phase II) adopted in the experiments are tabulated in Table 4.1.

Table 4.1. Values of lug motion parameters (in phase II) adopted in the experiments.

Initial rotational angle θ_1 [$^\circ$]	Inclination angle α [$^\circ$]	Sinkage length l_s [mm]
20	50	10, 14, 18, 22
20	60	10, 14, 18, 22
30	70	10, 14, 18, 22

According to the motion parameters (θ_1, α, l_s) determined from Table 4.1, the following lug trajectory is designed to move the lug at a constant inclination angle and sinkage length in phase II as shown in Fig. 4.1.

- i. Because the wheel sinkage, lug inclination angle and lug sinkage length are maintained at constant values, throughout phase II, the lug performs a translational motion. Based on the values of α and l_s , the trajectory of the lug shaft which is a horizontal line inside its workspace can be determined. Then, according to the initial rotation angle θ_1 of the wheel in phase II, the corresponding starting point S_1 is derived from the kinematic model. Destination S_2 of this phase is the point at which the trajectory and the workspace boundary of the lug shaft intercept.
- ii. Before the wheel begins rotating, the lug shaft is positioned at S_1 . In phase I, as the wheel rotates from 0° at constant angular velocity, the lug is forced into the soil by the hinge, and starts to push the soil backward. The α and l_s are continuously

increased to the desired inclination angle and sinkage length in the initial position of phase II, respectively, as the angular position of the wheel increases to θ_1 .

- iii. During phase III, having arrived at S_2 , the lug shaft reverses to S_3 along the arc S_2S_3 at constant speed as the wheel rotates. At a wheel rotation of 180° , the lug shaft precisely stops at S_3 .

Photographs of the actual motional behavior of the ALW are displayed in Fig. 4.4.

4.2.2 ALW-soil Interaction Testbed

ALW-soil interaction measurements were conducted in a testbed (Fig. 4.5) of length 1700 mm, width 500 mm, and height 800 mm. The conveyance unit of the testbed was actuated along two slide guides at the desired speed by using a DC brushed servo motor via a ball-bearing screw. The angular position of the screw was monitored by an incremental encoder (E6A2-CWZ3E, OMRON; Japan). The wheel module was connected to the conveyance unit by a six-axis force/torque sensor (Delta SI-330-30, ATI; USA). In the vertical direction, after the wheel was lowered to the desired sinkage through the linear bushings, it is fixed by clamp levers to hold at the constant wheel sinkage during wheel rotation. As the description in Sec. 2.5, the angular positions of the three joints of the ALW were collected by three absolute encoders. The signals from the single incremental encoder and three absolute encoders were sampled at 166 Hz through a digital input/output board (NI-6001, National Instrument; USA) on a PC running a Windows XP operating system. From the encoder data, we can extract the real trajectory of the lug. The force signals were sampled by an A/D board (AD12-16(PCI), Contec; Japan) at the same rate used for digital data acquisition from encoders. The experimental soil is the same soil used in Sec. 3.2.2.

4.2.3 Experimental Procedure

The experimental procedure was as follows.

- i. Determine the motion parameters (θ_1 , α , l_s) from Table 4.1.

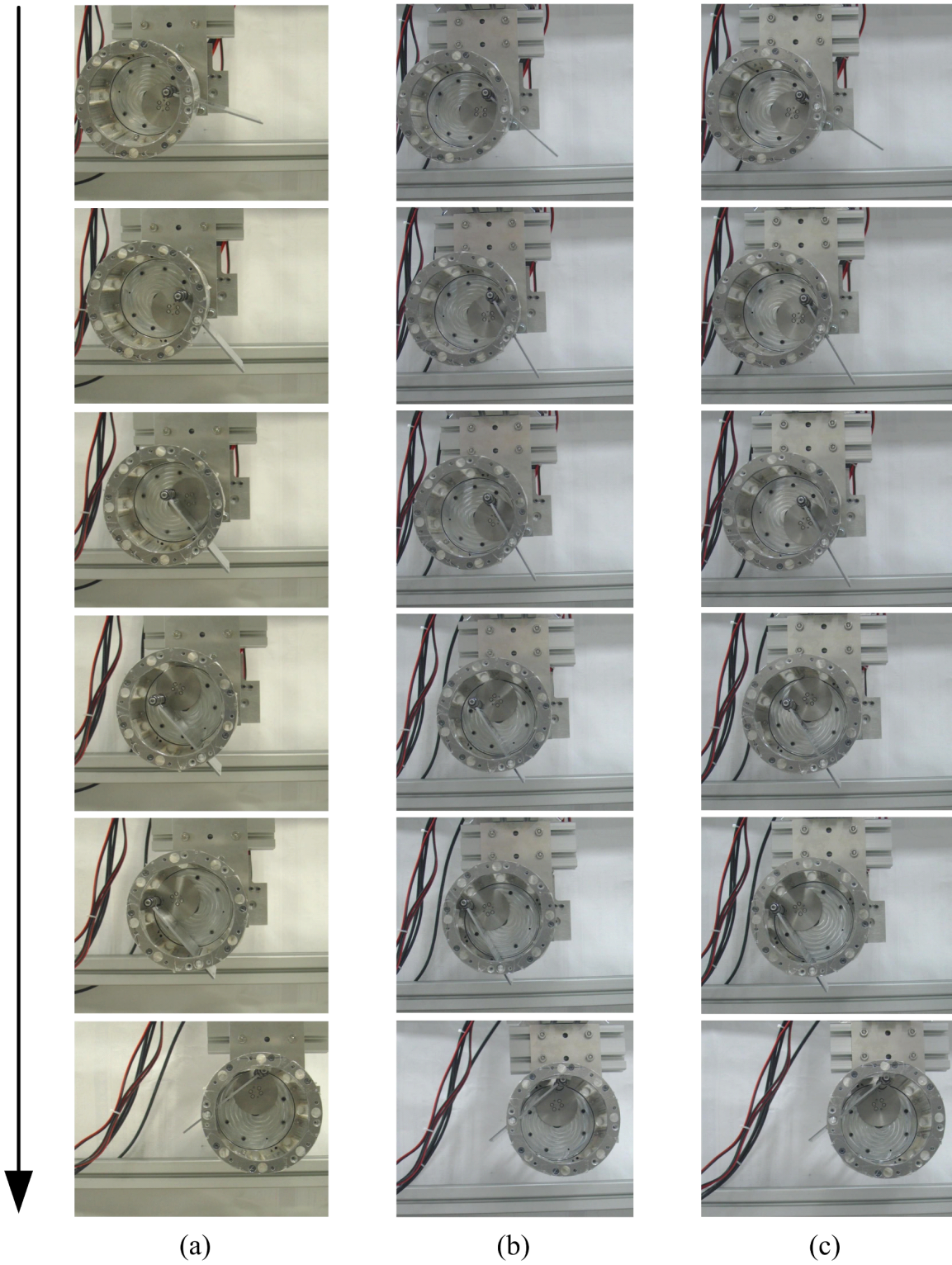
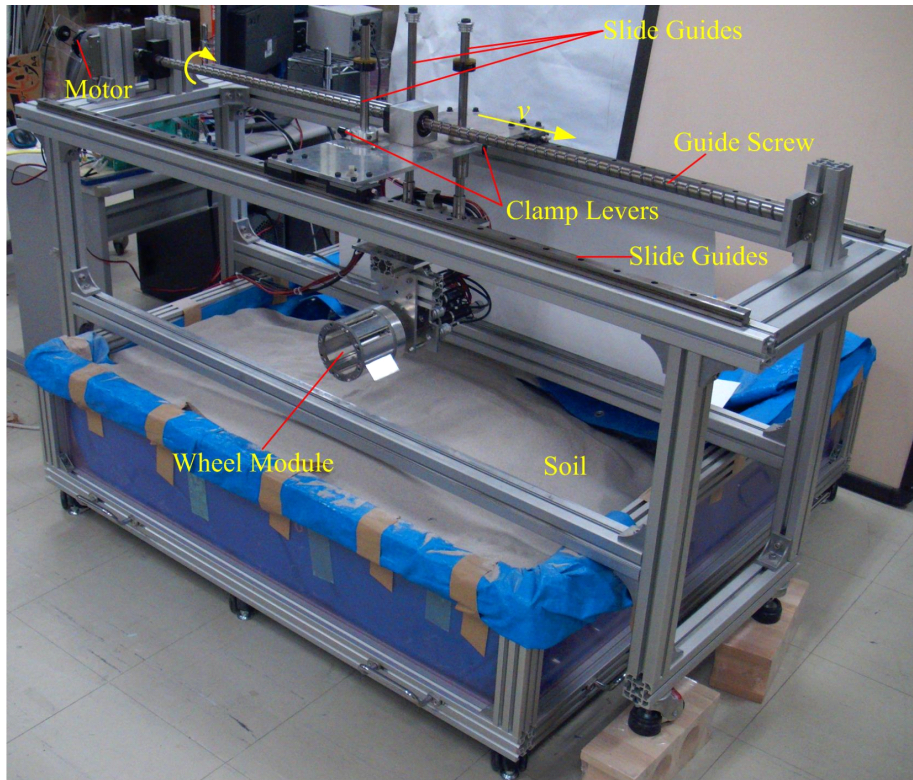
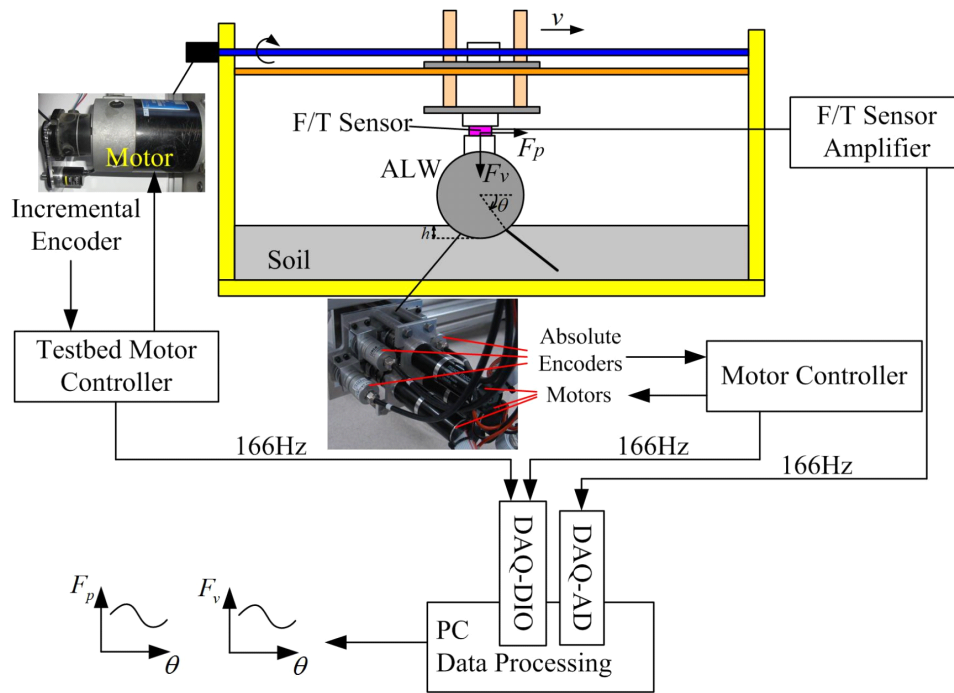


Figure 4.4. Actual lug trajectory of the ALW at (a) $\theta_1 = 20^\circ$, $\alpha = 50^\circ$, $l_s = 18$ mm, (b) $\theta_1 = 20^\circ$, $\alpha = 60^\circ$, $l_s = 18$ mm, (c) $\theta_1 = 20^\circ$, $\alpha = 60^\circ$, $l_s = 22$ mm.



(a)



(b)

Figure 4.5. (a) ALW-soil interaction testbed, (b) data acquisition system.

- ii. Make the soil uniform and smooth to ensure reproducibility of the experiments.
- iii. Calibrate the force/torque sensor. While the wheel was suspended, the reference values of the sensor can be obtained easily by clicking the “Calibration” button of the control software.
- iv. Lower the wheel at its initial state.
- v. Start the motors and run the data acquisition program.
- vi. Stop the motors and record the experimental data.
- vii. Repeat the above steps to finish all experiments.

4.2.4 Data Processing

Similar with the data processing method in Sec. 3.2.4, the force signal was extracted from the original noisy signal using the Daubechies-5 (db5) wavelet at level 5, by which noise with frequency exceeding 3.5 Hz was removed from sensor signals corresponding to the sampling rate (166 Hz) in the test system. In all experiments, 10 trials were conducted in each configuration and results are presented as their mean values.

An example ($\theta_1 = 20^\circ$, $\alpha = 50^\circ$, $l_s = 18$ mm) was taken to show the effect of data processing method. The noisy raw data from the force sensor (Fig. 4.6 (a)) was smoothed by the DWT application (Fig. 4.6 (b)). The reported result in each configuration is the mean of ten trials. The acceptable repeatability of the experiments is demonstrated in Fig. 4.6 (c).

4.3 Experimental Results

The effects of lug sinkage length and inclination angle on the ALW-soil interaction forces are shown in Figs. 4.7 and 4.8, respectively. In these figures, the sign of the forces is consistent with the coordinate system described in Fig. 4.3; that is, a positive drawbar

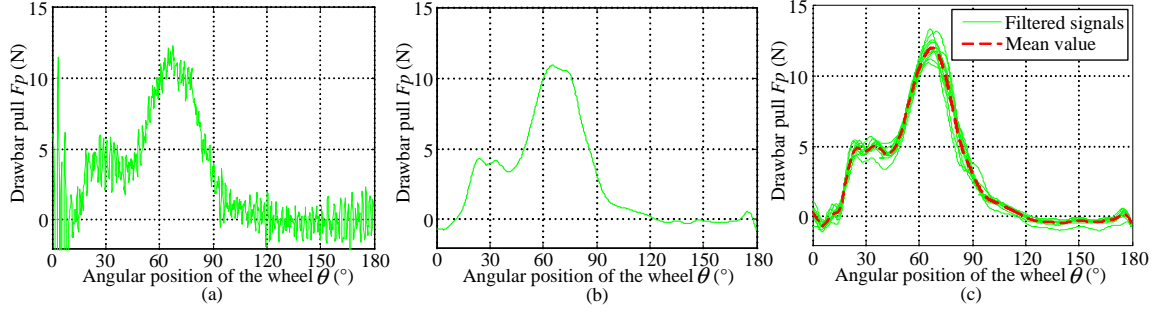


Figure 4.6. Removal of noise from measured forces: (a) original signal measured during one experimental trial, (b) filtered signal, and (c) filtered signals from ten experimental trials and their mean (red dashed line).

pull encourages forward movement of the wheel, while a negative vertical force prevents the wheel from sinking.

The characteristics of ALW-soil interaction forces shown in Fig. 4.7 exhibit similar trends. As a representative, the drawbar pull measured at $\theta_1 = 20^\circ$, $\alpha = 60^\circ$, $l_s = 18$ mm (magenta dashed line in Fig. 4.7 (b1)) is analyzed in following successive stage.

- i. Following contact between the lug and soil, the drawbar pull increased in phase I. A slight decrease occurred as the lug motion shifted from phase I to phase II at around 20° wheel rotation. This decrease is attributable to discontinuity in the lug-tip velocity as the lug motion switches from phase I to phase II, as shown in Fig. 4.2 (d).
- ii. After a slight fluctuation as the wheel proceeded from 20° to 40° , the drawbar pull sharply increased to its peak value at wheel rotational angle about 67° . According to the ground swell phenomenon observed from single lug experiment in Sec. 3.4.1, we deduce that as the lug bulldozes the soil, the ground in front of the lug tends to swell. However, this swelling is inhibited by the rigid wheel rim, which also exerts a surcharge on the ground. Thus, the drawbar pull are enhanced by the lug motion (Fig. 4.9 (a)).
- iii. As the lug moves backward, increasing quantities of soil flow and swell behind the wheel, and the effect of the wheel rim gradually disappears. Consequently, the reaction force decreased until θ rotates around 100° (Fig. 4.9 (b)).

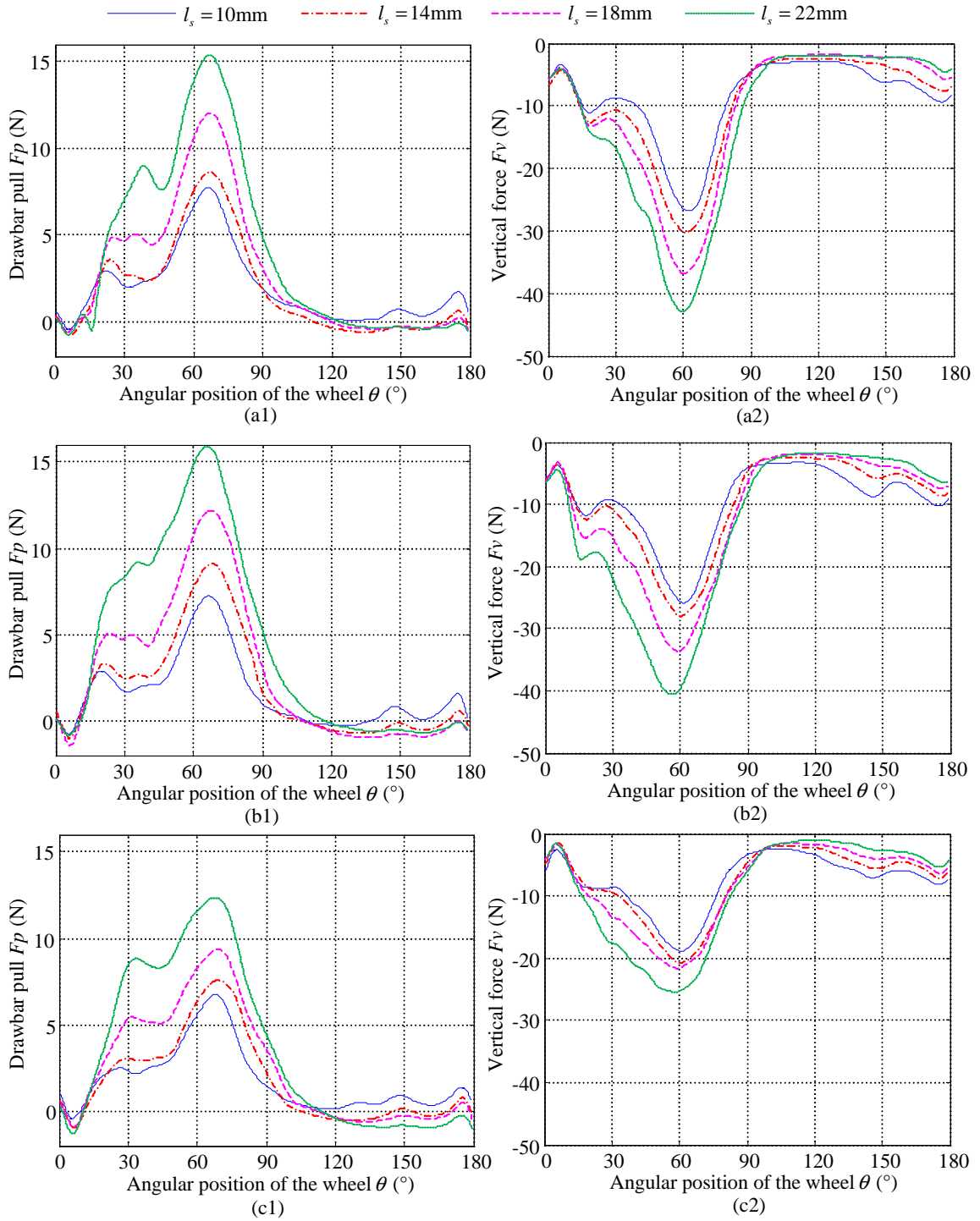


Figure 4.7. Drawbar pulls (left panels) and vertical forces (right panels) at selected sinkage lengths l_s and inclination angles α of (a) 50° , (b) 60° , and (c) 70° .

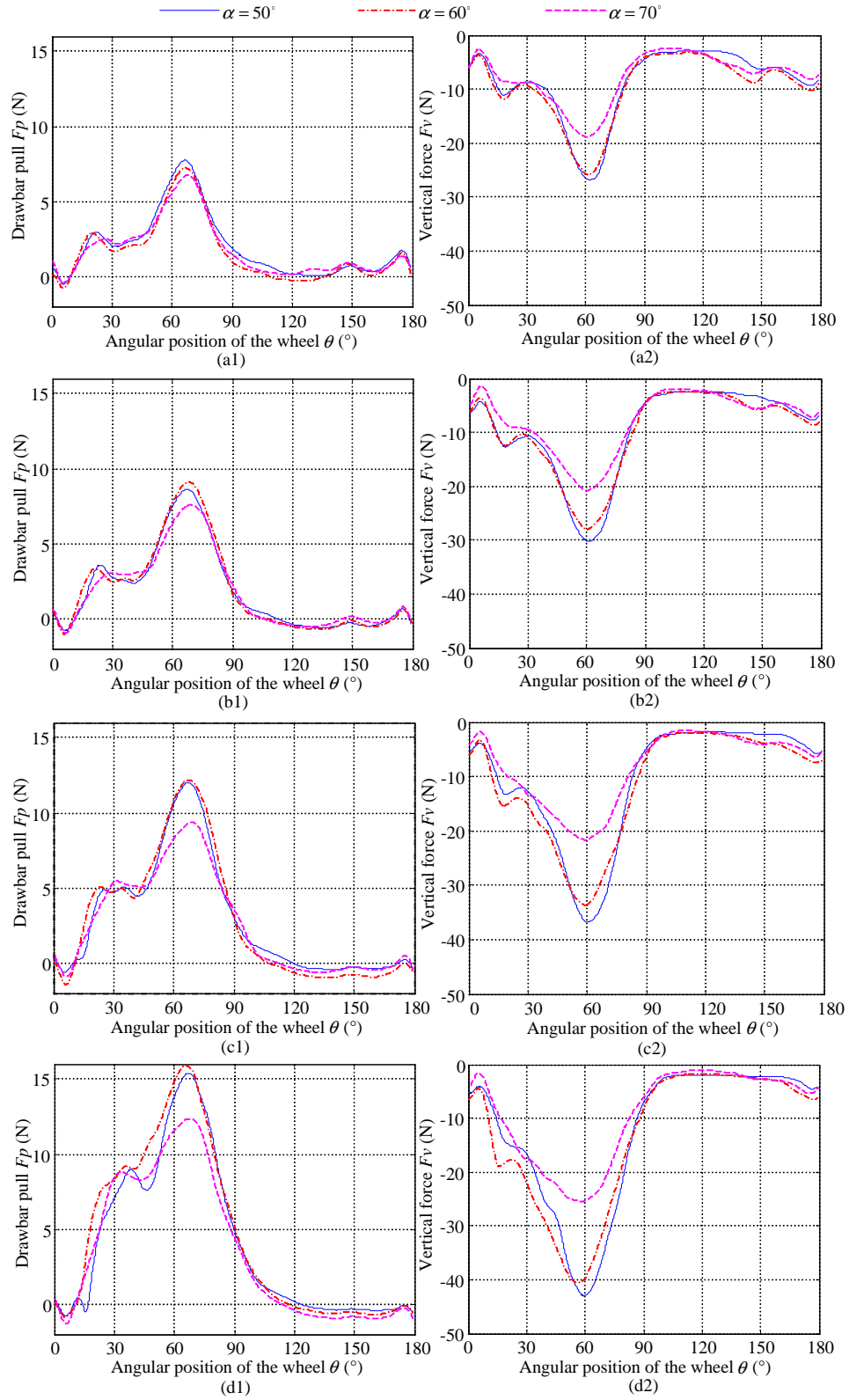


Figure 4.8. Drawbar pulls (left panels) and vertical forces (right panels) at selected inclination angles α and sinkage lengths l_s of (a) 10 mm, (b) 14 mm, (c) 18 mm, and (d) 22 mm.

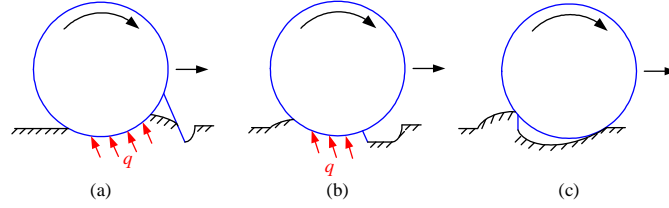


Figure 4.9. ALW-soil interaction process: (a)→(b)→(c).

- iv. Throughout the remaining period, the drawbar pull remained at approximately 0 N due to the soil structure beneath the wheel has been previously dug and changed by the lug (Fig. 4.9 (c)).

4.3.1 Sinkage Length Dependency

To investigate the effect of lug sinkage length on soil reaction forces, measurements were performed by maintaining the lug sinkage length at 10 mm, 14 mm, 18 mm, 22 mm (in phase II), respectively. As seen in Fig. 4.7, lug sinkage length considerably affects both the drawbar pull and vertical force obtained by the ALW.

In particular, the drawbar pull increases with increasing sinkage length (Fig. 4.7 (b1)). The maximum drawbar pull at sinkage lengths of 10 mm, 14 mm, 18 mm, and 22 mm was approximately 7.2 N, 9.1 N, 12.2 N, and 15.9 N, respectively.

The vertical force also increases with increasing sinkage length, but sinkage length does not affect the overall trends, as shown in Fig. 4.7 (b2). At sinkage lengths of 10 mm, 14 mm, 18 mm, and 22 mm, the vertical force peaks at approximately -25.9 N, -28 N, -33.7 N, and -40.5 N, respectively.

4.3.2 Inclination Angle Dependency

To investigate the effect of lug inclination angle on the ALW forces, the lug inclination angle (in phase II) was varied as 50°, 60°, and 70°. Fig. 4.8 shows the drawbar pull and vertical force acting on the ALW at each lug inclination angle.

The drawbar pull of the ALW was larger at inclination angles of 50° and 60° than at 70° (Fig. 4.8 (a1), (b1), (c1), and (d1)). For example, at a lug sinkage length of 18 mm (Fig. 4.8 (c1)), the maximum drawbar pulls at $\alpha = 50^\circ$ and $\alpha = 60^\circ$ were similar in trend, but 30% larger than at $\alpha = 70^\circ$. At $\alpha = 50^\circ$, 60° , and 70° , the drawbar pull peaked at approximately 12.0 N, 12.2 N, and 9.4 N, respectively. In all cases, the peak occurred at approximately 70° wheel rotation angle.

The characteristics of the vertical force are plotted in panels (a2), (b2), (c2), and (d2) of Fig. 4.8. As the lug inclination angle increases, the peak lift force declines. As shown in Fig. 4.8 (d2), the peak lift forces at lug inclination angles of 50° , 60° , and 70° were approximately -43.0 N, -40.5 N, and -25.4 N, respectively. The peak vertical force occurred at 60° rotation of the wheel, earlier than the peak drawbar pull.

4.4 Discussion

4.4.1 Effect of Lug Sinkage Length

As shown in Fig. 4.7, the larger the lug sinkage length, the greater the soil reaction force. This effect is attributable to the deeper soil penetration of a longer lug. The increased contact area with the soil enhances the lug forces. Therefore, by tuning the lug sinkage length, we can control the resultant force of the ALW module.

Table 4.2. Experimental peak values of drawbar pull F_p and vertical force F_v at different inclination angles α and sinkage lengths l_s .

l_s [mm]	$\alpha = 50^\circ$		$\alpha = 60^\circ$		$\alpha = 70^\circ$	
	F_p [N]	F_v [N]	F_p [N]	F_v [N]	F_p [N]	F_v [N]
10	7.7345	-26.8115	7.2370	-25.8607	6.7434	-18.8571
14	9.85	-32.8973	9.0935	-27.9570	7.5696	-20.7852
18	12.0114	-36.8247	12.1935	-33.6652	9.3795	-21.6077
22	15.4081	-42.9667	15.9141	-40.5281	12.3615	-25.4234

To elucidate how the lug sinkage length influences the maximum lug-soil interaction forces, we tabulate the maximum experimentally determined forces in Table 4.2. Inspired

from the experimental analysis in Chapter 3, for a fixed inclination angle, the relationships between l_s and maximal F_p and between l_s and maximal F_v can be approximated by the following quadratic functions.

$$F_p^{\max} = K_1^{F_p} l_s^2 + K_2^{F_p} l_s + K_3^{F_p} \quad (4.6)$$

$$F_v^{\max} = K_1^{F_v} l_s^2 + K_2^{F_v} l_s + K_3^{F_v} \quad (4.7)$$

The coefficients of (4.6) and (4.7) in the data fittings are summarized in Tables 4.3 and 4.4, respectively. The predicted maximum F_p and F_v , calculated by (4.6) and (4.7), respectively, are compared with the experimental results in Fig. 4.10. These comparisons confirm that F_p^{\max} and F_v^{\max} are quadratic functions of the sinkage length l_s at all inclination angles. In physical terms, as the lug sinks deeper into the soil, the soil reaction forces increase at a faster than linear rate.

Table 4.3. Coefficients of (4.6) determined by fitting to experimental data.

α [°]	$K_1^{F_p}$	$K_2^{F_p}$	$K_3^{F_p}$
50	0.02	-0.011	5.9025
60	0.0291	-0.2038	6.3309
70	0.0337	-0.6113	9.4973

Table 4.4. Coefficients of (4.7) determined by fitting to experimental data.

α [°]	$K_1^{F_v}$	$K_2^{F_v}$	$K_3^{F_v}$
50	-0.0009	-1.2817	-14.1251
60	-0.0745	1.1405	-29.6954
70	-0.0295	0.4308	-20.4203

However, longer lugs would also enhance fluctuations in the wheel sinkage, drawbar pull, and driving torque [31], and thus compromise the stability of the robot body. Based on the experimental results, Sutoh et al. pointed that if the lug height is increased, the lugs only contact with the ground at certain points, which may even decrease the traveling performance [34]. Therefore, on soft terrains, the lug should be deeply inserted into the

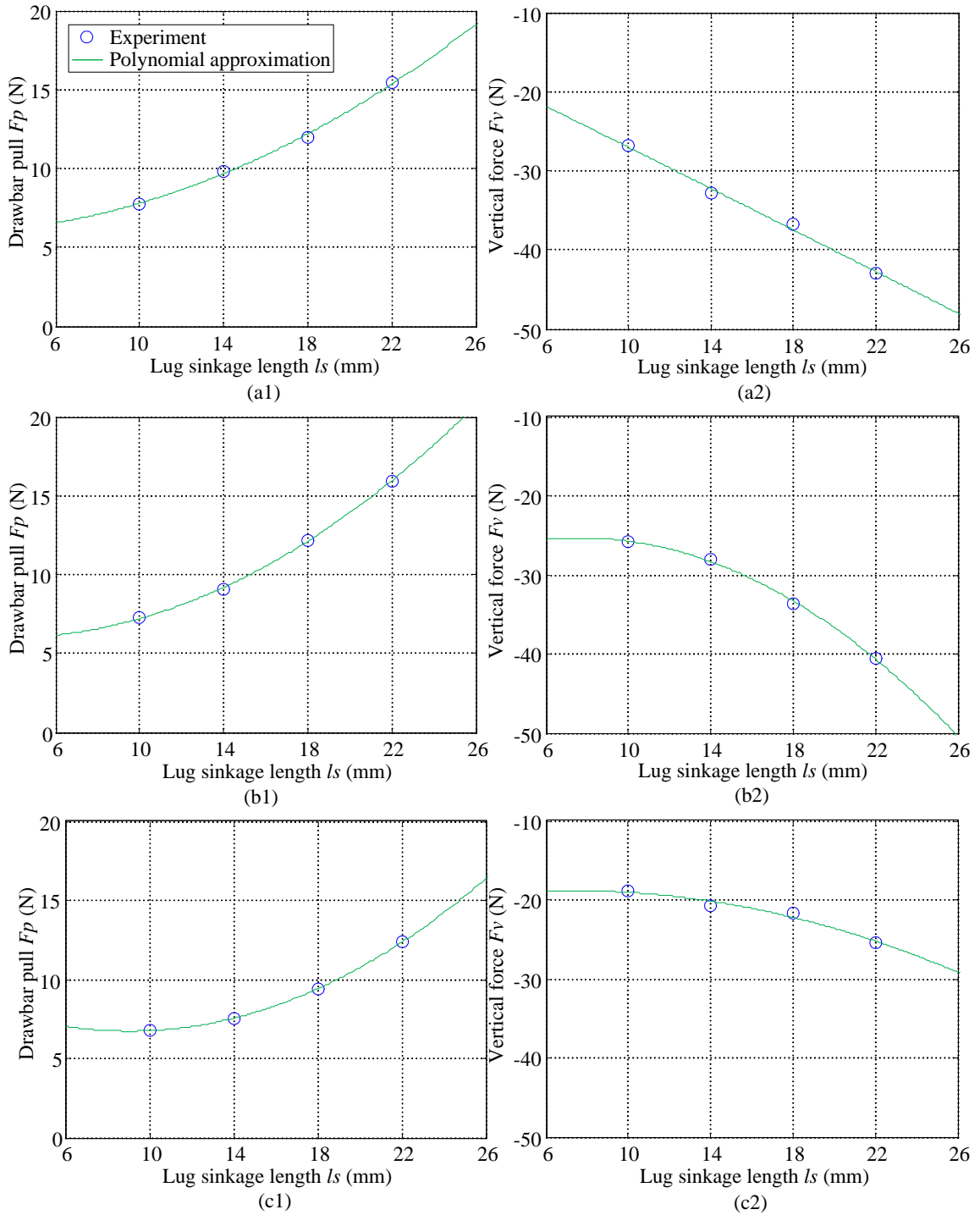


Figure 4.10. Drawbar pulls fitted by (4.6) (left panels) and vertical forces fitted by (4.7) (right panels). The inclination angles α are (a) 50° , (b) 60° , and (c) 70° .

soil but actively moved to suppress lug force fluctuations. On compacted rigid terrain, the robot might be effectively propelled by the thrust generated by friction between the wheel surface and ground. In this case, the lugs should protrude only a short distance or be completely retracted into the wheel; otherwise, the robot body will be periodically affected by lug-ground interactions.

4.4.2 Effect of Lug Inclination Angle

As evident in Fig. 4.8, a lug with a given sinkage length exerted higher peak drawbar pull and vertical force at 50° and 60° inclination angle than at 70°. To further investigate the effect of lug inclination angle, we calculated the ratio of drawbar pull F_p to vertical force F_v , defined as follows

$$\eta = \left| \frac{F_p}{F_v} \right| \quad (4.8)$$

As shown in Fig. 4.11, the ratio of drawbar pull to vertical force cannot be systematically related to the inclination angle throughout one ALW-soil interaction cycle. However, in general, the ratio increases with increasing inclination angle as the angular wheel position proceeds from 45° to 80°. In other words, when $\theta = 45^\circ - 80^\circ$, the drawbar pull makes an increasingly higher contribution to the soil reaction force as the inclination angle increases.

4.5 Summary

In this chapter, the drawbar pull and vertical force generated by the ALW equipped with a single lug were measured in sandy soil. The experimental results and analyses are summarized below.

- i. The sinkage length of the lug determines the resultant soil reaction force. The maximum drawbar pull and vertical force are quadratic functions of the lug sinkage length;

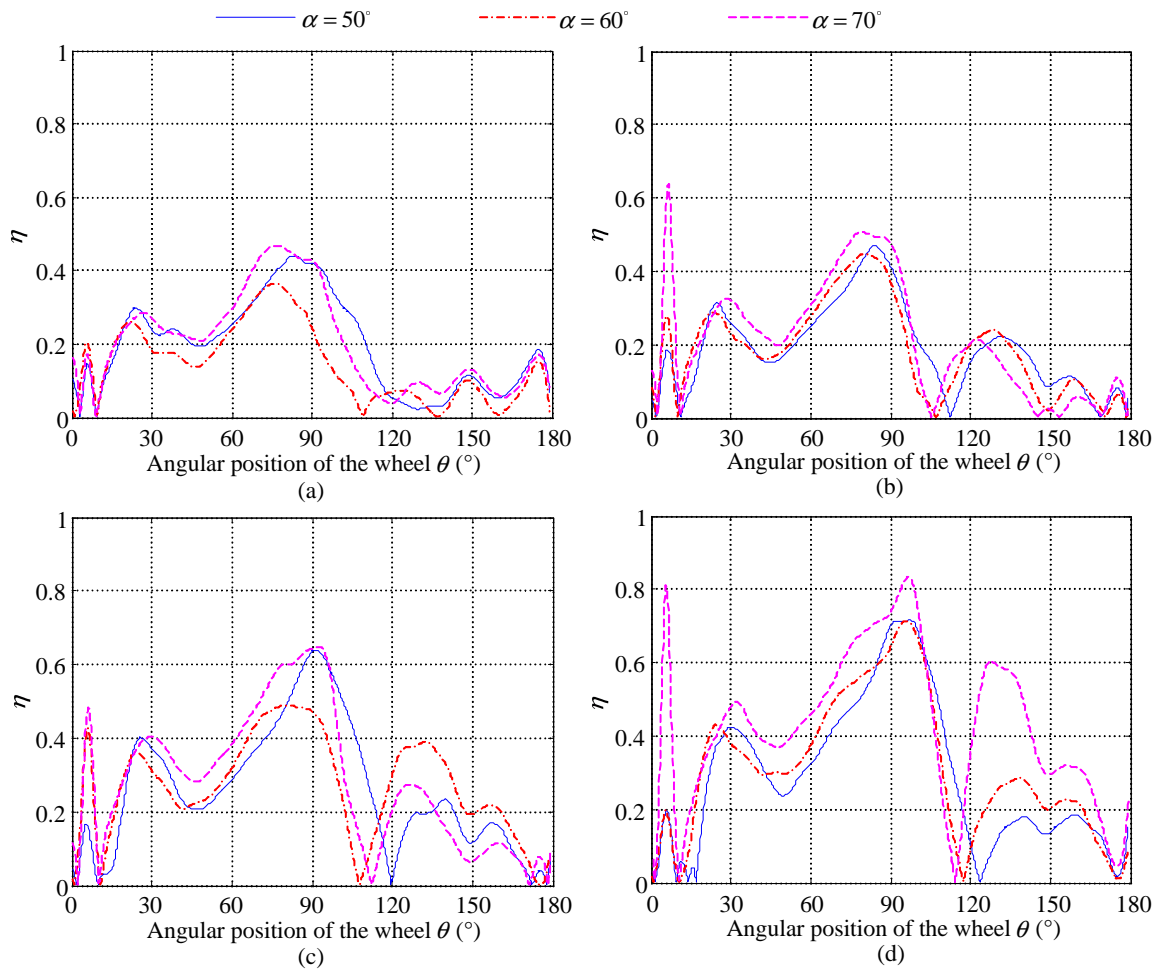


Figure 4.11. Ratio of drawbar pull to vertical force at selected inclination angles α and sinkage lengths l_s of (a) 10 mm, (b) 14 mm, (c) 18 mm, and (d) 22 mm.

that is, as the lug inserts deeper into the soil, the ALW-soil reaction forces increase at a faster than linear rate.

- ii. As the wheel rotates from 45° to 80° , the ratio of drawbar pull to vertical force increases with the increase of the lug inclination angle on the whole.

The experimental analysis in this chapter reveals obvious relationships between the lug trajectory and the ALW-soil interaction forces. We conclude that the ALW mechanism might improve the performance of mobile robots on difficult terrains. We thus proceed to test this potential improvement in Chapter 5.

Chapter 5

Performance Improvement by the ALW Mechanism

Comparing the experimental results from Chapter 3 and Chapter 4, we found that ALW-soil interaction mechanics exhibit several interesting characteristics. For example, the vertical force, which can prevent the device from the sinkage, can be significantly enlarged owing to the presence of the wheel rim. In addition, these experiments obviously demonstrated that the lug trajectory significantly affects the soil reaction forces, thus it is feasible to improve the traveling performance of locomotive device by controlling the lug motion in sandy environments.

In this chapter, we discuss how the wheel rim and the lug contribute to the ALW-soil interaction forces, and highlight the advantages of improving the ALW mechanism by tuning the lug trajectory. First, we experimentally confirm the wheel-lug interference, and discuss its effect on improving the lugged wheel-soil interaction forces. Then the drawbar pull and vertical force measured by the ALW in Chapter 4 are compared with those generated by a fixed lugged wheel to demonstrate the superior performance of the ALW mechanism. Further, we take the advantage of kinematic ability of the ALW to reduce fluctuations in the drawbar pull. By tuning the lug sinkage length of the active lug, the developed

wheeled mechanism can reduce the fluctuations of the drawbar pull that arise when using the conventional fixed lugged wheel.

5.1 Experimental Overview

Unless otherwise mentioned, in all experiments in this chapter, the wheel rim sinkage was fixed at 5 mm. The wheel rim was rotated from 0° to 180° at a constant angular speed of $30^\circ/s$. The traveling velocity was 20 mm/s, yielding a slip ratio (calculate from (4.1)) of 0.3. The ALW-soil interaction testbed, experimental soil, experimental procedure and data processing method were the same with the introduction in Sec. 4.2.

5.1.1 Wheel Configurations

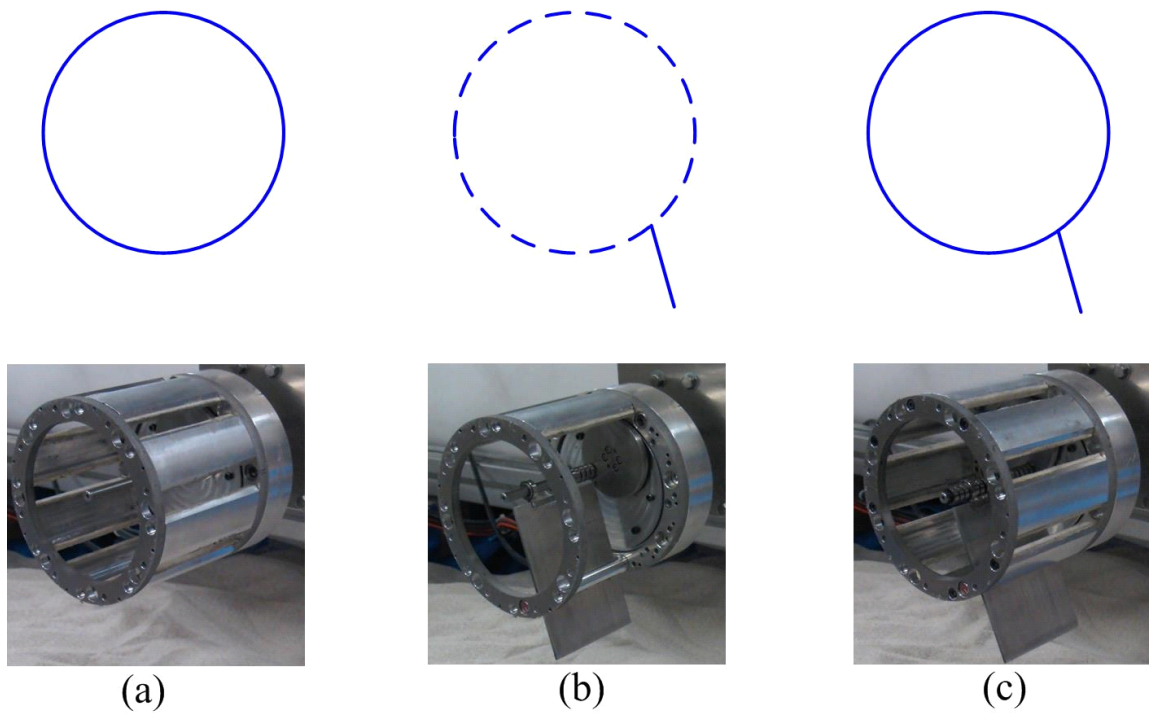


Figure 5.1. Experimental wheel types: (a) Smooth Wheel (SW), (b) Cage Lugged Wheel (CLW), (c) Active Lugged Wheel (ALW).

To evaluate how the wheel rim and lug contribute to the drawbar pull and vertical force, we measured the soil reaction forces generated by a Smooth Wheel (SW) and a Cage

Table 5.1. Values of lug motion parameters (in phase II) adopted in the Cage Lugged Wheel (CLW) experiments.

Initial rotational angle θ_1 [°]	Inclination angle α [°]	Sinkage length l_s [mm]
20	50	14
20	60	18
30	70	18

Lugged Wheel (CLW). The experimental results were compared with those of the ALW with the same lug trajectory presented in Chapter 4. As shown in Fig. 5.1, the SW and CLW were respectively obtained by disassembling the lugs and the wheel rims from the ALW. Therefore, all three wheels were of identical radius and width. All combinations of lug motion parameters (in phase II) adopted in the CLW are tabulated in Table 5.1.

5.1.2 Motion Sequence of the Fixed Lugged Wheel

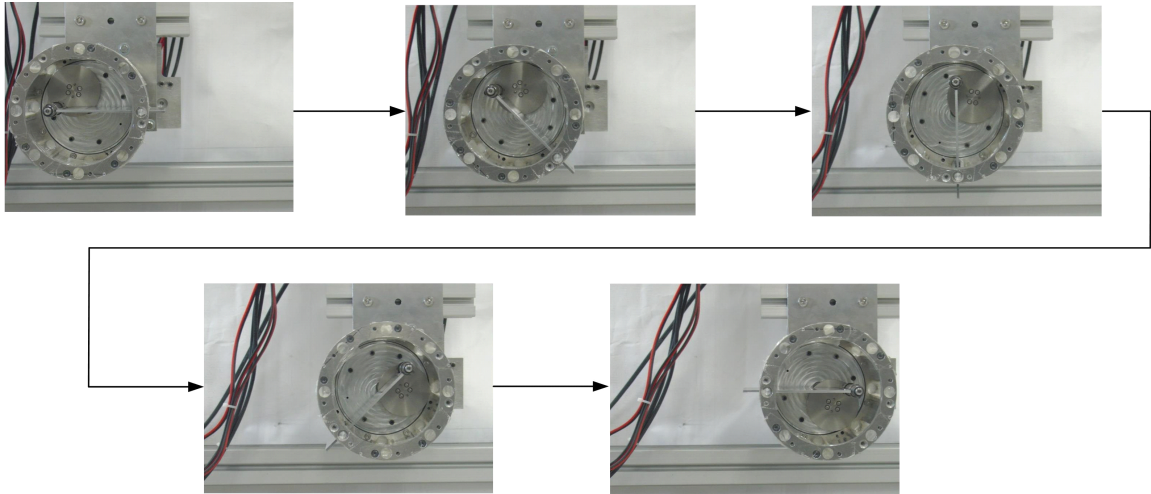


Figure 5.2. Motion behavior of the prototype to simulate a wheel with a fixed lug of 13 mm height.

Having experimentally confirmed the merits of installing both rim and lugs on the wheels, we compared the drawbar pull and vertical force of a fixed-lugged wheel and the ALW. As shown in Fig. 5.2, the locomotion of the wheel fitted with a fixed lug of 13 mm height is performed by the ALW mechanism, thus two wheels were of identical radius and width.

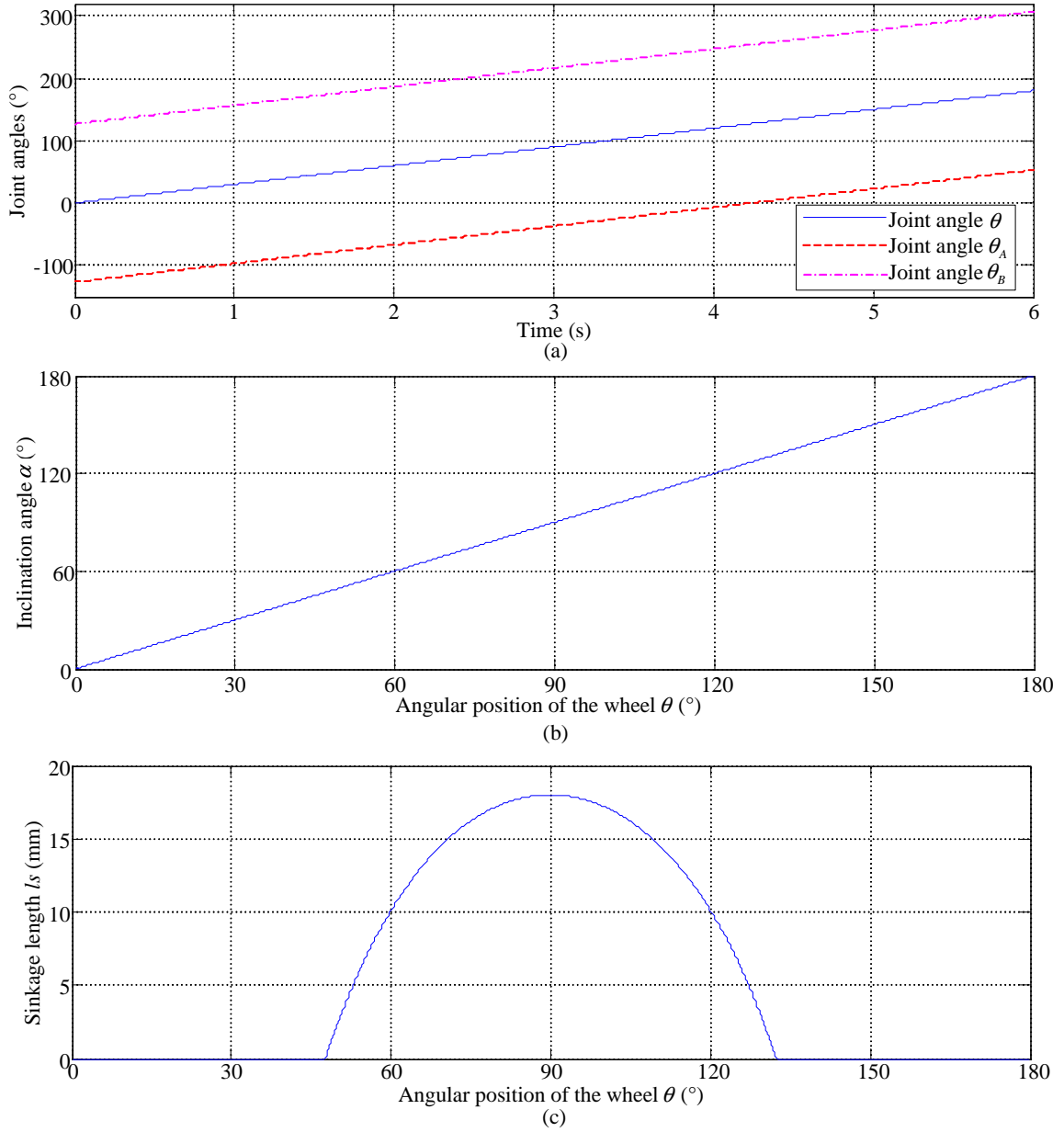


Figure 5.3. Locomotion of a wheel fitted with a fixed lug of 13 mm height at wheel sinkage $h = 5$ mm. (a) Joint angles calculated from (2.8), (b) lug inclination angle, (c) lug sinkage length.

Different from the lug trajectories described in Chapter 4, both the lug inclination angle and lug sinkage length of the fixed lugged wheel were continuously changed during the wheel rotation. As shown in Fig. 5.3, while the inclination angle increased from 0° to 180° , the lug sinkage length increased to its maximum of 18 mm and then decreased. Positive sinkage length means that the lug is contacting to the soil to gain the soil reaction forces. Therefore, comparing with Fig. 4.2 (c), it can be found that lug-soil interaction time of the ALW mechanism is longer than that of the fixed lugged wheel.

5.1.3 Fluctuation Reduction in Drawbar Pull

Clearly, the drawbar pull depends on the locomotion of the traveling mechanism. In this chapter, the advantage of the ALW is further taken to reduce fluctuations in the drawbar pull. Based on the curves plotted in Fig. 4.7, we deduce that it is possible to reduce fluctuations in drawbar pull by protruding the lug longer in the initial stage to achieve the desired force as early as possible, and subsequently gradually adjust the lug sinkage length to prevent the drawbar pull from rapidly declining.

In this study, we selected six lug trajectories in which the drawbar pull fluctuations were diminished by adjusting the lug sinkage length during wheel rotation. These trajectories were known from our previous experience. Different from the experimental trajectories of Chapter 4, the lug sinkage length continuously altered in phase II. Here, the lug trajectory in phase II was determined by an additional three points, (θ_a, l_{sa}) , (θ_b, l_{sb}) , and (θ_c, l_{sc}) , whose geometries are represented in Fig. 5.4. During wheel rotation from θ_1 to θ_a , the lug was driven to a constant sinkage length of l_{sa} ; as the wheel advanced from θ_a to θ_b to θ_c , the lug sinkage length linearly changed from l_{sa} to l_{sb} to l_{sc} and was maintained at l_{sc} until the end of phase II. The lug motions in phases I and III were identical to those described in Sec. 4.2.1.

At each inclination angle, the drawbar pull was smoothed by two trajectories. The motion parameters are tabulated in Table. 5.2. As an example, the joint angles, lug sinkage

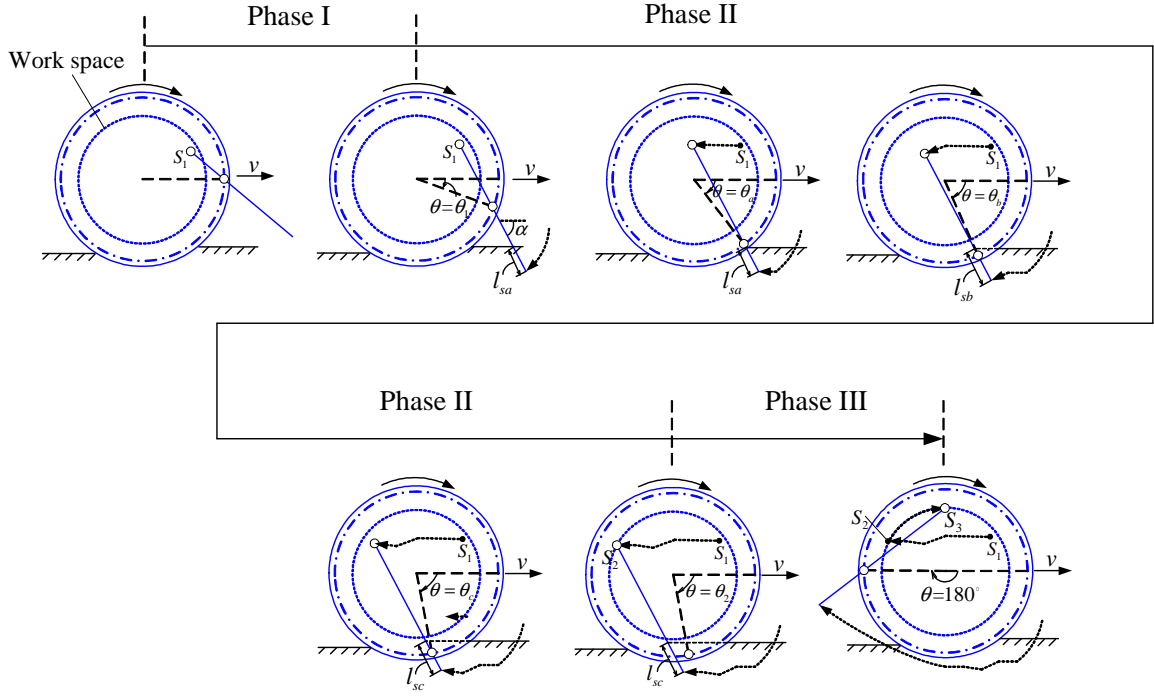


Figure 5.4. Lug trajectory within a complete lug-soil interaction process as the wheel rotates from 0° to 180° for reducing the fluctuation of drawbar pull.

length, lug inclination angle of the ALW with trajectory “Inc60-II” are plotted in Fig. 5.5, and photographs of the actual motional behavior are displayed in Fig. 5.6.

Table 5.2. Values of motion parameters adopted in the experiments.

α [°]	θ_1 [°]	θ_a [°]	l_a [mm]	θ_b [°]	l_b [mm]	θ_c [°]	l_c [mm]	Codes
50	20	22	14	45	17	53	0	Inc50-I
	20	45	18	55	0	75	12	Inc50-II
60	20	22	14	42	15	53	0	Inc60-I
	20	45	18	55	2	75	12	Inc60-II
70	30	31	14	45	16	65	2	Inc70-I
	30	40	18	50	0	80	16	Inc70-II

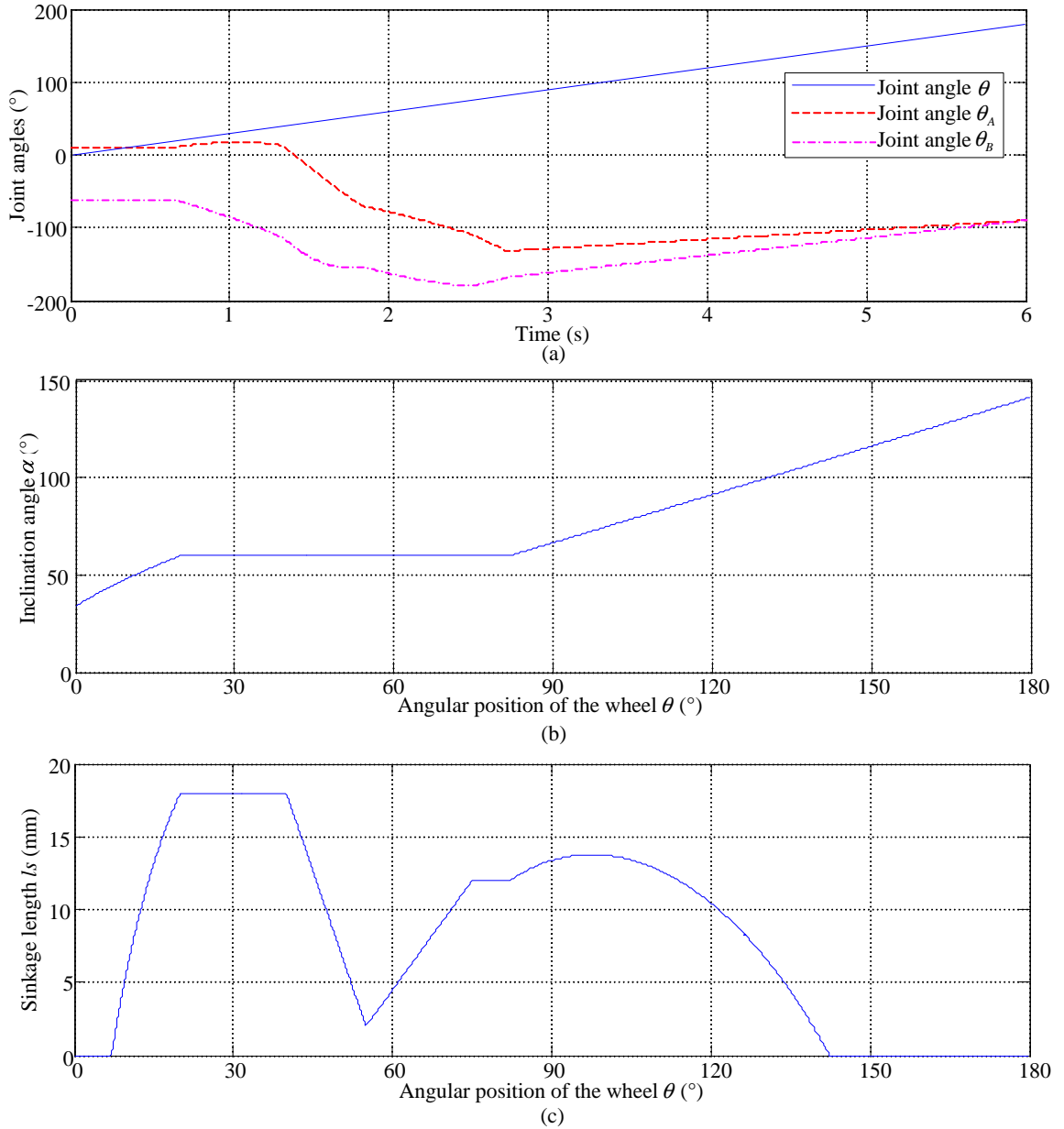


Figure 5.5. Locomotion of the ALW at initial rotational angle $\theta_1 = 20^\circ$, inclination angle $\alpha = 60^\circ$ (in phase II), $\theta_a = 40^\circ$, $l_{sa} = 18$ mm, $\theta_b = 55^\circ$, $l_{sb} = 2$ mm, $\theta_c = 75^\circ$, $l_{sc} = 12$ mm, and wheel sinkage $h = 5$ mm. (a) Joint angles calculated from (2.8), (b) lug inclination angle, (c) lug sinkage length.

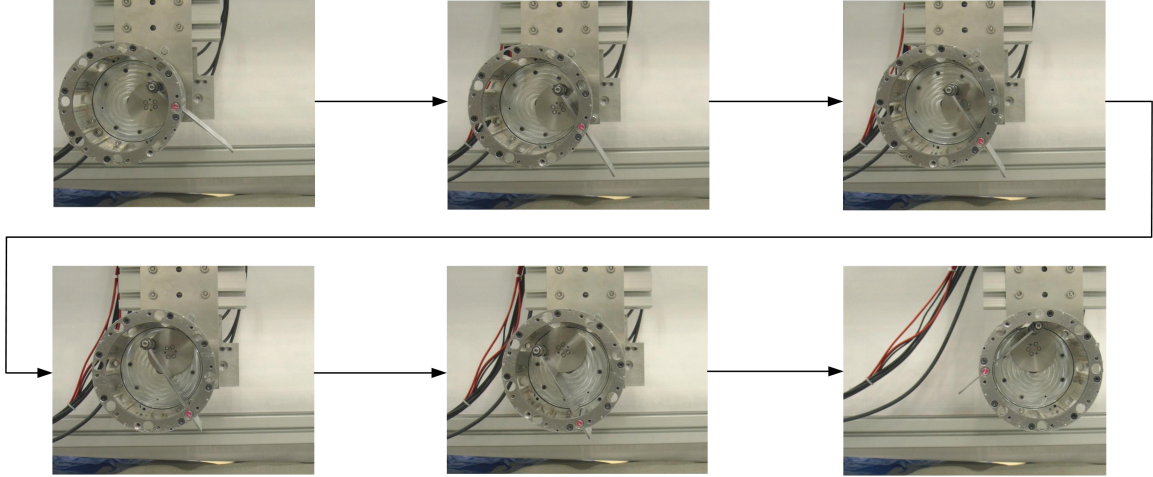


Figure 5.6. Actual lug trajectory of the ALW at trajectory “Inc60-II”.

5.2 Experimental Results and Discussion

5.2.1 Confirmation of Wheel-lug Interference

The evaluation results of the SW, LCW, and ALW are compared in Fig. 5.7. The smooth wheel generated a slight drawbar pull and vertical force; these forces are the resultant of the normal and shear stresses acting on the wheel surface. In general, the soil reaction forces generated by smooth wheels are insufficient to extricate the robot from loose soil if the robot becomes trapped therein.

The soil reaction forces significantly increased due to the presence of the lugs. As shown in Fig. 5.7 (b1) ($\theta_1 = 20^\circ$, $\alpha = 60^\circ$, $l_s = 18$ mm), the maximum drawbar pulls of the CLW and ALW were 200% and 400% higher, respectively, than the SW drawbar pull. In contrast, the CLW generally exerted less vertical force than the SW (Fig. 5.7 (b2)). This implies that the lugs effectively enlarge the drawbar pull by their shearing movements, while the wheel rim can prevent wheel sinkage. Therefore, the lugged wheel is a better configuration than smooth-wheeled or lug-only devices for accessing soft terrains.

To confirm the wheel rim-lug interference, the ALW-soil interaction forces were compared with the sum of the SW-soil and the CLW-soil interaction forces. The results are

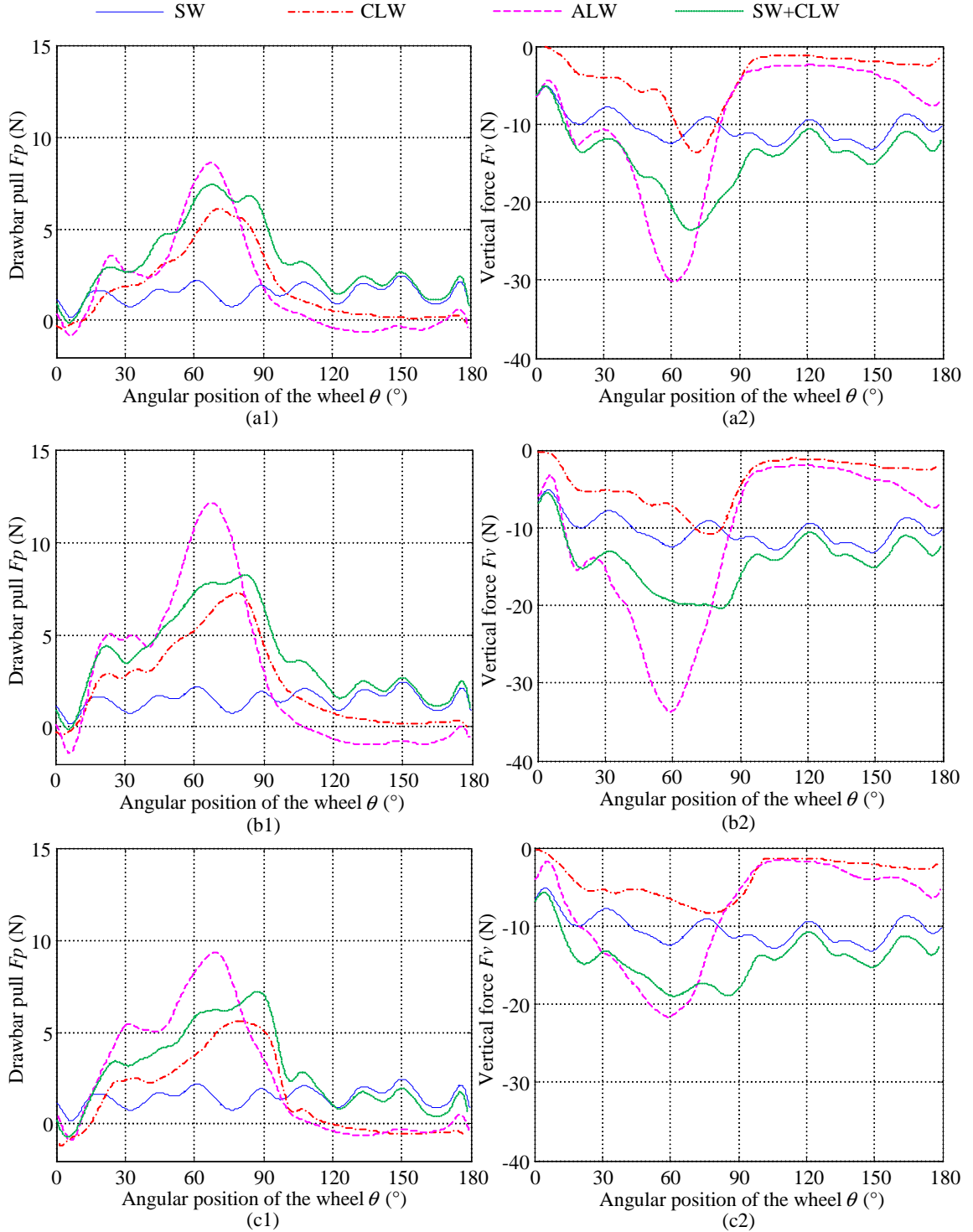


Figure 5.7. Comparison of drawbar pulls (left panels) and vertical forces (right panels) generated by the Smooth Wheel (SW), the Lugged Cage Wheel (LCW), the ALW, and the sum of SW and LCW (SW + LCW), at initial rotational angles θ_1 , inclination angles α and sinkage lengths l_s of (a) $\theta_1 = 20^\circ$, $\alpha = 50^\circ$, $l_s = 14$ mm, (b) $\theta_1 = 20^\circ$, $\alpha = 60^\circ$, $l_s = 18$ mm, (c) $\theta_1 = 30^\circ$, $\alpha = 70^\circ$, $l_s = 18$ mm.

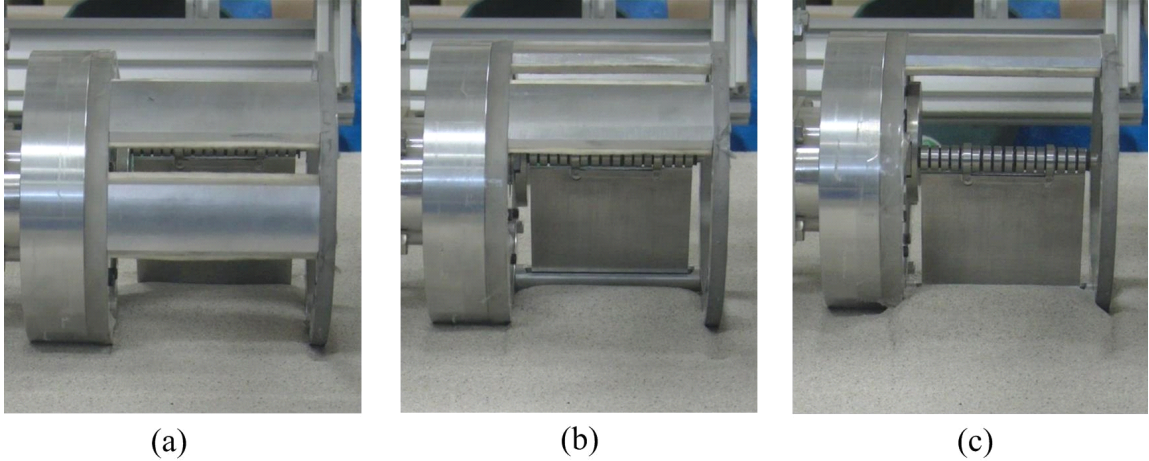


Figure 5.8. The phenomenon of ground swell photographed as the wheel rolls from (a) \rightarrow (b) \rightarrow (c).

plotted as the green curves in Fig. 5.7. Taking Fig. 5.7 (b) as an example, we observe that as θ ranges from 42° to 78° , the ALW generates a larger drawbar pull and vertical force than the sums of the respective forces generated by the SW and CLW. Similar with the findings from the single lug experiments in Sec. 3.4.1, the ground swell due to excavation of the lug has also been observed in the CLW-soil interaction experiments as shown in Fig. 5.8. Therefore, we deduce that as the lug bulldozes the soil, the ground in front of the lug tends to swell. However, this swelling is inhibited by the rigid wheel, and thus the soil between the wheel and the lug will be compacted. This will enlarge the normal stress acting on the wheel rim, and further enlarge the wheel-rim interaction forces. Moreover, the compaction will enlarge the surcharge and thus enlarge the lug-soil interaction forces. Because of this property of dry sand, lugged wheel can achieve better performance than other locomotion mechanism on sandy terrains. Although the ALW-soil interaction forces were smaller than the sum of the SW and the CLW after the wheel rotational angle passed 78° , the multi-lug could overcome this problem, which will be investigated in future research.

These experimental results confirm that the wheel rim and lugs interfere to enhance the drawbar pull and vertical force. Therefore, the ALW can exploit the deformation property of the sandy soil to strengthen the interaction forces. In contrast, such complex soil deformation complicates the modeling of the lugged wheel-soil interaction. For simplicity,

most studies have separately modeled the wheel-soil and lug-soil interaction forces and summed them to estimate the lugged wheel-soil interaction forces. However, ignoring the wheel-lug interference may jeopardize the model precision.

5.2.2 Soil Reaction Forces of Two Lugged Wheels

The lugged wheel is a better configuration for locomotive modules in sandy environments than lugs or wheel rims alone. In this section, the drawbar pull and vertical force of a fixed lugged wheel were measured and compared with the ALW results plotted in Fig. 4.7. The aim was to demonstrate the performance improvement conferred by the ALW mechanism.

For wheels fitted with a single fixed lug of height 13 mm, the lug sinkage length was maximized at 18 mm at a wheel sinkage of 5 mm on sandy terrain. A slight drawbar pull (or vertical force) was induced just before the lug contacted the ground (black dashed line in Fig. 5.9). Once the lug reached the soil, the drawbar pull (or vertical force) rapidly increased to its peak value at 70° rotation of the wheel and rapidly decreased thereafter. For the wheel equipped with multi-lugs, rapid increase and decrease of the soil reaction forces over such a short period inevitably cause unwanted oscillations in the sinkage, traveling velocity, driving torque, etc. as the individual lugs interact with the soil, and consequent destabilize the vehicle.

The advantages of fitting the wheels with active lugs are summarized below.

- i. The ALW mechanism is able to insert the lug into the soil earlier in the cycle and depart from the soil later to increase the drawbar pull and vertical force over a wider range. It is attributed to the lug-soil interaction time analyzed in Sec. 5.1.2.
- ii. The maximum force is obtained at a slightly earlier angular position of the wheel rim in the ALW mechanism than in the fixed lugged wheel.
- iii. Compared to the fixed lugged wheel with a maximum sinkage length of 18 mm, the maximum drawbar pull of the ALW at 18 mm sinkage length (magenta dashed line

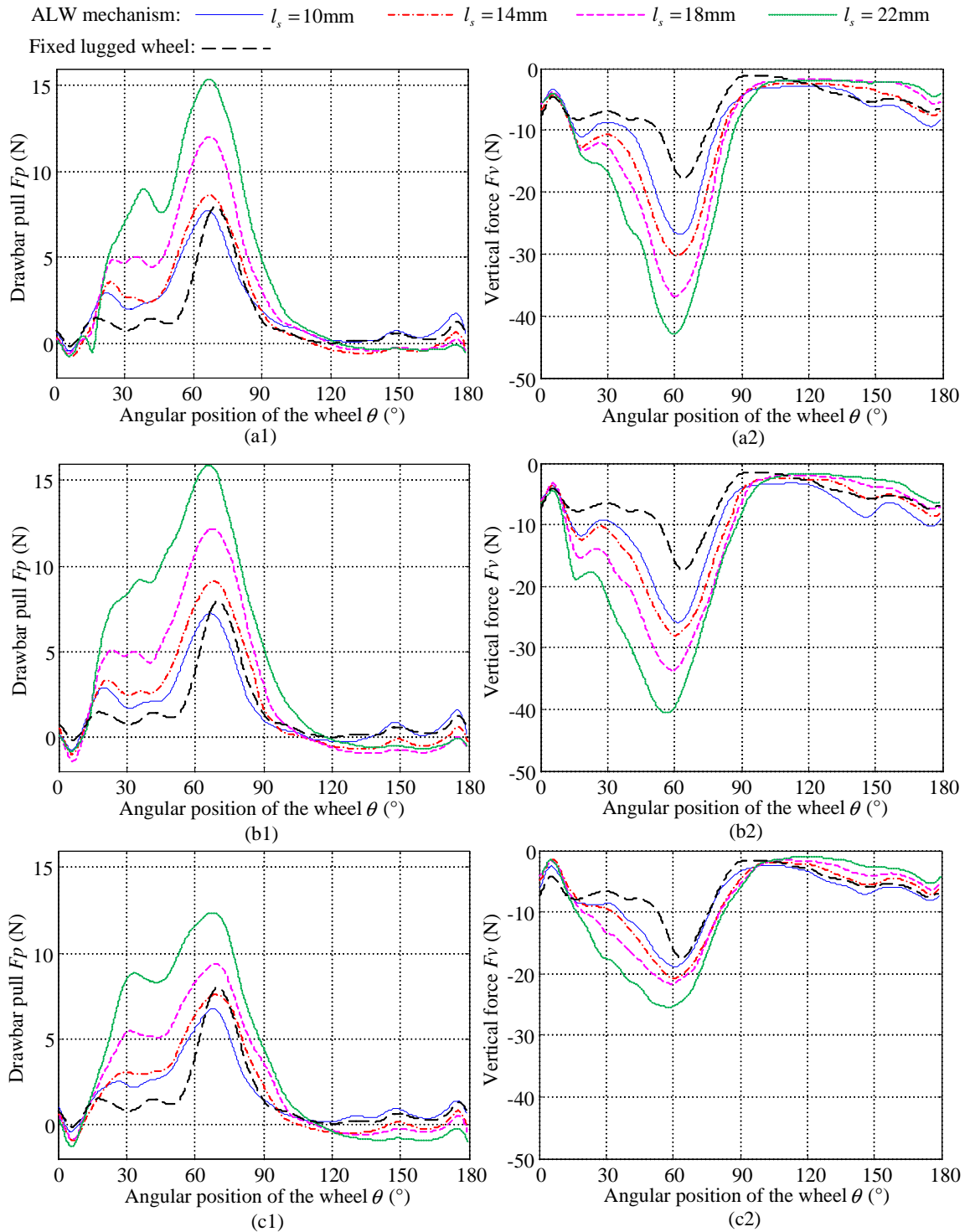


Figure 5.9. Comparison of drawbar pulls (left panels) and vertical forces (right panels) generated by a fixed lugged wheel (lug height = 13 mm) and by the ALW mechanism at selected sinkage lengths l_s and inclination angles α of (a) 50°, (b) 60°, and (c) 70°.

in Fig. 5.9) is increased by 51% ($\alpha = 50^\circ$), 53% ($\alpha = 60^\circ$), and 18% ($\alpha = 70^\circ$) (see Fig. 5.9 (a1), (b1), and (c1)).

- iv. The ALW mechanism significantly enhances the vertical force (Fig. 5.9 (a2), (b2), and (c2)). We deduce that because the ALW interacts with the soil over a longer period, a greater soil volume is excavated and swelled. The increased vertical reaction force imparted to the wheel rim can reduce the sinkage of the ALW mechanism in practical applications.

Therefore, we confirm that the ALW mechanism generates a more effective drawbar pull and vertical force over a wider range than the conventional fixed-lugged wheel.

5.2.3 Effectiveness of the Fluctuation Reduction Method

As shown in Fig. 5.9, although the ALW improves the force characteristics, the drawbar pull largely varies if the inclination angle and lug sinkage length remain constant during phase II. Therefore, we must generate a lug trajectory that weakens the unwanted oscillations in the ALW-soil interaction forces. Because of the complicated soil deformation, we have yet to find an acceptable strategy to achieve this goal. We illustrate this point on the six trajectories tabulated in Table. 5.2. These trajectories were derived from experience gained during our extensive experimental tests.

The experimental results are plotted in Fig. 5.10. The drawbar pull can be stabilized around a value within a certain range. For example, the drawbar pull of trajectory “Inc60-II” was approximately 7.5 N in the range of $[20^\circ, 65^\circ]$ of wheel rotation angle. For each inclination angles, two trajectories were given. As shown in Fig. 5.10 (b1), it also can decrease the fluctuations in the drawbar pull in the range $[17^\circ, 55^\circ]$ of wheel rotation angle as adopting trajectory “Inc60-I”. The small fluctuated drawbar pull (about 6.5 N) was smaller than that generated in trajectory “Inc60-II”. Therefore, it is possible to achieve force control by adjusting the lug sinkage length to ensure that the wheel moves with a small amount of slippage. As an additional practical application in challenging environments, a robot

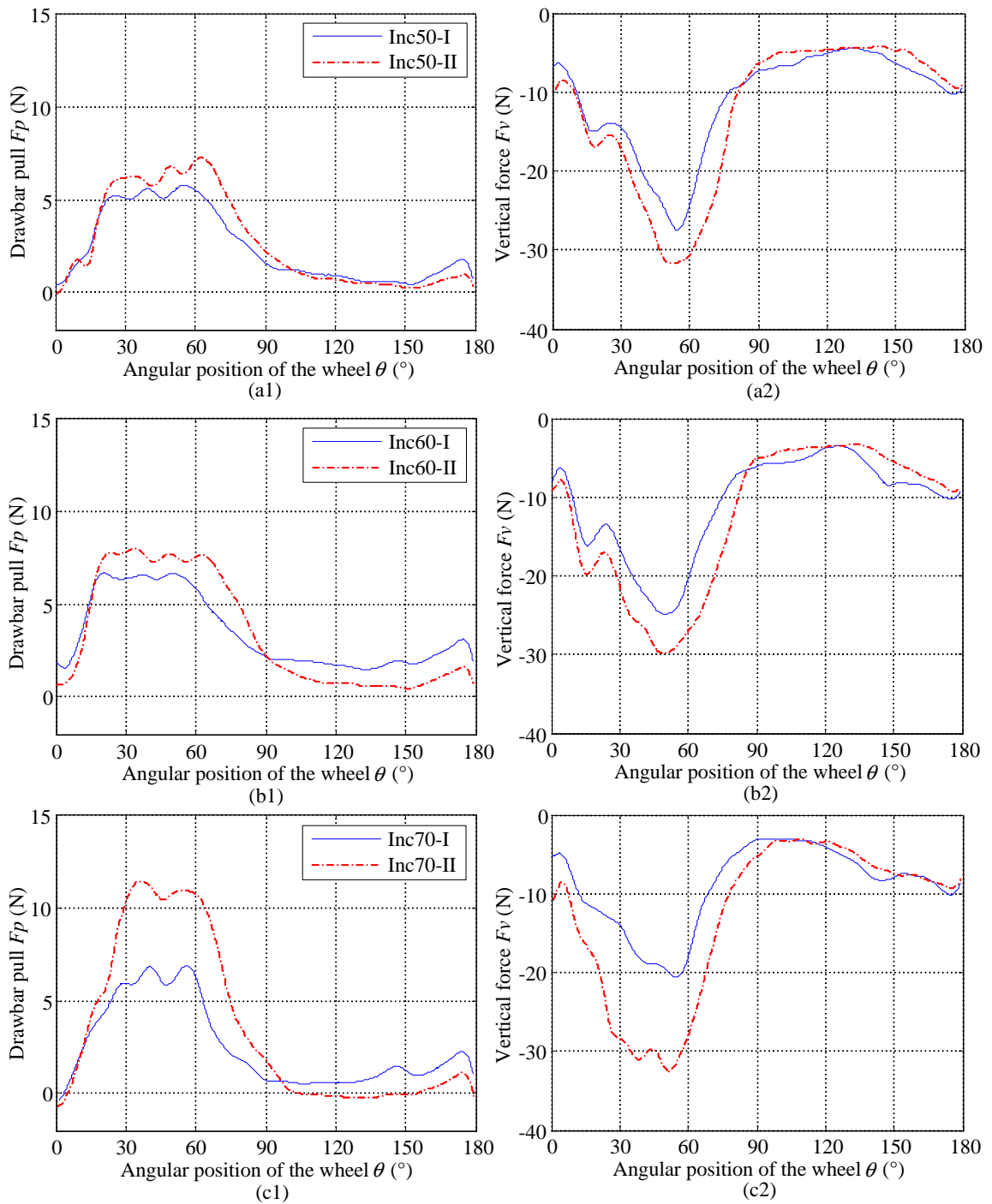


Figure 5.10. Drawbar pulls (left panels) and vertical forces (right panels) for different trajectories. (a) “Inc50-I” and “Inc50-II”, (b) “Inc60-I” and “Inc60-II”, (c) “Inc70-I” and “Inc70-II”.

equipped with multi-ALWs has the potential to meet kinematic constraints by rotating the wheel rim and meet the dynamic constraints by controlling the lug trajectory in real time, as discussion in Sec. 2.6.2.

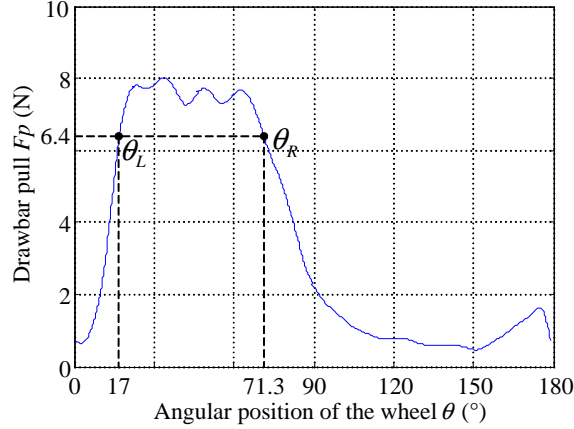


Figure 5.11. Definition of parameters for evaluating fluctuations of wheel-soil interaction force.

The fluctuations of the lugged wheel were evaluated over the range of wheel rotational angles for which the force exceeded 80% of its peak magnitude. The parameters defining this range are best described by the following example. The maximum drawbar pull in trajectory “Inc60-II” was 8 N; thus, a horizontal line is drawn at 6.4 N in Fig. 5.11. We denote the leftmost and rightmost intersection points between this line and the plotted curve by L ($\theta_L = 17^\circ$) and R ($\theta_R = 71.3^\circ$), respectively. Using (5.1), the range of wheel rotational angles $\Delta\theta$ is subsequently obtained as 54.3° . Note that, although this stable range was small, multiple controllable lugs can generate constant soil reaction forces over a wider range.

$$\Delta\theta = \theta_R - \theta_L \quad (5.1)$$

In the absence of interference between the adjacent lugs, the number of lugs that would ensure 80% or more of the peak wheel-soil interaction should exceed N_L , calculated as follows.

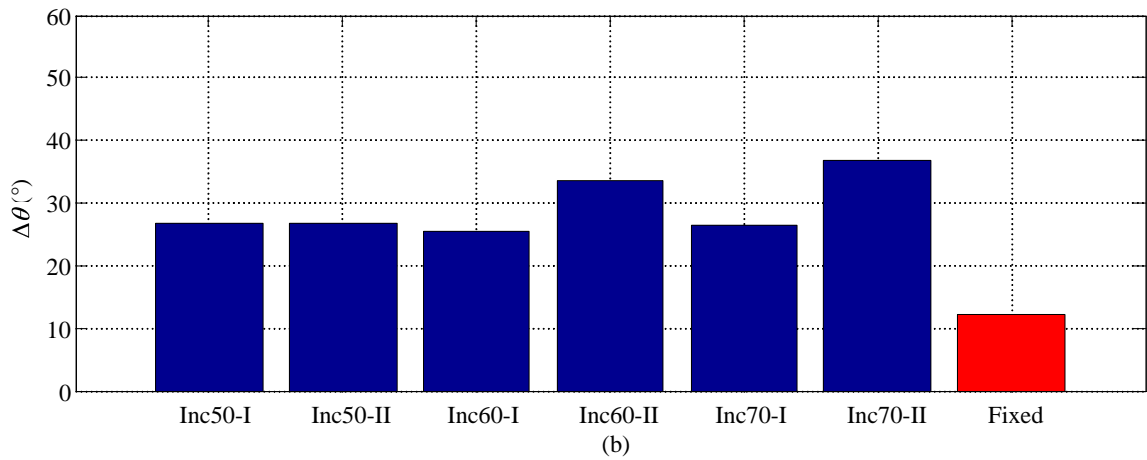
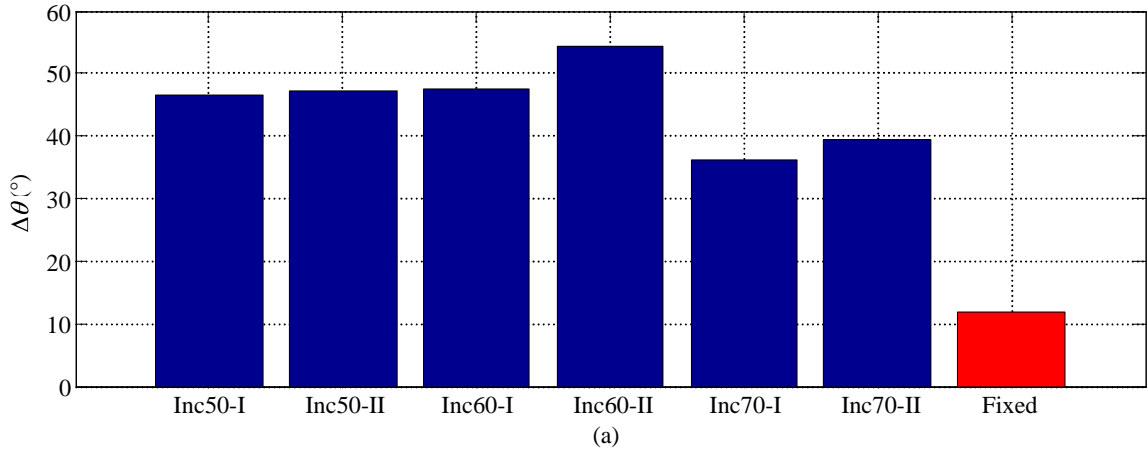


Figure 5.12. $\Delta\theta$ calculated from (5.1) for (a) drawbar pulls and (b) vertical forces of the ALW adopting six trajectories (blue bars) and fixed lugged wheel (red bar).

$$N_L = \frac{360^\circ}{\Delta\theta} \quad (5.2)$$

Obviously, the required number of lugs increases as $\Delta\theta$ decreases. Smaller $\Delta\theta$ means that more lugs must be equipped on the wheel surface. If the actual number installed is smaller than N_L , the soil reaction forces will fluctuate more violently.

The calculated $\Delta\theta$ s in six trajectories of the ALW mechanism and a fixed lugged wheel are presented in Table. 5.3 and plotted in Fig. 5.12 to more intuitively demonstrate their differences. The ALW mechanism significantly enlarged the $\Delta\theta$, increasing the ranges of drawbar pull and vertical force by 205%-356% and 107%-202%, respectively, relative to the conventional fixed lugged wheel.

Table 5.3. Evaluation of fluctuations in wheel-soil interaction forces.

Codes	Drawbar pull F_p [N]			Vertical force F_v [N]		
	θ_L [°]	θ_R [°]	$\Delta\theta$ [°]	θ_L [°]	θ_R [°]	$\Delta\theta$ [°]
Inc50-I	20.6	67.2	46.6	41.6	68.3	26.7
Inc50-II	23.8	71.1	47.3	41.6	68.3	26.7
Inc60-I	15.0	62.6	47.6	35.2	60.5	25.3
Inc60-II	17.0	71.3	54.3	32.8	66.5	33.7
Inc70-I	25.6	61.8	36.2	34.7	61.2	26.5
Inc70-II	27.0	66.5	39.5	25.2	62.8	37.6
Fixed	64.3	76.2	11.9	58.3	70.5	12.2

Notably, the offline method adopted in this study affirms that the ALW might reduce fluctuations in drawbar pull. However, because the module must be pre-tested in the target soil, its performance in unknown environments cannot be ascertained. For improved adaptability, the ALW should be enabled to generate its trajectory in real-time, based on feedback signals of the robot's motion state from on-board sensors. An online method for generating the lug trajectory will be investigated in future study.

5.3 Summary

This chapter has demonstrated the superior performance of the ALW mechanism fitted with a single lug. The experimental results are summarized below.

- i. The interference between the wheel rim and lug cannot be ignored. Owing to the soil deformation, the ALW can significantly enlarge the soil reaction forces which become larger than the sum of the soil reaction forces imposed by a separate cage lugged wheel and smooth wheel. Therefore, the lugged wheel is a better configuration for a locomotive module accessing soft terrains than the smooth wheel and single lug.
- ii. The ALW generated a larger drawbar pull and vertical force over a wider range than the fixed lugged wheel.
- iii. From experience, we identified six lug trajectories by which the ALW mechanism can dampen the fluctuations of the drawbar pull arising from a fixed lugged wheel.

Based on the experimental results and analysis in this chapter, we infer that the ALW module can potentially overcome the limitations of conventional wheeled robots by tuning its lug trajectory. This conclusion provides the fundamental principles for developing a lug trajectory generation strategy of a multi-lugged ALW mechanism in future.

Chapter 6

Conclusion and Future Work

6.1 Conclusion

This study proposed a novel wheel mechanism integrated with a set of actively actuated lugs, called Active Lugged Wheel (ALW). When rolling on sandy terrains, the ALW mechanism can actively adjust the lug inclination angle and lug sinkage length by alternating the position of the lug shaft. Based on the kinematic model and force analysis, a means of improving the ALW-soil interaction forces by tuning the lug trajectory was proposed. To this end, the lug-soil and ALW-soil interaction forces were sequentially measured on the fabricated testbeds. We then discussed the wheel-lug interference and experimentally verified the superior performance of the ALW mechanism.

Experiments were conducted on a single lug to determine how the lug motion influences the lug forces on sandy terrains without interference from the wheel rim. To quantify these effects, the measured data were numerically fitted by the least-squares method. The following conclusions were drawn. i) The horizontal and vertical forces acting on the lug are independent of traveling speeds below 10 mm/s. ii) The relationship between horizontal (or vertical) force and horizontal displacement can be approximated by an exponential function; the force characteristics are mainly contributed by ground swell owing to excavation by the lug. iii) The horizontal (or vertical) force is a quadratic function of lug sinkage in both

transient and steady-state of bulldozing experiments. iv) For a fixed lug sinkage length, the lug-soil interaction force can be maximized by setting the lug at an optimal inclination angle. In addition, the ratio of horizontal to vertical force can be increased by a more vertical setting of the lug (relative to the horizontal surface). Our experimental results confirm that the lug-soil interaction forces strongly depend on the lug trajectory.

Subsequently, we measured the drawbar pulls and vertical forces on a single-lugged ALW undergoing a complete interaction process. As the wheel rotated from 0° to 180° , the drawbar pull (or vertical force) increased to its peak at a certain rotational angle, then sharply decreased as the wheel rotated to around 100° and remained at approximately 0 N throughout the remaining period. We then varied the lug inclination angle and lug sinkage length and analyzed the effects of both parameters on the ALW-soil interaction forces. The sinkage length of the lug determined the resultant soil reaction force; in particular, the maximum drawbar pull (or vertical force) was a quadratic function of the lug sinkage length. The lug inclination angle altered the ratio of drawbar pull to vertical force; the ratio increased with increasing lug inclination angle as the wheel rotated from 45° to 78° .

Measurements of the lug-soil and ALW-soil interactions yielded different characteristics, motivating us to study the interference between the wheel rim and lugs. By comparing the drawbar pulls and vertical forces generated by a smooth wheel, a cage lugged wheel, and the ALW, we confirmed that the lugged wheel can exploit the deformation property of the sandy soil to realize a stronger drawbar pull and vertical force than the wheel rim or single lug alone. Moreover, the ALW mechanism generated a larger drawbar pull and vertical force over a wider range than the fixed-lugged wheel. Finally, we found six lug trajectories in which the ALW mechanism retains a stable force that is adjustable by adjusting the lug sinkage length. Although the stable range of a single lug is small, it could be widened by installing multiple controllable lugs. The experimental results from the single-lugged ALW provide the fundamental principles for a lug trajectory generation strategy of an actual ALW mechanism.

6.2 Future Work

Before it can be deployed as a fundamental locomotion mechanism in natural environments, the proposed ALW mechanism must overcome several challenges in modeling, control, and design. These challenges are discussed below.

- i. This study experimentally elucidated the soil reaction force characteristics of the ALW fitted with a single lug. Next, we need to understand how adjacent lugs interfere in a multi-lugged ALW. We can then develop a lug trajectory generation method that enables smooth movement of the multi-lugged ALW on soft terrains.
- ii. In this thesis, all tasks were performed in a sandy environment. However, the methodology adopted in this study can be extended to a wide range of robotics research environments with similar physical properties to sandy soils, such as waterlogged, muddy, and amphibious environments. The interaction characteristics of the ALW mechanism in these environments will be measured to improve its adaptability to diverse soft terrains.
- iii. The investigated lug trajectory generation method is an off-line method, which depends on soil type and conditions (such as moisture and compaction). To achieve autonomous locomotion with limited human supervision in complex unknown environments, an on-line lug trajectory generation strategy is required. The lug trajectories of the individual locomotion modules of an ALW-based vehicle could be generated from feedback signals supplied by the on-board sensors, thereby improving the traveling performance in real time without prior parameter measurements.

Once the ALW-based robot achieves reliable and adaptable autonomous locomotion in complex unknown environments, it can replace humans in high-risk missions, such as planetary exploration, active volcano observations, disaster rescue, and so on.

Bibliography

- [1] K. Iagnemma, H. Shibly, A. Rzepniewski, and S. Dubowsky, “Planning and control algorithms for enhanced rough-terrain rover mobility,” in *Proceedings of the 6th International Symposium on Artificial Intelligence, Robotics, and Automation in Space (i-SAIRAS 2001)*, Quebec, Canada, Jun. 2001.
- [2] K. Young. (2006) Mars rover escapes from the “bay of lamentation”, <http://www.newscientist.com/article/dn9286-mars-rover-escapes-from-the-bay-of-lamentation.html>.
- [3] D. Brown and G. Webster. (2010) Now a stationary research platform, nasa’s mars rover spirit starts a new chapter in red planet scientific studies, <http://www.nasa.gov/mission-pages/mer/news/mer20100126.html>.
- [4] Jet propulsion laboratory, jpl robotics, <http://www-robotics.jpl.nasa.gov/>.
- [5] R. Volpe, J. Balaram, T. Ohm, and R. Ivlev, “Rocky 7: a next generation mars rover prototype,” *Advanced Robotics*, vol. 11, no. 4, pp. 341–358, 1996.
- [6] Scientific information from the mars exploration rover mission, <http://en.wikipedia.org/wiki/scientific-information-from-the-mars-exploration-rover-mission>.
- [7] D. Brown, S. Cole, G. Webster, and D. Agle. Nasa mars rover begins driving at bradbury landing. <http://www.nasa.gov/home/hqnews/2012/aug/hq-12-292-mars-bradbury-landing.html>.
- [8] Mars science laboratory: Mission science goals, <http://mars.jpl.nasa.gov/msl/mission/science/goals/>.
- [9] G. Webster and D. Brown. Nasa’s mars curiosity rover marks first martian year, <http://www.jpl.nasa.gov/news/news.php?release=2014-199>.
- [10] D. Wettergreen, D. Bapna, M. Maimone, and G. Thomas, “Developing nomad for robotic exploration of the atacama desert,” *Robotics and Autonomous Systems*, vol. 26, no. 23, pp. 127 – 148, 1999, field and Service Robotics.
- [11] N. A. Cabrol, G. Chong-Diaz, C. R. Stoker, V. C. Gulick, R. Landheim, P. Lee, T. L. Roush, A. P. Zent, C. H. Lameli, A. J. Iglesia, M. P. Arrerondo, J. M. Dohm, R. Keaten, D. Wettergreen, M. H. Sims, K. Schwher, M. G. Bualat, H. J. Thomas, E. Zbinden, D. Christian, L. Pedersen, A. Bettis, G. Thomas, and B. Witzke, “Nomad rover field experiment, atacama desert, chile: 1. science results overview,” *Journal of Geophysical Research: Planets*, vol. 106, no. E4, pp. 7785 – 7806, 2001.

- [12] D. Wettergreen, S. Moreland, K. Skonieczny, D. Jonak, D. Kohanbash, and J. Teza, “Design and field experimentation of a prototype lunar prospector,” *The International Journal of Robotics Research*, 2010.
- [13] T. Aoki, Y. Murayama, and S. Hirose, “Development of a transformable three-wheeled lunar rover: Tri-star iv,” *Journal of Field Robotics*, vol. 31, no. 1, pp. 206 – 223, 2014.
- [14] S. Wakabayashi, H. Sato, and S.-I. Nishida, “Design and mobility evaluation of tracked lunar vehicle,” *Journal of Terramechanics*, vol. 46, no. 3, pp. 105 – 114, 2009.
- [15] D. I. Goldman, H. Komsuoglu, and D. E. Koditschek, “March of the sandbots,” pp. 30–35, 2009.
- [16] U. Saranli, M. Buehler, and D. E. Koditschek, “Rhex: A simple and highly mobile hexapod robot,” *The International Journal of Robotics Research*, vol. 20, no. 7, pp. 616–631, 2001.
- [17] A. Boxerbaum, P. Werk, R. Quinn, and R. Vaidyanathan, “Design of an autonomous amphibious robot for surf zone operation: part i mechanical design for multi-mode mobility,” in *Proceedings of 2005 IEEE/ASME International Conference on Advanced Intelligent Mechatronics (AIM 2005)*, Monterey, USA, Jul. 2005, pp. 1459 – 1464.
- [18] R. Harkins, J. Ward, R. Vaidyanathan, A. Boxerbaum, and R. Quinn, “Design of an autonomous amphibious robot for surf zone operations: part ii - hardware, control implementation and simulation,” in *Proceedings of 2005 IEEE/ASME International Conference on Advanced Intelligent Mechatronics (AIM 2005)*, Monterey, UCA, Jul. 2005, pp. 1465 – 1470.
- [19] J. Dietsch, B. Kennedy, A. Okon, H. Aghazarian, M. Badescu, X. Bao, Y. Bar.Cohen, Z. Chang, B. E. Dabiri, M. Garrett, L. Magnone, and S. Sherrit, “Lemur iib: a robotic system for steep terrain access,” *Industrial Robot: An International Journal*, vol. 33, no. 4, pp. 265 – 269, 2006.
- [20] K. Nagatani, H. Kinoshita, K. Yoshida, K. Tadakuma, and E. Koyanagi, “Development of leg-track hybrid locomotion to traverse loose slopes and irregular terrain,” *Journal of Field Robotics*, vol. 28, no. 6, pp. 950 – 960, 2011.
- [21] K. Hauser, T. Bretl, J.-C. Latombe, and B. Wilcox, “Motion planning for a six-legged lunar robot,” in *Algorithmic Foundation of Robotics VII*, ser. Springer Tracts in Advanced Robotics, S. Akella, N. Amato, W. Huang, and B. Mishra, Eds. Springer Berlin Heidelberg, 2008, vol. 47, pp. 301–316.
- [22] E. Rohmer, G. Reina, and K. Yoshida, “A novel teleoperated hybrid wheel-limbed hexapod for the exploration of lunar challenging terrains,” in *Proceedings of the 26th International Symposium on Space Technology and Sciences*, Hamamatsu, Japan, Jun. 2008, pp. 3902 – 3907.
- [23] H. Nakano and S. Hirose, “Crank-wheel: A brand new mobile base for field robots,” in *Proceedings of the 2012 IEEE/RSJ International Conference on Intelligent Robots and Systems (IROS 2012)*, Vilamoura, Portugal, Oct. 2012, pp. 4608 – 4613.
- [24] P. Berkelman, J. Easudes, M. C. Martin, E. Rollins, and J. Silberman, “Design of a day/night lunar rover,” Carnegie Mellon University, Tech. Rep., 1995.

- [25] (2005) The apollo lunar roving vehicle. <http://nssdc.gsfc.nasa.gov/planetary/lunar/apollo-lrv.html>.
- [26] Introduction to the microrover, <http://mars.jpl.nasa.gov/mpf/rovercom/rovintro.html>.
- [27] R. Lindemann and C. Voorhees, “Mars exploration rover mobility assembly design, test and performance,” in *Proceedings of the 2005 IEEE International Conference on Systems, Man and Cybernetics*, Pasadena, USA, Oct. 2005, pp. 450 – 455.
- [28] M. Heverly, J. Matthews, J. Lin, D. Fuller, M. Maimone, J. Biesiadecki, and J. Leichty, “Traverse performance characterization for the mars science laboratory rover,” *Journal of Field Robotics*, vol. 30, no. 6, pp. 835 – 846, 2013.
- [29] T. Kubota, Y. Kuroda, Y. Kunii, and I. Nakatani, “Small, light-weight rover ”micro5” for lunar exploration,” *Acta Astronautica*, vol. 52, no. 2-6, pp. 447 – 453, 2003.
- [30] J. Liu, H. Gao, and Z. Deng, “Effect of straight grousers parameters on motion performance of small rigid wheel on loose sand,” *Information Technology Journal*, vol. 7, no. 8, pp. 1125 – 1132, 2008.
- [31] L. Ding, H. Gao, Z. Deng, K. Nagatani, and K. Yoshida, “Experimental study and analysis on driving wheels performance for planetary exploration rovers moving in deformable soil,” *Journal of Terramechanics*, vol. 48, no. 1, pp. 27 – 45, 2011.
- [32] M. Sutoh, K. Nagaoka, K. Nagatani, and K. Yoshida, “Design of wheels with grousers for planetary rovers traveling over loose soil,” *Journal of Terramechanics*, vol. 50, no. 56, pp. 345 – 353, 2013.
- [33] M. Sutoh, J. Yusa, T. Ito, K. Nagatani, and K. Yoshida, “Traveling performance evaluation of planetary rovers on loose soil,” *Journal of Field Robotics*, vol. 29, no. 4, pp. 648 – 662, 2012.
- [34] M. Sutoh, K. Nagaoka, K. Nagatani, and et al., “Evaluation of influence of surface shape of locomotion mechanism on traveling performance of planetary rovers,” in *2012 IEEE International Conference on Robotics and Automation (ICRA2012)*, St. Paul, MN, USA, May. 2012, pp. 3419–3424.
- [35] L. Ding, Z. Deng, H. Gao, J. Guo, D. Zhang, and K. D. Iagnemma, “Experimental study and analysis of the wheels steering mechanics for planetary exploration wheeled mobile robots moving on deformable terrain,” *The International Journal of Robotics Research*, vol. 32, no. 6, pp. 712 – 743, 2013.
- [36] B. Chen and Y. Chao, “The research of driving wheel with movable lugs of the paddy field floating tractor,” in *Proceedings of the 8th International Conference on International Society for Terrain-vehicle Systems (ISTVS1984)*, Cambridge, Aug. 1984, pp. 495 – 505.
- [37] W. Hermawan, A. Oida, and M. Yamazaki, “Measurement of soil reaction forces on a single movable lug,” *Journal of Terramechanics*, vol. 33, no. 2, pp. 91 – 101, 1996.
- [38] W. Hermawan, A. Oida, and et al., “The characteristics of soil reaction forces on a single movable lug,” *Journal of Terramechanics*, vol. 34, no. 1, pp. 23 – 35, 1997.

- [39] W. Hermawan, M. Yamazaki, and A. Oida, "Experimental analysis of soil reaction on a lug of a movable lug wheel," *Journal of Terramechanics*, vol. 35, no. 2, pp. 119 – 135, 1998.
- [40] Z. Chen, "Research of compound walking wheel having retractile laminas with application to lunar rover," Master's thesis, Jilin University, Changchun, China, (in Chinese) 2007.
- [41] D. Hettiaratchi, B. Witney, and A. Reece, "The calculation of passive pressure in two-dimensional soil failure," *Journal of Agricultural Engineering Research*, vol. 11, no. 2, pp. 89 – 107, 1966.
- [42] W. C. David Gee-Clough, "Pull and lift characteristics of single lugs on rigid wheels in wet rice soils," *Transactions of the ASABE*, vol. 19(3), pp. 433–447, 1976.
- [43] W. Hermawan, M. Yamazaki, and A. Oida, "Theoretical analysis of soil reaction on a lug of the movable lug cage wheel," *Journal of Terramechanics*, vol. 37, no. 2, pp. 65 – 86, 2000.
- [44] D. R. P. Hettiaratchi and A. R. Reece, "Symmetrical three-dimensional soil failure: by d. r. p. hettiaratchi and a. r. reece," *Journal of Terramechanics*, vol. 4, no. 3, pp. 45 – 67, 1967.
- [45] E. McKyes and O. Ali, "The cutting of soil by narrow blades," *Journal of Terramechanics*, vol. 14, no. 2, pp. 43 – 58, 1977.
- [46] R. Godwin and G. Spoor, "Soil failure with narrow tines," *Journal of Agricultural Engineering Research*, vol. 22, no. 3, pp. 213 – 228, 1977.
- [47] C. S. D. J. V. Perumpral, R. D. Grisso, "A soil-tool model based on limit equilibrium analysis," *Transactions of the ASAE*, vol. 26, no. 4, pp. 991 – 995, 1983.
- [48] W. Harrison, "Soil failure under inclined loads i," *Journal of Terramechanics*, vol. 9, no. 4, pp. 41 – 63, 1973.
- [49] W. Harison, "Soil failure under inclined loads ii," *Journal of Terramechanics*, vol. 10, no. 1, pp. 11 – 50, 1973.
- [50] K. Triratanasirichai, A. Oida, and M. Honda, "The performance of cage wheels for small power tillers in agricultural soil," *Journal of Terramechanics*, vol. 27, no. 3, pp. 193–205, 1990.
- [51] H. Nakashima, "Analyses of interaction between a lug of lugged wheel and wet cohesive soil," Ph.D. dissertation, Kyoto University, 1989.
- [52] Y. Yang, Y. Sun, and et al., "Characteristics of tangential force acting on a single lug with translational motion in sandy soil," in *Proceedings of the 2014 IEEE 4th Annual International Conference on Cyber Technology in Automation, Control, and Intelligent Systems (CYBER 2014)*, Hongkong, China, Jun. 2014, pp. 31–36.
- [53] Bekker.M.G, *Introduction to terrain-vehicle systems*, A. Arbor, Ed. The University of Michigan, 1969.

- [54] J. Wong and A. Reece, “Prediction of rigid wheel performance based on the analysis of soil-wheel stresses part i. performance of driven rigid wheels,” *Journal of Terramechanics*, vol. 4, no. 1, pp. 81 – 98, 1967.
- [55] K. Nagatani, A. Ikeda, K. Sato, and K. Yoshida, “Accurate estimation of drawbar pull of wheeled mobile robots traversing sandy terrain using built-in force sensor array wheel,” in *2009 IEEE/RSJ International Conference on Intelligent Robots and Systems (IROS 2009)*, 2009, pp. 2373–2378.
- [56] H. Nakashima, H. Fujii, A. Oida, M. Momozu, Y. Kawase, H. Kanamori, S. Aoki, and T. Yokoyama, “Parametric analysis of lugged wheel performance for a lunar microrover by means of {DEM},” *Journal of Terramechanics*, vol. 44, no. 2, pp. 153 – 162, 2007.
- [57] H. Nakashima, H. Fujii, A. Oida, M. Momozu, H. Kanamori, S. Aoki, T. Yokoyama, H. Shimizu, J. Miyasaka, and K. Ohdoi, “Discrete element method analysis of single wheel performance for a small lunar rover on sloped terrain,” *Journal of Terramechanics*, vol. 47, no. 5, pp. 307 – 321, 2010.
- [58] R. Irani, R. Bauer, and A. Warkentin, “A dynamic terramechanic model for small lightweight vehicles with rigid wheels and grousers operating in sandy soil,” *Journal of Terramechanics*, vol. 48, no. 4, pp. 307 – 318, 2011.
- [59] Y. Favaedi, A. Pechev, M. Scharringhausen, and L. Richter, “Prediction of tractive response for flexible wheels with application to planetary rovers,” *Journal of Terramechanics*, vol. 48, no. 3, pp. 199 – 213, 2011.
- [60] K. Iagnemma, C. Senatore, B. Trease, R. Arvidson, K. Bennett, A. Shaw, F. Zhou, L. Van Dyke, and R. Lindemann, “Terramechanics modeling of mars surface exploration rovers for simulation and parameter estimation,” in *Proceedings of ASME International Design Engineering Technical Conference & Computers and Information Engineering Conference (IDETC/CIE2011)*, vol. 2011, 2011.
- [61] K. Iizuka, T. Yoshida, and T. Kubota, “Effect of tractive given by grousers mounted on wheels for lunar rovers on loose soil,” in *Proceedings of the 37th Annual Conference on IEEE Industrial Electronics Society (IECON 2011)*, 2011, pp. 110–115.
- [62] Bekker.M.G, *Off-road locomotion: research and development in terramechanics*, A. Arbor, Ed. The University of Michigan, 1969.
- [63] L. Ding, Z. Deng, H. Gao, K. Nagatani, and K. Yoshida, “Planetary rovers’ wheel—soil interaction mechanics: New challenges and applications for wheeled mobile robots,” *Intelligent Service Robotics*, vol. 4, no. 1, pp. 17 – 38, 2011.
- [64] R. Yong, A. Youssef, and E. Fattah, “Vane-cone measurements for assessment of tractive performance in wheel-soil interaction,” in *Proceedings of the 5th International Society of Terrain Vehicle Systems (ISTVS 75)*, Detroit, USA, 1975, pp. 769 – 788.
- [65] K. Pandey and T. Ojha, “Effect of design parameters on the performance of rigid traction wheels on saturated soils,” *Journal of Terramechanics*, vol. 15, no. 3, pp. 145 – 156, 1978.

- [66] S. Wanjii, T. Hiroma, Y. Ota, and T. Kataoka, "Prediction of wheel performance by analysis of normal and tangential stress distributions under the wheel-soil interface," *Journal of Terramechanics*, vol. 34, no. 3, pp. 165 – 186, 1997.
- [67] J. Perumpral, J. Liljedahl, and W. Perloff, "A numerical method for predicting the stress distribution and soil deformation under a tractor wheel," *Journal of Terramechanics*, vol. 8, no. 1, pp. 9 – 22, 1971.
- [68] K. Iagnemma, "A laboratory single wheel testbed for studying planetary rover wheel-terrain interaction," MIT, Tech. Rep., 2005.
- [69] G. Ishigami, A. Miwa, K. Nagatani, and K. Yoshida, "Terramechanics-based model for steering maneuver of planetary exploration rovers on loose soil," *Journal of Field Robotics*, vol. 24, no. 3, pp. 233–250, 2007.
- [70] L. Ding, "Wheel-soil interaction terramechanics for lunar/planetary exploration rovers: modeling and application," Ph.D. dissertation, Harbin Institute of Technology, China, 2009, (in Chinese).
- [71] K. Iizuka, Y. Sato, Y. Kuroda, and T. Kubota, "Study on wheel of exploration robot on sandy terrain," in *Proceedings of the 2006 IEEE/RSJ International Conference on Intelligent Robots and Systems (IROS 2006)*, Oct 2006, pp. 4272–4277.
- [72] D. Apostolopoulos, "Analytic configuration of wheeled robotic locomotion," Tech. Rep., 2001.
- [73] S. Michaud, L. Richter, T. Thueer, A. Gibbesch, T. Huelsing, N. Schmitz, S. Weiss, A. Krebs, N. Patel, L. Joudrier *et al.*, "Rover chassis evaluation and design optimisation using the rcet," in *Proceedings of the 9th ESA Workshop on Advanced Space Technologies for Robotics and Automation (ASTRA 2006)*, Noordwijk, The netherlands, Nov. 2006.
- [74] K. Iagnemma and S. Dubowsky, "Traction control of wheeled robotic vehicles in rough terrain with application to planetary rovers," *The International Journal of Robotics Research*, vol. 23, no. 10-11, pp. 1029 – 1040, 2004.
- [75] P. Lamon, A. Krebs, M. Lauria, R. Siegwart, and S. Shooter, "Wheel torque control for a rough terrain rover," in *Proceedings of the 2004 IEEE International Conference on Robotics and Automation (ICRA2004)*., vol. 5, Barcelona, Spain., Apr. 2004, pp. 4682–4687.
- [76] K. Yoshida and H. Hamano, "Motion dynamics of a rover with slip-based traction model," in *Proceedings of the 2002 IEEE International Conference on Robotics and Automation (ICRA 02)*, vol. 3, Washington, USA, May. 2002, pp. 3155 – 3160.
- [77] G. Ishigami, K. Nagatani, and K. Yoshida, "Slope traversal controls for planetary exploration rover on sandy terrain," *Journal of Field Robotics*, vol. 26, no. 3, pp. 264 – 286, 2009.
- [78] Y. Yang, Y. Sun, and S. Ma, "Effect of lug sinkage length to drawbar pull of a wheel with an actively actuated lug on sandy terrain," in *Proceedings of the 2014 IEEE International Conference on Robotics and Automation (ICRA 2014)*, Hongkong, China, May. 2014, pp. 2932–2937.

- [79] Y. Yang, Y. Sun, and et al., “Paddle trajectory generation for accessing soft terrain by an epaddle locomotion mechanism,” in *Proceedings of the 2013 IEEE International Conference on Robotics and Automation (ICRA 2013)*, Karlsruhe, Germany, May. 2013, pp. 403–408.
- [80] Z. Janosi and B. Hanamoto, “The analytical determination of drawbar pull as a function of slip for tracked vehicles in deformable soils,” in *Proceedings of the 1st international conference on soil-vehicle systems.*, Turin, Italy, 1961.
- [81] G. Ishigami, “Terramechanics-based analysis and control for lunar/planetary exploration robots,” Ph.D. dissertation, Tohoku University, 2008.

Published Papers During Doctoral Course

Journal Papers:

1. Yang Yang, Yi Sun and Shugen Ma, Drawbar pull of a wheel with an actively actuated lug on sandy terrain, *Journal of Terramechanics*, vol.56, pp. 17–24, 2014.
2. Yang Yang, Yi Sun, Shugen Ma and Ryohei Yamamoto, Characteristics of normal and tangential forces acting on a single lug during translational motion in sandy soil, *Journal of Terramechanics*, vol.55, pp. 47–59, 2014.
3. Yi Sun, Shugen Ma, Yang Yang and Huayan Pu, Towards stable and efficient legged race-walking of an ePaddle-based robot, *Mechatronics*, vol.23, no.1, pp. 108–120, 2013.

International Conference Papers:

1. Yang Yang, Yi Sun and Shugen Ma, Effect of lug sinkage length to drawbar pull of a wheel with an actively actuated lug on sandy terrain, In *Proc. of the 2014 IEEE Int. Conf. on Robotics and Automation (ICRA'14)*, Hongkong, China, pp. 2932–2937, Jun., 2014.
2. Yang Yang, Yi Sun and Shugen Ma, Paddle trajectory generation for accessing soft terrain by an ePaddle locomotion mechanism, In *Proc. of the 2013 IEEE Int. Conf.*

- on Robotics and Automation (ICRA '13)*, Karlsruhe, Germany, pp. 403–408, May., 2013.
3. **Yang Yang**, Yi Sun, Ryohei Yamamoto and Shugen Ma, Characteristics of tangential force acting on a single lug with translational motion in sandy soil, In *Proc. of the 2014 IEEE Int. Conf. on CYBER Technology in Automation, Control, and Intelligent Systems (CYBER'14)*, Hongkong, China, pp. 31–36, Jun., 2014. (Best Student Paper Award Finalist)
 4. **Yang Yang**, Yi Sun, Ryohei Yamamoto and Shugen Ma, Influence of moving direction on normal force acting on a single lug during translational motion in sandy soil, In *Proc. of the 2014 IEEE Int. Conf. on Robotics and Biomimetics (ROBIO'14)*, Bali, Indonesia, pp. 425–430, Dec., 2014.
 5. Ryohei Yamamoto, **Yang Yang**, Yi Sun and Shugen Ma, Influences of lug motion on lug-soil reaction forces in sandy soil, In *Proc. of the 2014 IEEE Int. Conf. on Automation Science and Engineering (CASE'14)*, Taipei, Taiwan, pp. 176–181, Aug., 2014.
 6. Ryohei Yamamoto, **Yang Yang**, Yi Sun and Shugen Ma, Characteristics of lug-soil interaction forces acting on a rotating lug in sandy soil, In *Proc. of the 2014 IEEE Int. Conf. on Robotics and Biomimetics (ROBIO'14)*, Bali, Indonesia, pp. 451–456, Dec., 2014.
 7. Huayan Pu, Yi Sun, Shugen Ma, **Yang Yang**, et al., Design and locomotion simulation of an improved eccentric paddle mechanism for amphibious robots, In *Proc. of the 2013 IEEE Int. Conf. on Robotics and Biomimetics (ROBIO'13)*, Shenzhen, China, pp. 510–515, Dec., 2013. (Best Paper Award in Biomimetics)
 8. Huayan Pu, Yi Sun, **Yang Yang**, and Shugen Ma, Modeling of the oscillating-paddling gait for an epaddle locomotion mechanism, In *Proc. of the 2013 IEEE Int. Conf. on Robotics and Automation (ICRA '13)*, Karlsruhe, German, pp. 3429–3435, May. 2013.

9. Yi Sun, Shugen Ma, Kazuhiro Fujita, **Yang Yang**, and Huayan Pu, Modeling the rotational paddling of an ePaddle-based amphibious robot, In *Proc. of the 2012 IEEE/RSJ Int. Conf. on Intelligent Robots and Systems (IROS'12)*, Algarve, Portugal, pp. 610–615, Oct., 2012.
10. Yi Sun, Shugen Ma, and **Yang Yang**, Planning of legged racewalking gait for an ePaddle-based amphibious robot, In *Proc. of the 10th Int. IFAC Symp. on Robot Control (SYROCO'12)*, Dubrovnik, Croatia, pp. 218–223, Sept., 2012.